TECHNISCHE
UNIVERSITÄT
WIEN
Vienna | Austria

ILSB Institute of
Lightweight Design and
Structural Biomechanics

Dissertation

Development of an Additive Manufacturing System for Producing Tissue-Mimicking Materials

carried out for the purpose of obtaining the degree of Doctor technicae (Dr. techn.)
submitted at TU Wien, Faculty of Mechanical and Industrial Engineering by

Laszlo Jaksa MSc

Mat. Nr.: 11740246

under the supervision of

Univ. Prof. Dipl.-Ing. Dr. techn. Dieter H. PAHR

Institute of Lightweight Design and Structural Biomechanics (ILSB), E317

Vienna, March 2023

Reviewed by

Assoc. Prof. Dipl.-Ing. Dr. techn.
Francesco Moscato

Center for Medical Physics and
Biomedical Engineering,
Medical University of Vienna

AKH Vienna, Leitstelle 4L,
Währinger Gürtel 18-20,
1090 Vienna, Austria

Univ. Prof. Dipl.-Ing. Dr. techn.
Rita M. Kiss

Department of Mechatronics, Optics
and Mechanical Engineering Informatics,
Budapest University of Technology
and Economics

Building D, 4th floor,
Bertalan Lajos utca 4-6,
1111 Budapest, Hungary

Funding

This work was supported by the Provincial Government of Lower Austria (Land Niederösterreich) under grant assignment number WST3-F2-528983/005-2018.

This work was also supported by ACMIT Gmbh (Austrian Center for Medical Innovation and Technology), which is funded within the scope of the “Competence Centers for Excellent Technologies” (COMET) program of the Austrian Research Promotion Agency (FFG), and by the federal government (BMDW and BMK) along with the governments of Lower Austria and Tyrol.

Affidavit

I confirm, that going to press of this thesis needs the confirmation of the examination committee.

I declare in lieu of oath, that I wrote this thesis and performed the associated research myself, using only literature cited in this volume. If text passages from sources are used literally, they are marked as such.

I confirm that this work is original and has not been submitted elsewhere for any examination, nor is it currently under consideration for a thesis elsewhere.

I acknowledge that the submitted work will be checked electronically-technically using suitable and state-of-the-art means (plagiarism detection software). On the one hand, this ensures that the submitted work was prepared according to the high-quality standards within the applicable rules to ensure good scientific practice "Code of Conduct" at the TU Wien. On the other hand, a comparison with other student theses avoids violations of my personal copyright.

Vienna, March 2023

Table of Contents

Chapter **Page**

Abstract

Development of an Additive Manufacturing System for Producing Tissue-Mimicking Materials

Anatomic models play a crucial role in the field of medical education and preoperative planning. They allow medical students or doctors to prepare for real-life scenarios in a controlled, risk-free environment. Additive manufacturing techniques have led to the creation of several experimental anatomic models with improved geometric, radiological, or biomechanical realism. In this context, the main focus of this thesis is the reproduction of realistic biomechanical behavior of soft tissues. Since there is no readily available commercial 3D printer for this, the first step was the development of a custom-built 3D printer. This printer can print soft and hard materials and allows for multi-material structuring. The printer is based on extrusion technology and is capable of depositing both thermoplastic and silicone rubber materials.

The accuracy and limits of this printer were studied with given materials. The printhead calibration process of the custom-built silicone printer was defined, and a set of test objects was proposed, printed, and evaluated in terms of geometric integrity and accuracy. Results indicated that silicone viscosity has a strong impact on geometric inaccuracies, and design recommendations were made based on the results. Afterwards, the feasibility of geometric features such as thin walls, infill structuring, overhangs, and multi-material interfaces was tested through the printing of various objects. A proof-of-concept medical image-based ribcage model was also successfully printed, demonstrating the potential of the printer to manufacture anatomic models.

In the next step, anatomical models were created from medical images and printed with realistic biomechanical behavior and radiological similarity. The liver model was printed using a soft silicone rubber as a structural material, silicone oil as a filler fluid inside the infill structure, and poly-lactic acid filament as hard support. A set of tensile testing specimens with matching structures was also printed. The results of CT-scanning of the liver model and tensile testing of the matching test specimens suggested that the liver model became more realistic in both mechanical and radiological properties compared to models printed solely with silicone rubber, demonstrating the potential for customization opportunities in the field of anatomic models through this rubber-fluid-thermoplastic printing method.

In summary, a 3D printer was developed and extensively tested in this work. Consecutively, realistic anatomical models were produced with it. The use of silicone printing and multi-material structuring techniques in the field of 3D-printed anatomic models was established, offering new opportunities for customization and increased realism in medical education, device development and preoperative planning.

Keywords:

anatomic models, tissue mimicking, silicone rubber, 3D-printing, additive manufacturing

Deutsche Kurzfassung

Entwicklung eines additiven Fertigungssystems zur Herstellung gewebeähnlicher Materialien

Anatomische Modelle spielen im Bereich der medizinischen Ausbildung und der präoperativen Planung eine entscheidende Rolle. Sie ermöglichen es Medizinstudenten oder Ärzten, sich in einer kontrollierten, risikofreien Umgebung auf reale Szenarien vorzubereiten. In diesem Bereich haben die additiven Fertigungstechniken zur Herstellung mehrerer experimenteller anatomischer Modelle mit verbessertem geometrischen, radiologischen, oder biomechanischen Realismus geführt. In diesem Zusammenhang liegt das Hauptaugenmerk dieser Arbeit auf der Reproduktion eines realistischen biomechanischen Verhaltens von Weichteilgeweben. Da es hierfür keinen handelsüblichen 3D-Drucker gibt, wurde in einem ersten Schritt ein eigener 3D-Drucker entwickelt. Dieser Drucker kann weiche und harte Materialien drucken und ermöglicht die Strukturierung aus mehreren Materialien. Der Drucker basiert auf der Extrusionstechnologie und ist in der Lage, sowohl thermoplastische als auch Silikonkautschukmaterialien aufzutragen.

Nach dem Bau des Druckers wurden die Genauigkeit und die Grenzen dieses Druckers mit bestimmten Materialien untersucht. Der Druckkopf des speziell angefertigten Silikondruckers wurde kalibriert, und eine Reihe von Testobjekten wurde vorgeschlagen, gedruckt und im Hinblick auf die geometrische Integrität und Genauigkeit bewertet. Die Ergebnisse wiesen darauf hin, dass die Silikonviskosität einen starken Einfluss auf geometrische Ungenauigkeiten hat, und auf der Grundlage der Ergebnisse wurden Designempfehlungen ausgesprochen. Anschließend wurde die Machbarkeit von geometrischen Merkmalen wie dünnen Wänden, Füllstrukturen, Überhängen und Multimaterial-Schnittstellen durch den Druck verschiedener Objekte getestet. Ein auf medizinischen Bildern basierendes Brustkorbmodell wurde ebenfalls erfolgreich gedruckt, was das Potenzial des Druckers für die Herstellung anatomischer Modelle demonstriert.

In einem nächsten Schritt wurden anatomische Modelle aus medizinischen Bildern erstellt und mit realistischem biomechanischem Verhalten und radiologischer Ähnlichkeit gedruckt. Das Lebermodell wurde mit einem weichen Silikonkautschuk als Strukturmaterial, Silikonöl als

Füllflüssigkeit innerhalb der Füllstruktur und Polymilchsäurefilament als harter Träger gedruckt. Außerdem wurde eine Reihe von Zugversuchsproben mit passenden Strukturen gedruckt. Die Ergebnisse des CT-Scans des Lebermodells und der Zugprüfung der passenden Prüfkörper zeigten, dass das Lebermodell sowohl in Bezug auf die mechanischen als auch auf die radiologischen Eigenschaften realistischer war als Modelle, die nur mit Silikonkautschuk gedruckt wurden, was das Potenzial für individuelle Anpassungsmöglichkeiten im Bereich der anatomischen Modelle durch diese Gummifluid-Thermoplast-Druckmethode verdeutlicht.

Zusammenfassend lässt sich sagen, dass in dieser Arbeit ein 3D-Drucker entwickelt und ausgiebig getestet wurde. Nacheinander wurden damit realistische anatomische Modelle hergestellt. Der Einsatz von Silikondruck und Multi-Material-Strukturierungstechniken im Bereich der 3D-gedruckten anatomischen Modelle wurde etabliert und bietet neue Möglichkeiten für die individuelle Anpassung und einen erhöhten Realismus in der medizinischen Ausbildung, der Geräteentwicklung und der präoperativen Planung.

Stichwörter:
anatomische Modelle, Gewebeimitation, Silikonkautschuk, 3D-Druck, additive Fertigung

Acknowledgements

I would like to express my sincerest gratitude to my supervisor, **Dieter Pahr**, for his unwavering support, guidance, and encouragement throughout the entire research. His experience and wisdom were invaluable to me and helped me to stay focused and motivated.

I am also thankful to **Andrea Lorenz**, for her insights and feedback, and for keeping the project running smoothly. I am deeply grateful to **Gernot Kronreif**, **Nikolaus Dellantoni**, and all my colleagues at ACMIT[*] who provided me with such a supportive and collaborative work environment.

I also wish to extend my thanks to **Othniel James Aryeetey**, **Katharina Nägl**, **Sarah-Jane Estermann**, and all colleagues at KL[**] and ILSB[***], who made the overall experience throughout this research enjoyable and unforgettable. I am also grateful to **Sepideh Hatamikia** and **Martin Buschmann**, who also provided me with invaluable help and support.

I would like to express my appreciation to **Rita Kiss** and **Francesco Moscato** for taking their time to review my dissertation and providing me with valuable feedback.

Finally, I would like to extend my heartfelt appreciation to my family and friends for their emotional support and encouragement, which was a constant source of motivation for me throughout the journey and made this achievement possible.

---

[*] Austrian Center for Medical Innovation and Technology, Wiener Neustadt, Austria

[**] Department of Biomechanics, Karl Landsteiner University of Health Sciences

[***] Institute of Lightweight Design and Structural Biomechanics, Technical University of Vienna

List of Publications

Peer-reviewed journal publications

L. Jaksa, D. H. Pahr, G. Kronreif, A. Lorenz: Development of a multi-material 3D printer for functional anatomic models, *International Journal of Bioprinting*, 7(4):420, 2021, DOI: 10.18063/ijb.v7i4.420

L. Jaksa, D. H. Pahr, G. Kronreif, A. Lorenz: Calibration dependencies and accuracy assessment of a silicone rubber 3D printer, *Inventions*, 7(2):35, 2022, DOI: 10.3390/inventions7020035

L. Jaksa, O. J. Aryeetey, S. Hatamikia, K. Nägl, M. Buschmann, D. H. Pahr, G. Kronreif, A. Lorenz: 3D-printed multi-material liver model with simultaneous mechanical and radiological tissue-mimicking features for improved realism, *International Journal of Bioprinting*, 9(3):721, 2023, DOI: 10.18063/ijb.721

The contributions of L. Jaksa to these publications included planning the studies and methodology, independently conducting the experiments, performing data analysis, and writing the manuscripts. D. H. Pahr and G. Kronreif provided resources, infrastructure, project guidance, and reviewed manuscript drafts. A. Lorenz was responsible for overseeing the project progress, conceptualizations, medical image segmentation, and reviewing the manuscript drafts. O. J. Aryeetey, S. Hatamikia, K. Nägl and M. Buschmann facilitated the mechanical testing and medical imaging parts of the experimental work.

Furthermore, concerning the manufacturing technology described in this work, a patent application has been filed at the European Patent Office under reference number 51241 on behalf of ACMIT Gmbh, with L. Jaksa, A. Lorenz and D. H. Pahr as inventors.

Conference contributions

L. Jaksa, A. Lorenz: 3D-printing soft materials to mitigate the effects of Covid-19 in medical education, *26th SESAM Virtual Annual Meeting*, 14-16 April 2021, Online

L. Jaksa, A. Lorenz: Extrusion-based multi-material 3D-printer for anatomic models, *55th DGBMT Annual Conference on Biomedical Engineering*, 5-7 October 2021, Hannover, Germany

L. Jaksa: Additive manufacturing with silicone rubbers – Case Study, *TCT Confrence at Formnext 2021*, 16-19 November 2021, Frankfurt am Main, Germany

L. Jaksa, S. Hatamikia, D. Pahr, G. Kronreif, A. Lorenz: 3D-Printer Enabling Customized Anatomic Models (Poster), *27th Congress of the European Society of Biomechanics*, 26-29 June 2022, Porto, Portugal, DOI: 10.13140/RG.2.2.28812.39049

L. Jaksa, A. Lorenz, G. Kronreif, D. Pahr: Dependencies and limits in cold-extrusion silicone rubber 3D-printing, *Joint Annual Conference on Biomedical Engineering (ÖGBMT, DGBMT, SSBE)*, 28-30 September 2022, Innsbruck, Austria

L. Jaksa, D. Pahr, G. Kronreif, A. Lorenz: Simultaneous liquid and filament 3D-printing for anatomic models and medical devices (Poster), *1st prize winner in the category of medical innovation at the Tecnet Accent Innovation Award 2023*, 12 January 2023, Wiener Neustadt, Austria

List of Symbols and Abbreviations

Symbol	**Meaning**
c_{motor}	motor coefficient
$c_{calib,theor}$	theoretical printhead calibration coefficient
V_{rev}	volume pushed forward by an extruder screw revolution
ω	angular velocity of extruder screw
V_{cmd}	commanded (or requested) volume of material
ε_{rel}	relative error of extruded volume
V_{extr}	extruded volume of material, deposited by the printhead
m_{extr}	extruded material mass, deposited by the printhead
ρ_{mat}	mass density of material
v	commanded volume flow
c_{corr}	extrusion correction factor
ε	engineering strain
σ	engineering stress
A_0	original cross-sectional area
L_0	original length
L	deformed length
f	force

Abbreviation	**Meaning**
AM	Additive Manufacturing
FFF	Fused Filament Fabrication
DIW	Direct Ink Writing
IJP	Inkjet Printing
SLA	Stereolithography
DLP	Digital Light Processing
BJ	Binder Jetting
SLS	Selective Laser Sintering
LAM	Liquid Additive Manufacturing
CT	Computed Tomography
HU	Hounsfield Unit
MRI	Magnetic Resonance Imaging
STL	Standard Tessellation Language
PLA	Polylactic Acid
PDMS	Polydimethylsiloxane
EFD	Equivalent Filament Diameter
DIC	Digital Image Correlation

1 Introduction and Motivation

1.1 Anatomic models

The advancement in medical practices, science, and education is often impeded by a shortage of human donors and strict regulations on animal and human testing, as well as difficulties in repeatability due to the individuality of each human or animal anatomy. Utilizing artificial anatomical models (Figure 1.1) offers a solution to these issues, particularly in anatomy or surgical education, pre-operative planning, and testing new medical devices [1, 2]. The closer a model´s use case gets to a real patient, the more requirements the model has to comply with. While mass-produced hard-plastic models are often sufficient for anatomy education, more functional models are needed for medical training and patient-specific models are necessary for pre-operative planning. In the surgical field, anatomic models can assist in the planning of complex surgeries across various surgical specialties [3]. By rehearsing the surgical steps, they can uncover potential intraoperative complications, thus reducing the risk and length of the procedure, leading to lower costs and higher patient satisfaction [4].

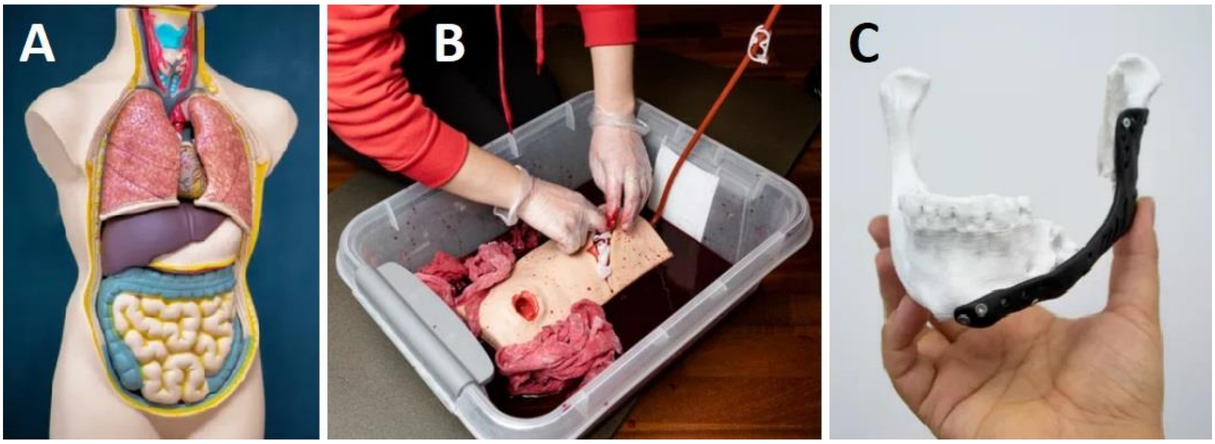

Figure 1.1: (A) hard plastic anatomic model for anatomy education; (B) functional model for wound-treatment training with simulated bleeding; (C) patient-specific anatomic model for pre-operative planning and implant customization *(source: see List of Figures and Image Credits)*

The mechanical properties of biological tissues are not uniform and are influenced by their multi-level structure of functional building blocks. While there has been significant progress in mimicking hard tissues like bone, representing soft tissues remains a challenge in anatomic models [5]. For a sufficient mechanical realism, the material properties of soft tissues

(Figure 1.2) should be accurately represented, including density, elastic modulus, hardness, tensile strength, and viscoelasticity.

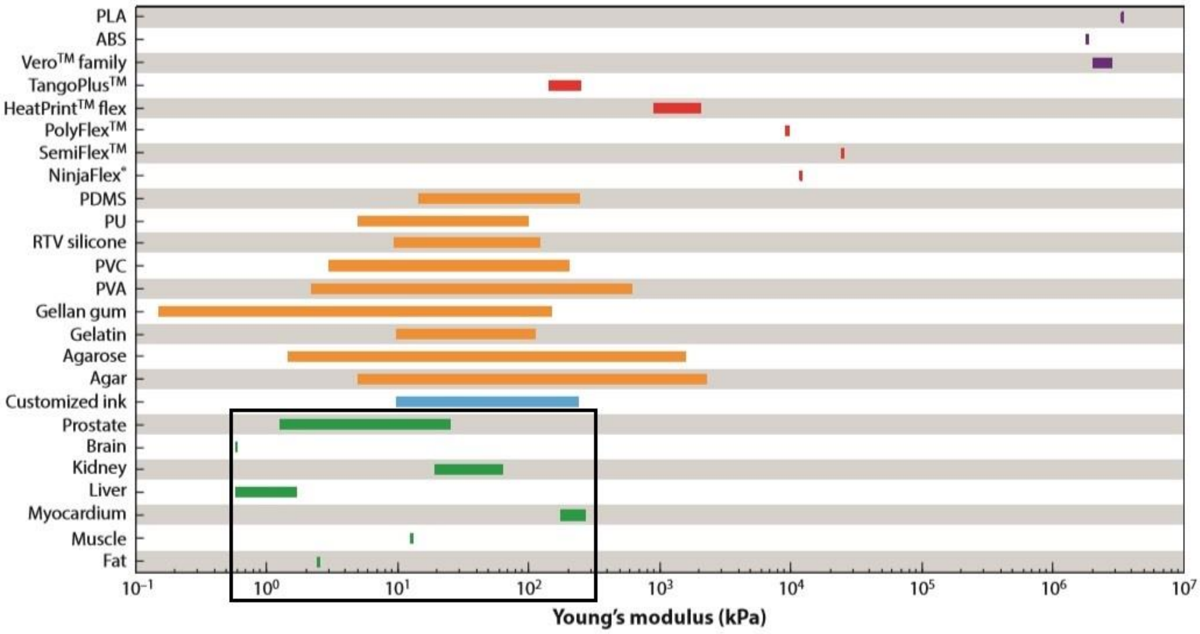

Figure 1.2: Comparing the elastic modulus of various biological tissues and commercially available soft or flexible polymers. The range of Young's modulus for various tissues is emphasized with a black frame. *(source: see List of Figures and Image Credits)*

1.2 Manufacturing of Soft Tissue Anatomic Models

The conventional methods for manufacturing anatomical models – such as casting and molding (Figure 1.3) – are ideal for mass production but they do not provide customization opportunities within a manufactured batch, hindering the use of such models for patient-specific surgical training or planning purposes [1]. Moreover, matching a patient-specific geometry is often insufficient for more advanced surgical training and planning purposes.

To meet more advanced requirements, anatomic models should imitate real-life soft tissue behavior under medical imaging systems and physical manipulation, such as touching, pressing grabbing, pinching, pulling, cutting, or suturing. This requires careful material selection in case of modelling soft tissues. To accurately mimic the mechanical behavior of soft tissues in anatomic models, soft matrix materials could be used in a composite-like structure [6]. This is challenging with conventional manufacturing techniques like casting or molding, since those usually fill a forming tool with a homogenous, bulk material (Figure 1.3). For creating anatomic models featuring multi-material structures, additive manufacturing offers better options.

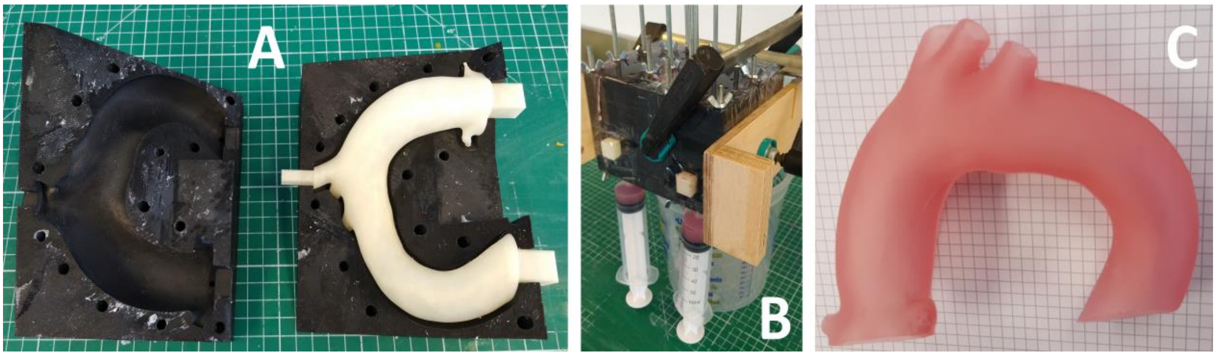

Figure 1.3: (A) molding tools to create a model of an aortic arc; (B) injection of silicone rubber using syringes; (C) the resulting model

1.3 Additive manufacturing techniques

To address the issues with patient-specificity in anatomic models, recent advancements in additive manufacturing (AM, also known as 3D-printing) technologies have made it possible to achieve high levels of model accuracy and customization even in a manufactured batch size of one [4, 7]. AM enables the physical manifestation of patient-specific geometry [5, 8], which can be derived from medical images obtained through medical imaging modalities like Computed Tomography (CT) or Magnetic Resonance Imaging (MRI). Raw data from medical imaging must undergo image segmentation to create a virtual 3D-geometry. Finally, the printer commands are generated based on this geometry.

Beyond the ability to create patient-specific geometry, certain AM technologies can also help in mimicking soft tissues by printing with soft polymer materials (Figure 1.2). Although there is a large range of various AM technologies for both, only the ones relevant to anatomic models – thus those working with polymers rather than metals or ceramics – are discussed here.

In photopolymerization-based techniques, a laser or projector is used to selectively solidify a pool of photoreactive liquid through processes called Stereolithography (SLA) or Digital Light Processing (DLP) (Figure 1.4 A) [9]. Inkjet Printing (IJP) involves depositing and solidifying photopolymers in small droplets (Figure 1.4 C) [9].

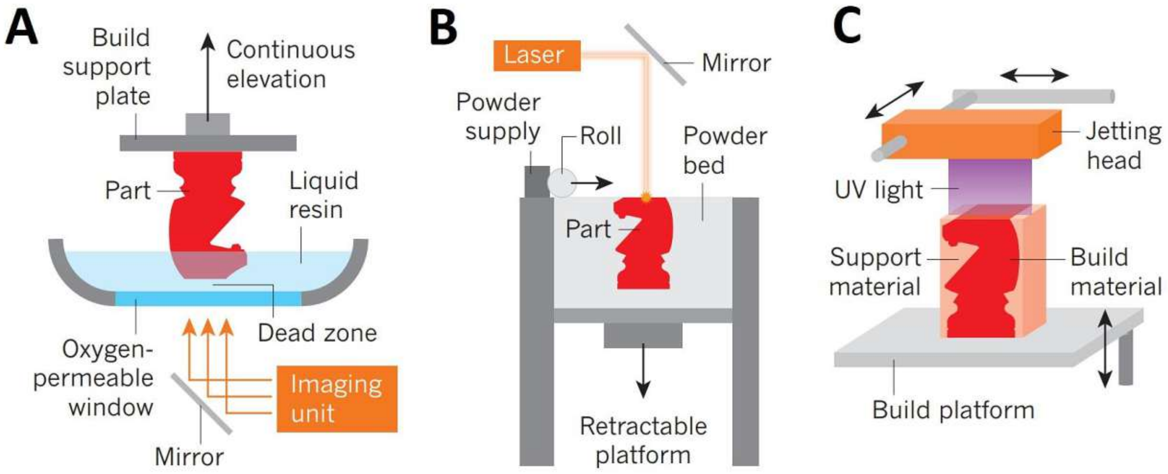

Figure 1.4: (A) Digital Light Processing; (B) Selective Laser Sintering; (C) Inkjet Printing *(source: see List of Figures and Image Credits)*

Selective Laser Sintering or Melting (SLS/M) and Binder Jetting (BJ) can also be used to process polymer powders, along with metals and ceramics that are ideal for implants and surgical tools [9]. SLS uses a high-energy laser to fuse the grains of a powder spread evenly on the building platform (Figure 1.4 B). Powders can be processed through Binder Jetting (BJ) too, in which adhesive droplets are deposited onto the powder. In this case, further chemical or thermal post-processing is required to fully solidify the part after printing [9].

Extrusion techniques, such as Fused Filament Fabrication (FFF) (Figure 1.5 A) and Direct Ink Writing (DIW) (Figure 1.5 B), use an extruder to deposit thermoplastic filaments and photoreactive or chemically or thermally cured polymers [9].

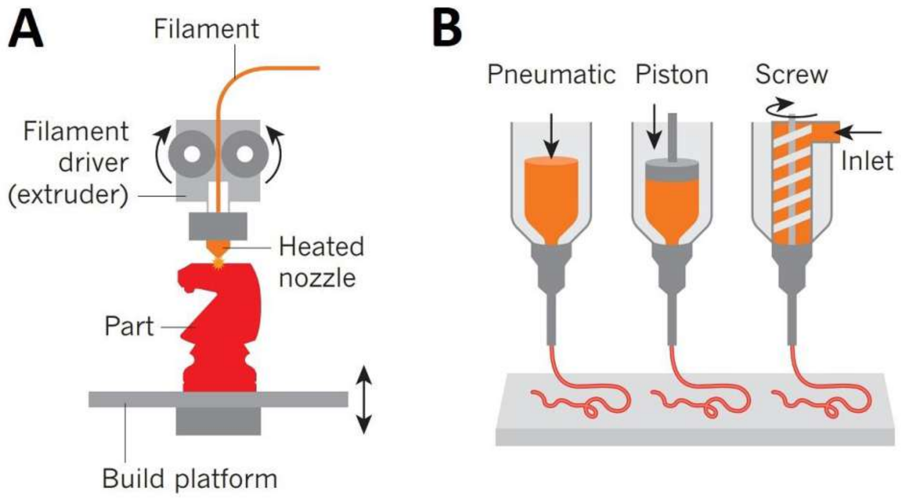

Figure 1.5: (A) Fused Filament Fabrication; (B) Direct Ink Writing *(source: see List of Figures and Image Credits)*

1.4 Additive manufacturing of soft tissue-mimicking material structures

Although all these AM techniques can reproduce patient-specific geometry upon the availability of imaging data, IJP, FFF, and DIW have the advantage of manufacturing soft multi-material structures that are useful in approximating the mechanical properties of soft tissues [10]. On the other hand, SLA and DLP both rely on a resin bath that cannot be combined with other materials, which also prevents the formation of completely enclosed air inclusions. IJP, DIW, and FFF can easily switch between materials by changing the filament, cartridge, or printhead, allowing for the creation of closed inclusions of another material, or air [10].

IJP deposits materials in small droplets or voxels and, with the proper printhead, multiple voxels of different materials can be deposited at the same time [11]. Although changing or mixing materials within a single droplet generator in IJP's printhead is challenging, IJP can still produce anisotropic properties through the inclusion of various materials [12, 13] (Figure 1.6) or even a gradient compositional change [14]. However, IJP cannot create completely enclosed hollow cavities as the droplets always require support. Furthermore, even though IJP can be faster than DIW or FFF for small prints due to its ability to deposit multiple droplets at the same time, this advantage is less clear for prints that are larger and require only a coarse resolution [9].

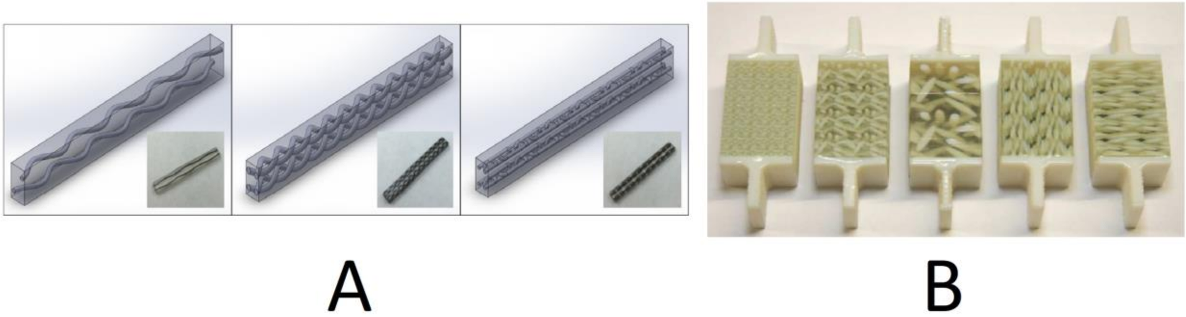

Figure 1.6: Examples of IJP-printed multi-material structuring approaches to influence mechanical properties with (A) fiber-like and (B) ellipsoidal inclusions of hard material inside a softer matrix *(sources: see List of Figures and Image Credits)*

FFF can only deposit a single material or mixture at a time, in a continuous rail [9], resulting in greater mechanical integrity of printed fiber reinforcements compared to IJP, where fibers are made of individual voxels [15]. FFF is generally more affordable compared to IJP or DIW systems due to its straightforward design and the existence of multiple competing manufacturers. These systems can process a broad range of hard thermoplastic filaments but have limitations in handling soft materials. Hence, a significant proportion of medical anatomic models made from hard plastic is produced using FFF [5]. The most convenient way to influence the macroscopic mechanical properties of an object printed with FFF is through the use of various infill patterns and various densities [16] (Figure 1.7 A). Some systems [17] combine FFF with an IJP printhead to color objects printed by FFF, which can improve the visual realism of anatomic models by depicting tissue colors more accurately. Although coloring enhances visual realism, which is crucial in anatomy education, it is not the most pressing issue in surgical education or preoperative planning [5]. Coloring, or even mixing materials with different mechanical properties can also be achieved by melting and mixing multiple filaments using a hotend with multiple inputs and single output [18] (Figure 1.7 B).

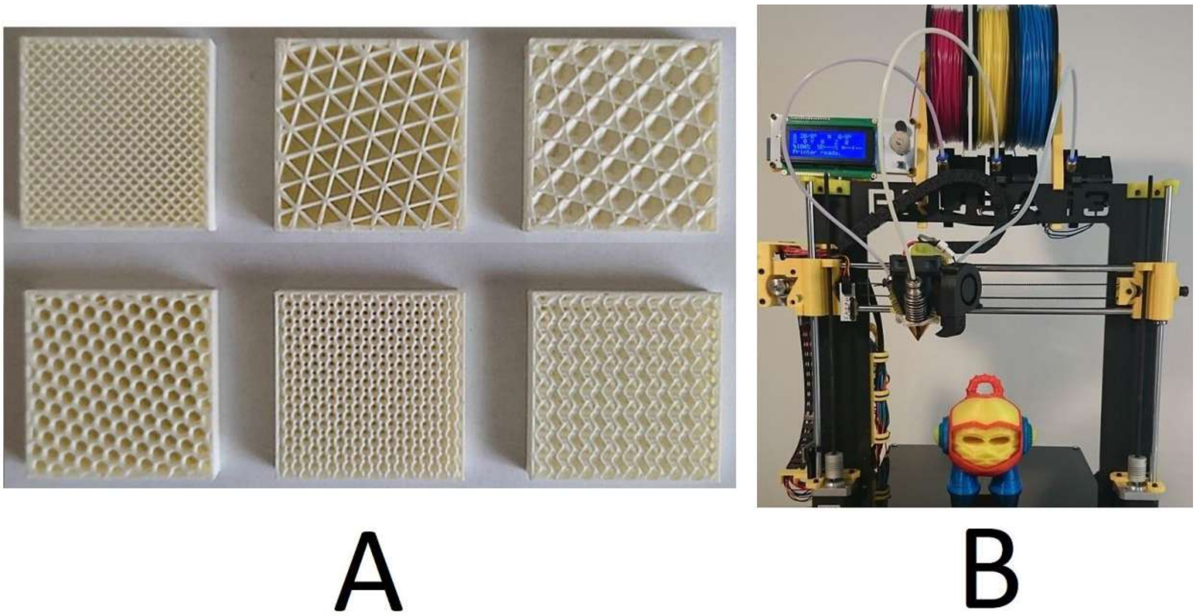

Figure 1.7: Examples of structuring approaches with FFF that can modify the mechanical properties of the printed object: (A) infill structuring and (B) diamond-nozzle multi-material printing *(sources: see List of Figures and Image Credits)*

DIW operates similarly to FFF but some experimental printheads can also generate droplets and switch between materials quickly [19]. DIW can be used to deposit hydrogels or more durable soft materials like silicones. The latter has been applied to anatomical models in some early-stage commercial services [20—24] usually focusing on reproducing the desired geometry with a single material. There are cases of hydrogels and rubbers being deposited via DIW in different publications as well [19, 25, 26]. This is usually achieved with pressurized reservoirs and controllable valves to mix and deposit the soft materials in liquid form (Figure 1.8).

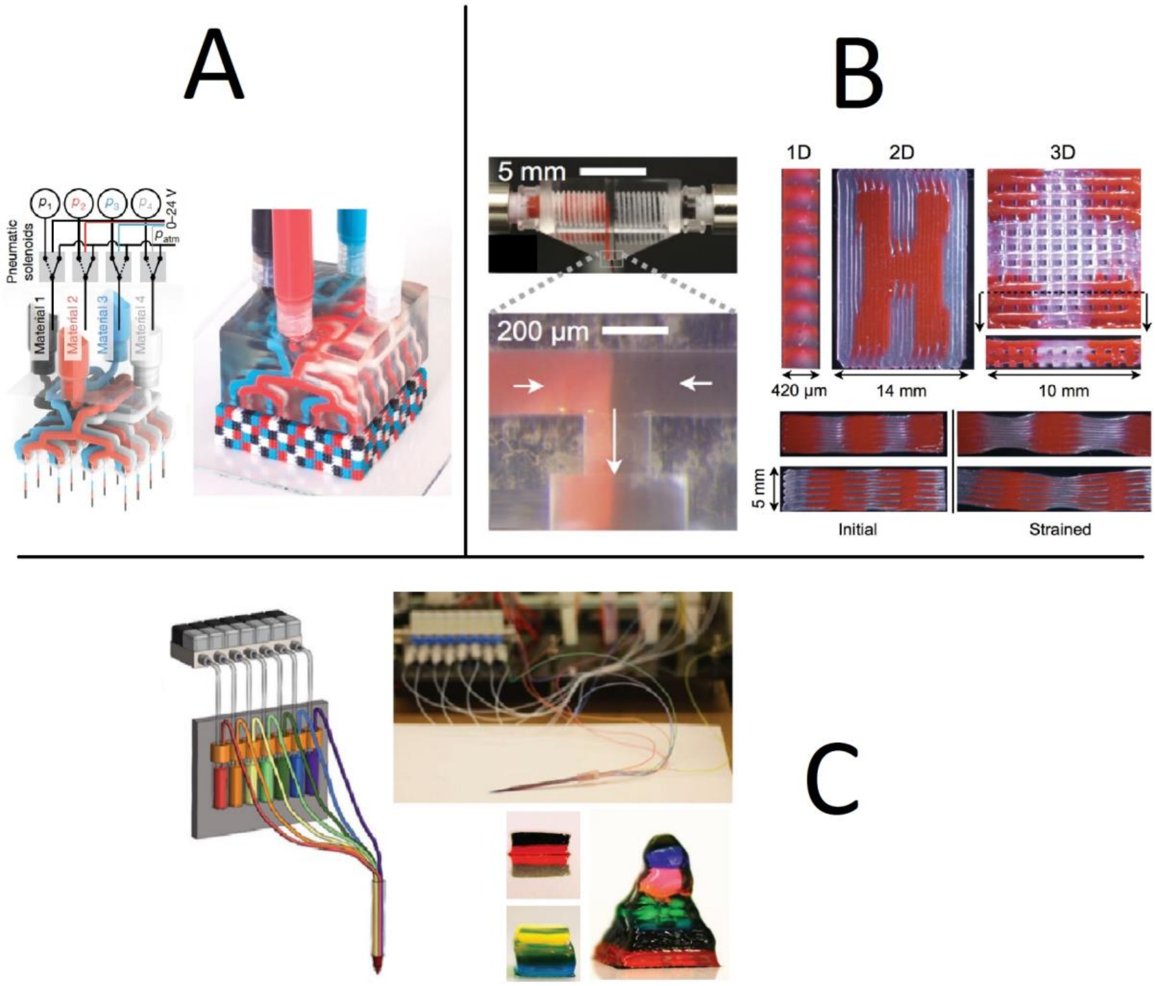

Figure 1.8: Examples of multi-material DIW printing with various soft materials: (A) epoxy, (A and B) silicone and (C) hydrogels *(sources: see List of Figures and Image Credits)*

Despite all these developments in AM, mimicking the mechanical properties of biological tissues like elasticity, hysteresis or stress-relaxation remains a gap in the domain of 3D-printed anatomic models [27], independent of chosen printing technology.

1.5 Objectives

Conventionally manufactured anatomic models suffer from limitations in terms of personalized geometries and multi-material structures for mimicking soft tissues. Both issues are simultaneously eased by currently available additive manufacturing techniques to some extent. However, even in case of additively manufactured soft-tissue models, there is a lack of experience in combining various AM techniques to create realistic anatomic models.

Combining technologies like FFF and DIW may enable promising methods to approximate the properties of soft tissues. For example, FFF-printed thermoplastics can be used as fiber reinforcement if printed into a softer matrix material deposited using a DIW printhead. Ideally, this method could harden the bulk mechanical properties compared to the original matrix material. FFF materials could also be used to build support structure underneath DIW-printed soft structures in case of more complex or unstable geometries. On the other hand, since FFF and DIW have the capability of printing closed and empty cavities even with soft materials, infill structuring can be used to alter the overall elasticity of the printed object. Alternatively, printing interconnected cavities that are filled with a viscous liquid – instead of air – may create viscoelastic mechanical behavior that is otherwise unattainable [27].

Such a combination of FFF and DIW technologies is not yet routinely used to print anatomic models. Exploring this concept may result in a technology that can produce anatomic models with highly realistic mechanical properties. This would contribute to medical education and patient safety in case of certain surgeries and may even help shortening the time to market for some novel medical instruments.

Therefore, the main objective in this research is establishing and testing an AM system which combines FFF and DIW technologies to produce objects with a large range of possible mechanical properties for medical education, surgical training, preoperative planning and medical device testing. This main objective is divided into the following goals:

- Designing and building a printer that features FFF and DIW printheads;
- Assessing printing limitations with soft materials and thermoplastic filaments;
- Printing medical image-based anatomical models with realistic biomechanical and radiological behavior as a proof of concept.

1.6 Dissertation outline

Chapter 1 provided an introduction to the state of the art in anatomic models and additive manufacturing and stated the main objectives and goals of this research.

Chapter 2 Based on self-published work [28], describes the design and construction of an additive manufacturing system that features FFF and DIW printheads to print soft materials along with thermoplastic filaments. The chosen printing system is an open-source FFF printer, extended with a set of extruders that can deposit high-viscosity fluids. This printer is tested in a set of initial printing trials, involving certain relevant geometric features and a small anatomic model.

Chapter 3 Based on self-published work [29], elaborates on printhead calibration and defines a test protocol for assessing soft materials and thermoplastic filaments from the standpoint of geometric limits, using the system described in Chapter 2. Three silicone rubbers and one thermoplastic material were chosen to print a set of test objects. Various dimensions were measured and evaluated to describe the printing limits with the used materials, and the role of material viscosity in printing accuracy.

Chapter 4 Based on self-published work [30], focuses on using the results from Chapters 2-3 and data from literature to design and print an anatomic model featuring a tissue-mimicking multi-material structure. The chosen organ for this model is the liver, and the material structuring strategy involves an infill structure of silicone rubber, filled with a high-viscosity oil to circulate within the object. Along the liver model, a set of mechanical testing specimens was printed using the chosen materials and structuring strategy. These specimens underwent a cyclical tensile testing protocol while the liver model was CT-scanned. The results from these measurements were compared with the properties of real human liver tissue, and also with the properties of the bulk silicone rubber.

Finally, **Chapter 5** provides a summarizing reflection on the overall results of this research and the future potential of the established technology.

2 Printer Concept and Realization

From the manuscript:

Development of a multi-material 3D-printer for functional anatomic models

Laszlo Jaksa, Dieter H. Pahr, Gernot Kronreif, Andrea Lorenz

Published:

International Journal of Bioprinting, October 2021, 7(4):420, DOI: 10.18063/ijb.v7i4.420

Abstract

Anatomic models are important in medical education and preoperative planning, as they help students or doctors prepare for real scenarios in a risk-free way. Several experimental anatomic models were made with additive manufacturing techniques to improve geometric, radiological, or mechanical realism. However, reproducing the mechanical behavior of soft tissues remains a challenge. To solve this problem, multi-material structuring of soft and hard materials was proposed in this study, and a 3D-printer was built to make such structuring possible. The printer relies on extrusion to deposit certain thermoplastic and silicone rubber materials. Various objects were successfully printed for testing the feasibility of geometric features like thin walls, infill structuring, overhangs, and multi-material interfaces. Finally, a small medical image-based ribcage model was printed as a proof of concept for anatomic model printing. The features enabled by this printer offer a promising outlook on mimicking the mechanical properties of various soft tissues.

Keywords

silicone 3D-printing; multi-material 3D-printing; anatomic models; soft tissues

2.1 Introduction

In medical practice and education, anatomic models are provided through using human donors, animal models, or artificial technical solutions that range from hand-crafted training models to mass-produced commercial products. In the former case of using real biological tissues, progress is often hindered by the lack of available human donors, strict regulations regarding animal and human testing, and problems in experiment repeatability due to the anatomical uniqueness of every human or animal specimen [8, 3]. Using advanced artificial anatomical models has the potential to ease these problems, especially in case of anatomy or surgical education, preoperative planning, or development of novel medical devices [1, 2]. Studies show that the use of physical anatomic models improves medical education from various aspects due to the additional haptic and spatial information students could not receive through books or screen visualizations [31—33]. In the surgical domain, anatomical models can aid the planning of complicated surgeries in a wide range of surgical specialties, since rehearsing the steps of the operation on a patient-specific model can reveal upcoming intra-operative complications [3, 34—37]. This can significantly reduce the risk and duration of certain operations, which may result in lower risk of complication and higher patient satisfaction [4]. Moreover, patient-specific models help the development of various customized implants and other medical instruments [4, 38, 39].

Traditionally, artificial anatomical models are mass-produced via casting or molding techniques, often based on population-averaged geometries [1, 38]. The materials used in such models are usually different hard and soft polymers, like thermoplastics, waxes, or rubbers. With casting and molding techniques, the mechanical properties of various represented tissues can be matched mainly through material selection, as these traditional technologies produce fully dense parts. This level of matching is often sufficient for certain mass-produced educational models [31], but the requirements of medical product development and testing, as well as preoperative planning may benefit from a better mechanical fidelity [1, 13, 15, 27, 39].

Additive manufacturing (also called 3D-printing) has become an increasingly influential group of technologies in the field of anatomic models and other medically relevant areas in recent years [4, 40, 41]. Achieving better geometric and mechanical fidelity is possible with the combination of medical imaging technologies and additive manufacturing (AM) [5]. For polymeric materials, the two dominant groups of AM techniques are based on photopolymerization and on extrusion [1]. In an extrusion-based technique called Fused

Filament Fabrication (FFF), a thermoplastic filament is pushed into a heated extruder, and deposited through a nozzle [9]. This is mostly used for bone modeling and mold-making in the field of anatomic models [1, 35]. FFF is cheaper than most other AM technologies due to its relative simplicity and fierce competition between several manufacturers. These systems can process a large variety of hard thermoplastic filaments but are limited in their ability to handle soft materials. A large proportion of available medical image-based anatomic models are made of hard plastic using FFF [5].

Liquid photopolymers can be deposited and solidified in small droplets via material jetting, which is called Inkjet Printing (IJP). Among others, it has been used to create surgical training models of aortic aneurysms and kidney tumors, skulls and fetuses [27, 42, 43]. IJP can also use multi-colored inks to make full-color objects [35, 5] and even use multiple hard and soft materials in a single print run [13, 15, 39, 44, 45]. The deposited droplets can be understood as voxels. Given the proper printhead, this allows multiple voxels of multiple materials to be deposited simultaneously [11]. While changing or mixing materials in a single droplet generator unit is difficult, IJP can easily achieve anisotropic properties by creating inclusions of various materials [12, 13, 15], or even seemingly gradient composition change [14]. However, IJP is limited in creating hollow and completely closed cavities, because droplets need support underneath them. Therefore, internal structuring is only possible if the support material can be washed or cut out after printing without damaging the printed object. From the standpoint of anatomic models, a relevant IJP printer on the market is the J850 Digital Anatomy Printer by Stratasys Ltd. (Eden Pairie, MI) [45, 46]. This offers an outstanding performance concerning geometric representation and the number of materials and colors used, including soft materials [47, 48]. However, the mechanical realism of soft tissue representing materials is still criticized [27].

Using soft materials is an intensely researched direction of AM [10]. Besides IJP, thermoset, photoreactive or chemically cured materials like certain silicones, resins or hydrogels may be deposited via extrusion as well, which is also called Direct Ink Writing (DIW) [1, 49—51]. This is used to print models of various soft structures [1, 19, 25, 26]. Most of these operate with pressurized material reservoirs with controllable valves or syringe extruders to deposit soft materials. The rheological properties of the printed material, like viscosity or thixotropy, are decisive for maintaining the shape of the printed object. Creating closed air inclusions is theoretically possible with FFF and certain DIW techniques [5].

Silicone rubbers offer a range of mechanical properties that may be ideal to represent soft tissues in anatomic models [49]. Certain silicone AM technologies are already being applied to anatomical models in some research endeavors and early-stage commercial services [20—24, 49, 52—55]. These are summarized in Table 2.1. The collaboration of Wacker Chemie AG (Munich, Germany) and ACEO (Burghausen, Germany) led to a droplet-based silicone printing technology, which relies on curing each layer of silicone with UV light, in a similar fashion to IJP [22, 56]. Meanwhile, InnovatiQ GmbH (formerly GermanRepRap GmbH, Feldkirchen, Germany) created an extrusion-based technology called Liquid Additive Manufacturing (LAM) which deposits silicone with extrusion and cures it layer-wise using a heat source [21]. The companies Deltatower GmbH (Bürerfeld, Switzerland) [23], Lynxter (Bayonne, France) [57], CR-3D (Cham, Germany) [58] have also created similar printers. The Silicone Additive Manufacturing (SAM) process is developed by Spectroplast AG (Zürich, Switzerland), a spinoff company of ETH Zürich. This method uses layer-wise photopolymerization in a liquid silicone bath [24]. Another method called Picsima by Fripp Design Ltd. (Rotherham, UK) represents a different bath-based printing approach, namely extruding the catalyst component of a two-part silicone into a bath of the base component [20]. Silicone AM may also utilize a non-planar coordinate system. Coulter *et al.* developed a printing method specialized on rotating printing surfaces, which offers unique advantages in realizing certain geometries. [52, 53]. Despite the promising development that these technologies represent, almost all focus on single-material printing. Therefore, the capabilities to tune mechanical properties are limited to porous structures with internal cavities [10].

Table 2.1: Summary of relevant commercial soft material printing technologies

Group name	**Process name**	**Principle**	**Material**
Stratasys Ltd.	J750 / J850	Droplet jetting	Photopolymers
Wacker Chemie AG	ACEO	Droplet jetting	Silicone rubbers
InnovatiQ GmbH	LAM	Extrusion	Silicone rubbers
Deltatower GmbH	Fluid ST / MT	Extrusion	Silicone rubbers
Lynxter SAS	LIQ11	Extrusion	Silicone rubbers
CR-3D GmbH	C2	Extrusion	Silicone rubbers
Fripp Design Ltd.	Picsima	Extrusion	Silicone rubbers
Spectroplast AG	Spectroplast	Vat photo-polymerization	Silicone rubbers

These AM technologies (IJP, FFF, DIW) are highly applicable to create personalized anatomic models that are geometrically unique [1]. However, geometric or color fidelity alone do not satisfy all possible needs of medical device development, surgical education, or preoperative planning. For more advanced applications, models should behave realistically under physical manipulation with hands or surgical instruments [5]. To achieve such surgical realism, the materials used to represent various biological tissues need to have similar mechanical properties to the tissues, like density, elastic modulus, hardness, tensile strength, or viscoelasticity [13, 15, 27]. While matching hard tissues like bone with AM is already a mature field, there are still many unsolved problems regarding soft tissues [5]. Most biological tissues - unlike technical materials - exhibit multi-level hierarchic structures of various functional building blocks, which often results in anisotropic and viscoelastic mechanical properties [6, 27]. This behavior could be approximated with soft-hard multi-material structures [13, 15, 39], but to date, there are no AM technologies available that can approximate a multitude of tissues [27]. Therefore, two major areas for improvement could be printing both hard and soft materials simultaneously and tuning local mechanical properties via multi-material structuring. These should happen simultaneously to produce high quality anatomic models that resemble real tissues from a mechanical standpoint [27].

2.1.1 Objectives

Combining extrusion-based AM technologies like FFF and DIW may be helpful for making more realistic anatomic models. While using FFF to produce the whole model is ineffective regarding mechanical realism, thermoplastics may be used as fiber reinforcement if printed into a softer matrix material, like a silicone rubber that is deposited by a DIW printhead. Such a concept may also work with having both the soft matrix and a harder reinforcement being deposited via DIW [59]. In any case, this strategy would allow the hardening, toughening (further referred to as “up-tuning”) of bulk mechanical properties compared to the original matrix material. Since both FFF and extrusion-based DIW can print closed and empty cavities, the weakening, softening (further referred to as “down-tuning”) of mechanical properties would also be possible [27].

Therefore, the main aim of this research was to design, build and test a 3D-printer based on the concept of combining hard and soft materials for printing more realistic anatomic models. As a proof of concept, the printer should be capable of printing at least one soft and one hard material, and thus achieve both up-tuning and down-tuning to influence mechanical properties.

Moreover, the printer should also realize thin-walled structures and closed internal cavities with the soft material, since these are relevant features in anatomic models. In this study, a 3D-printer with these features was built, and its abilities were evaluated through qualitative analysis of various printed proof-of-concept objects, including a small ribcage model based on a medical image. The applicability of the system in the field of anatomic models and the future direction of research are also discussed.

2.2 Materials and methods

2.2.1 Technology definition

The design process of this novel AM system started with a comparison of various AM technologies and their specifications, as clarifying differences is critical for choosing the right printing concept. IJP, DIW and FFF can handle different materials in the same print, which is a required feature to produce multi-material structures. Other technologies based on material jetting or vat photopolymerization, like Binder Jetting (BJ), Stereolithography (SLA) and Digital Light Processing (DLP) all use a single-material bath (or "vat") of liquid resin or powder [9]. This prevents multi-material printing, and the creation of closed air inclusions. For IJP, DIW and FFF, changing materials simply requires switching to a different filament, cartridge, or printhead. Mimicking the macroscopic mechanical properties of biological tissues through up- and down-tuning requires printing both soft and hard materials. Extrusion is preferred, to create closed internal cavities and support structures if needed. The mentioned technologies are compared considering our construction preferences in Table 2.2. Further descriptions and schematics of these technologies are available in [9] and [10].

Concerning the printing material, some silicone rubbers exhibit ideal mechanical properties to mimic various soft tissues. This also makes them a popular casting material for certain anatomic models, where a casting mould of the desired anatomy is first printed with FFF or SLA, and then filled with a two-component addition-cured silicone rubber [32, 35]. However, in multi-material printing, the adhesion of the various printing materials is important, unlike in casting. Certain single-component condensation-cured silicone rubbers may exhibit an adhesive behavior to some thermoplastic polymer materials, which makes these a promising combination in a multi-material printing scenario. Therefore, the printer should employ an FFF printhead for printing thermoplastics, and a continuous extrusion-based DIW printhead to print single-component silicone rubbers.

Table 2.2: A survey of features considering various additive manufacturing technologies, including an imaginary technology which we found ideal for anatomic models if mechanical realism is desirable

Technology	**Principle**	**Soft materials**	**Multi-material**	**Material deposition**	**Support structures**	**Closed cavities**
SLS	powder bed fusion	limited	No	spreading	powder or printed	no
BJ	material jetting	limited	No	spreading and droplets	powder or printed	no
IJP	material jetting	yes	yes	droplets	printed	limited
SLA	vat photo-polymerization	limited	No	spreading	liquid or printed	no
DLP	vat photo-polymerization	limited	No	spreading	liquid or printed	no
FFF	Extrusion	limited	yes	heated extrusion	printed	yes
DIW	Extrusion	yes	yes	extrusion or droplets	liquid or printed	yes
Ideal for anatomic models	Extrusion	yes	yes	extrusion	printed	yes

2.2.2 Printer system

For an extrusion based DIW printhead, various extrusion mechanisms like syringes, peristaltic pumps and screw extruders are available. However, for high-viscosity and high-precision applications, screw extruders were preferred. The final choice fell on a Vipro-HEAD 3/3 two-component printhead by Viscotec GmbH (Töging am Inn, Germany) [60], which enables processing either one or two single-component silicones, or a two-component silicone. In this study, only one single-component silicone rubber was used.

Regarding printer mechanics from the standpoint of printing soft and flexible materials, it is important that the building platform only moves in the axis of the building direction (usually labeled “Z”), so that it does not shake the printed objects horizontally during printing. The printer kinematics which fulfills this criterion are the so-called XY-Core and the Delta kinematics. Hardware and software formed another important aspect in the component selection. An FFF printer which does not only apply Delta or XY-Core kinematics, but also employs a control board that is open-source and easily extended with the chosen Viscotec extruder was considered highly desirable.

Finally, a Railcore II 300 ZL open-source FFF 3D-printer system [61] was chosen and modified (Figure 2.1). On this printer, the original E3D V6 FFF printhead was extended with the Viscotec Vipro-HEAD 3/3 (Figure 2.2) [60]. Silicones and other high-viscosity materials can be fed into this screw extruder with pressurized air up to 6 bars, from 55 ml cartridges, which are also mounted on the printhead. If necessary, these can be moved to the frame, which removes their volume and mass limitations, enabling a large material supply to the printhead, given sufficient feed pressure. The silicone printing nozzle is connected to the outlet of the extruder through a Luer-thread and is secured against unscrewing with a retainer part. These white Luer-adapters and retainers were custom-made for the extruder (Figure 2.2 A). A nozzle with 0.33 mm outlet diameter was selected for silicone extrusion. The original E3D V6 FFF printhead on the other side of the carriage (Figure 2.2 B) is capable of melting and depositing thermoplastic filaments through a 0.4 mm diameter nozzle.

The printer is controlled by the Duet 2 Wifi control electronics, extended with a Duex 5 extension board, operating with RepRap v1.18 firmware [62]. The system can be connected to a personal computer (PC) through a wifi network, and printjobs can be started through the Duet Web Interface, which is accessible through an internet browser running on the PC. The general printer configuration, including the printhead definitions and dosing calibration settings are done by modifying a file stored on the Duet 2 Wifi board. The slicing software used to generate G-codes for printing objects is Prusa Slicer (version 2.1), an open-source slicer originally made for filament-based printers [9]. The user can easily define a multi-material printhead and generate G-codes for multi-material FFF-DIW printjobs. No post-processing of the generated G-code files is necessary, and an extrusion correction factor can also be set to fine-tune dosing accuracy, when necessary. To start a printjob, the generated G-code files must be uploaded to the Duet 2 Wifi board through the Duet Web Interface. This way, the printer is likely also compatible with other popular slicing software, like Cura or Simplify3D.

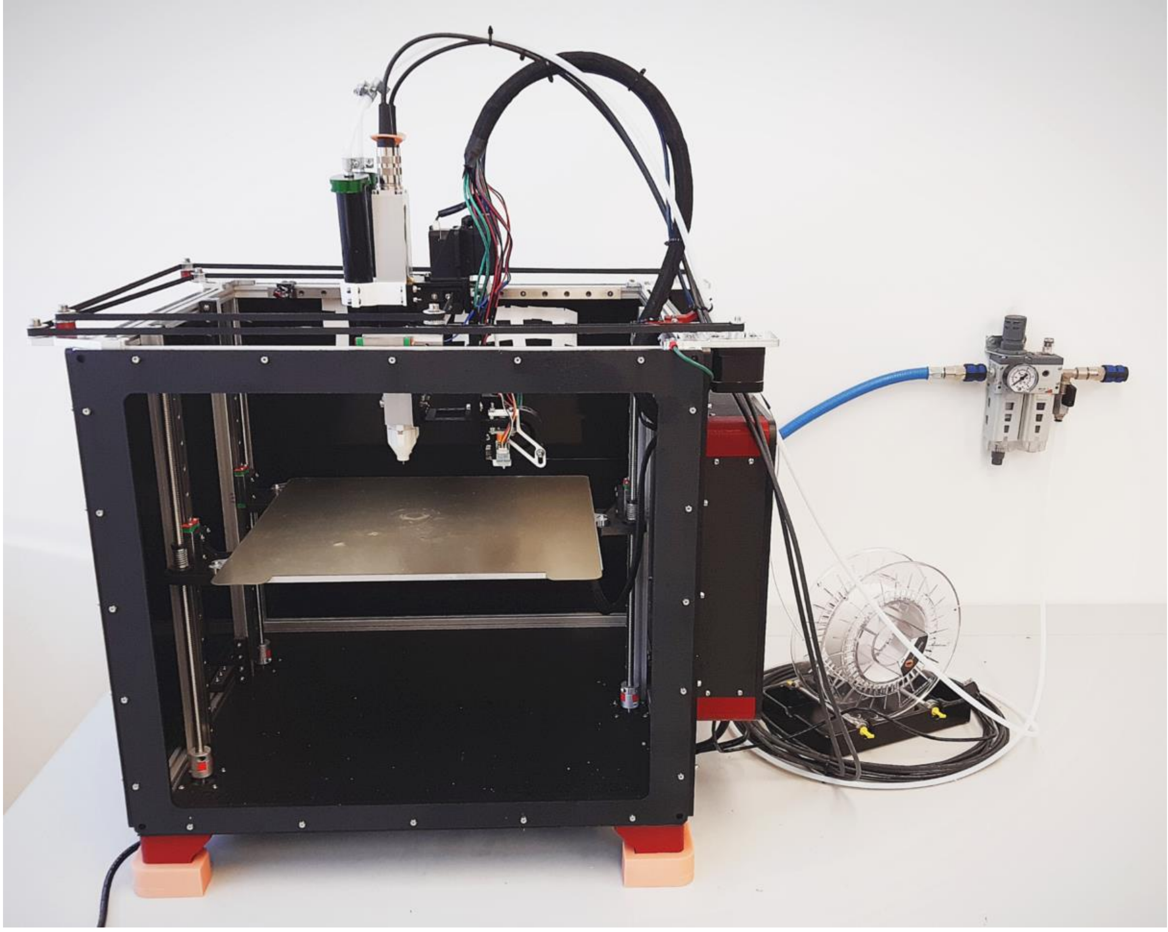

Figure 2.1: The modified Railcore II 300 ZL printer, extended with a Viscotec Vipro-HEAD 3/3 extruder

2.2.3 Materials

The selected silicone material is a high-viscosity single-component condensation-crosslinking liquid silicone rubber called Elkem AMSil 20101 (Elkem Silicones, Oslo, Norway), which was used with the Viscotec DIW printhead. This material is intended for cold extrusion therefore no heating or other means of energy input is required during printing. Moreover, a 1.75 mm diameter poly-lactic acid (PLA) filament from Fillamentum Manufacturing (Hulín, Czech Republic) was used with the E3D V6 FFF printhead in case of prints that demonstrate the multi-material capabilities. PLA was chosen as it is an easily accessible and popular FFF material.

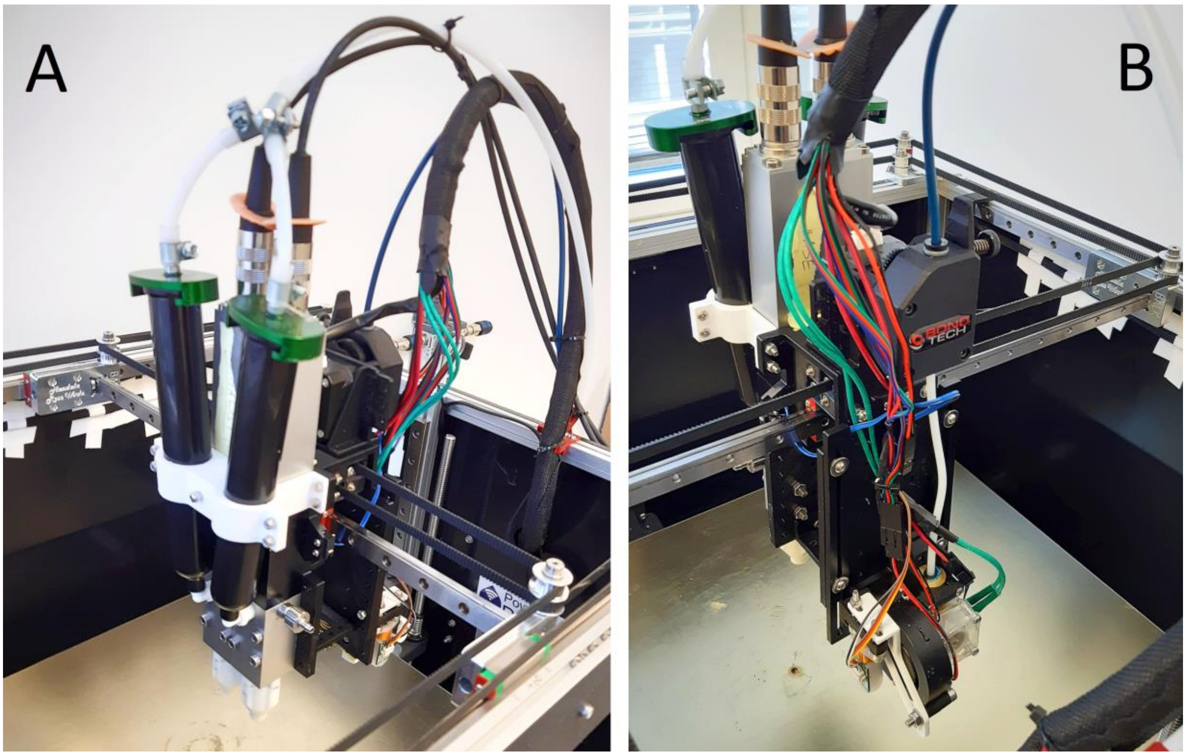

Figure 2.2: (A) Viscotec Vipro-HEAD 3/3 extruder with custom Luer-compatible endpieces; (B) the original E3D V6 filament extruder on the opposite side of the printhead carriage

2.2.4 Printing tests

For accurate dosing, the silicone printhead was calibrated for the chosen material, using a KERN EMB 200-3 scale (Kern&Sohn GmbH, Balingen, Germany). After this, 15 x 15 x 10 mm silicone blocks were printed with various speeds and layer thicknesses to find reasonable settings for further printing tests. The integrity of the printed cubes was qualitatively evaluated by observing them, and then slicing them with a blade to see if there are any internal faults (Figure 2.3).

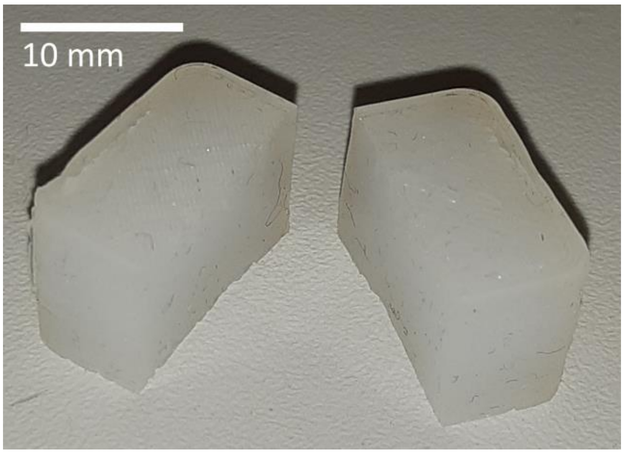

Figure 2.3: A 15 x 15 x 10 mm test block, printed after calibration, cut in half after printing

Based on the calibration prints, a printing speed of 15 mm/s and a layer thickness of 0.3 mm were chosen for further trials. Furthermore, every printed object was left on the building platform untouched for 24 hours to ensure sufficient crosslinking before any manipulation or inspection. After calibration, the system's ability to print silicone objects with closed internal cavities, infill structuring, thin-walls, and to combine silicone DIW and thermoplastic FFF was assessed by conducting six printing tests:

- In the first test, a thin-walled shell was printed, based on the same 15 x 15 x 10 mm cuboid that was used for the calibrations. In this case, only two lines of outer contour was used, resulting in approximately 0.7 mm shell wall thickness (Figure 2.4). This is relevant to anatomic models in case of printing vessels or membranes, which all feature thin walls.
- The second test involved a silicone block of the same dimensions as in the first test, but with 40% volume fraction gyroid infill structuring to simulate down-tuning (Figure 2.5).
- In the third test, a 50% downscaled version of a human bladder was printed, based on a 3D-model segmented from a CT image earlier. To test the feasibility of such a large internal cavity with overhanging areas, no support was used inside. The envelope dimensions of this downscaled bladder were approximately 35 x 30 x 25 mm, and the wall thickness was changing between 1.5 and 2 mm (Figure 2.6).
- The fourth test involved a pair 15 x 15 x 3 mm square silicone and PLA multi-material chips on top of each other. The silicone was printed on top of the PLA to simulate a situation of printing hard plastic support under a silicone structure (Figure 2.7 A).
- In the fifth test, the same model was used as in the fourth test, but now the PLA was printed on top of the silicone to simulate laying the filament as an inclusion into the silicone matrix (Figure 2.7 B).
- The sixth test was planned to give some synthesis of the features investigated through the previous text. The ribcage and the surrounding soft tissues were segmented from the CT-image of a newborn using 3D-Slicer, and the model was printed (Figure 2.8). The ribs and the support structures were printed from PLA and the surrounding soft tissue was printed from silicone. To mimic bone structure, the ribs were printed with a 30% gyroid infill, while 80% infill was used for the soft tissue.

2.3 Results

All test objects were successfully printed. The thin-walled shell of the first test (Figure 2.4) did not collapse during or after printing, despite having only 0.7 mm wall thickness.

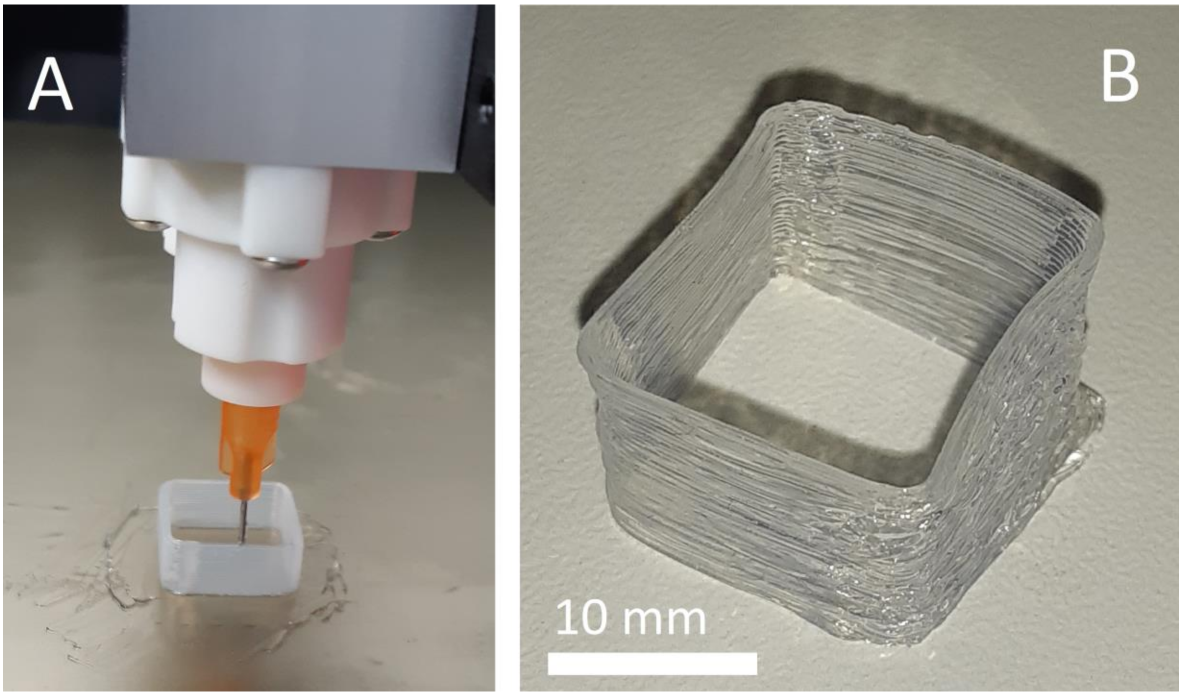

Figure 2.4: (A) Thin-walled silicone rubber shell during; and (B) after printing

The 40% gyroid block of the second test (Figure 2.5) was cut in half with a blade after crosslinking, to reveal the internal structure (Figure 2.5 C).

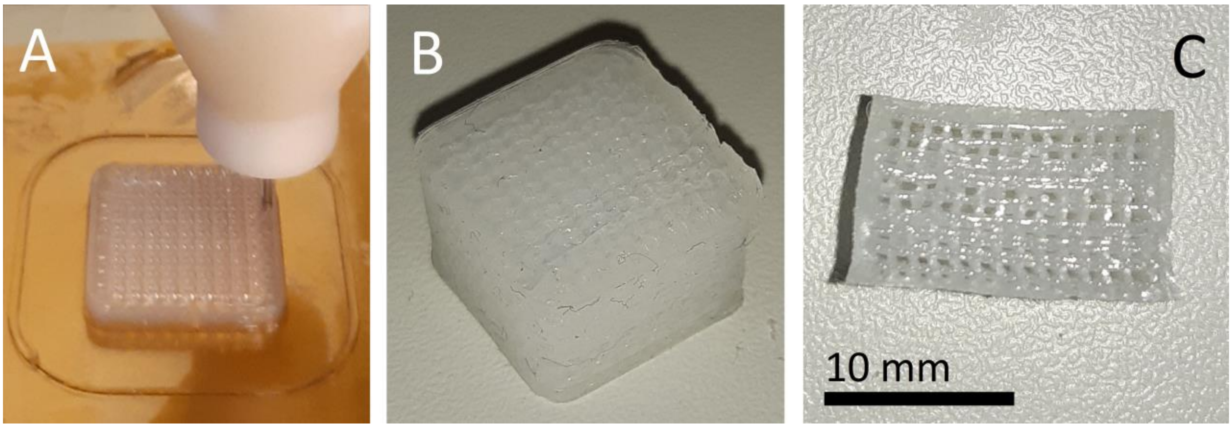

Figure 2.5: Silicone block with 40% volume fraction gyroid infill (A) during and (B) after printing, and (C) after slicing with a blade to reveal the internal structure

The downscaled bladder in the third test (Figure 2.6) had minor material integrity errors at the top due to the lack of internal support, but the external geometry stayed intact. This bladder was also cut in half after printing to reveal the internal cavity (Figure 2.6 C).

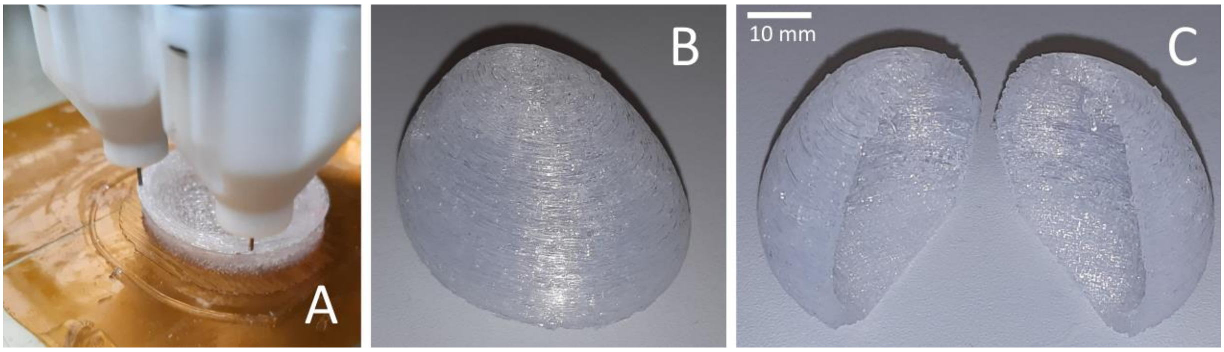

Figure 2.6: A downscaled human bladder with no internal support (A) during and (B) after printing, and (C) after slicing with a blade to reveal the internal cavity

The multi-material chips from the fourth (Figure 2.7 C) and fifth (Figure 2.7 B) tests were also printable. Moreover, in case of the fifth test, the PLA top was deformed, presumably due to printing on a soft and unstable silicone surface. After printing, the adhesion between the silicone and the PLA in the multi-material chips was evaluated by trying to manually separate the materials. The silicone was considered adhesive enough to resist this manual peeling, since the bulk silicone material was damaged before the interface.

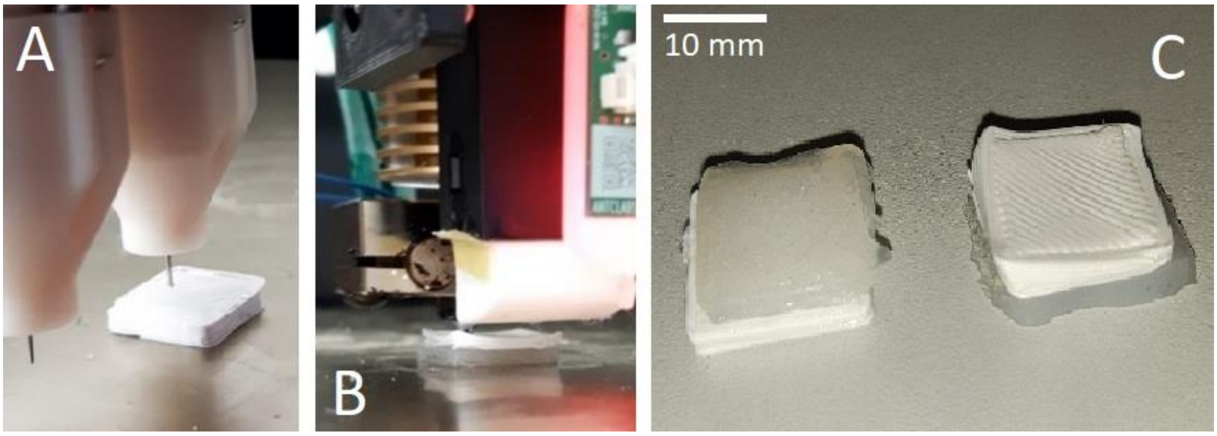

Figure 2.7: (C) Silicone-PLA multi-material chips; (A) with the silicone laid on top of the PLA; and (B) the PLA laid on top of the silicone

After seeing the success of the five previous tests, the ribcage model of the sixth test was printed to demonstrate the applicability of the printer to produce medical image-based anatomic models (Figure 2.8). No complications were experienced during the printing process, although the manual removal of the support structures was challenging due to the adhesion between the silicone and the PLA.

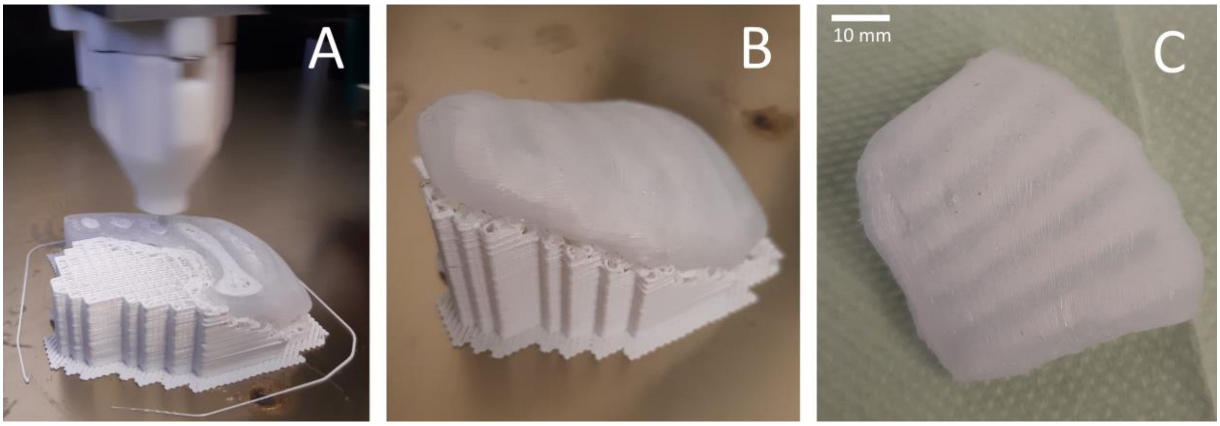

Figure 2.8: Silicone-PLA multi-material ribcage model, based on a medical image of a newborn, (A) during printing; (B) with support after printing; and (C) after support removal

2.4. Discussion

The aim of this study was to build and test a 3D-printer that enables features necessary for producing more realistic anatomic models in the future. The specifications stemming from this goal were printing multi-material structures out of at least one hard and one soft material, while also being capable of printing empty cavities, infill structures and thin-walled features. Considering the advantages and drawbacks of various additive manufacturing methods and their applicable materials, a printer was built that combines FFF and DIW technologies to print with a single-component silicone rubber and a thermoplastic PLA filament.

2.4.1 Overview of results

The printing trials demonstrated that the established technology is capable of printing objects of both materials and can print silicone with a weakened internal structure (down-tuning) or combine silicone with PLA (up-tuning). An unsupported internal cavity and a thin-walled structure were also printable with the silicone. It was shown that the FFF printhead can create hard support structures. The strong adhesion between the PLA and the silicone, that was experienced during the tests, suggests that this material combination can be applied to create more complex multi-material structures, and that the silicone must be cut away from the PLA in case of using PLA for printing support structures under the silicone. These assumptions were confirmed through the last test, where the ribcage was indeed printable with PLA support and sufficient adhesion between the silicone and the PLA. These promising outcomes imply that the technology could be used to approximate the mechanical properties of various soft biological tissues through up- and down-tuning strategies. By using the other half of the Viscotec printhead as a third extruder, the system could easily be extended to introduce a viscous fluid into printed internal cavities. Such a method, used in parallel with up- and down-tuning strategies, could possibly increase viscoelasticity [27] in anatomic models. This means that with the further development of our technology, a significant increase in anatomic model realism may be delivered, which could accelerate the development of certain medical instruments and improve medical education and preoperative planning.

2.4.2 Comparison with other technologies

From the perspective of down-tuning, the greatest limitation of concurrent technologies like IJP, BJ, SLA and DLP is their difficulty to realize completely closed and empty cavities, either because of an inherent need for support (IJP) or because of a leveled slurry or powder bath (BJ, SLA, DLP) [9]. This also applies to the Picsima silicone printing process [20], as well as the technology used by Wacker and ACEO [22], and by Spectroplast [24]. In our case, this limitation is overcome by utilizing extrusion based DIW and FFF, even though the extrusion-based processes of InnovatiQ [21], Deltatower [23], Lynxter [57] and CR-3D [58] are also free of this problem.

Considering up-tuning, IJP has a better resolution and a larger variety of applicable materials than our presented technology [13, 15, 39]. Our process can use up to three materials and can be extended to handle two more without changing the electronics. The other extrusion-based processes, along with the one of Wacker and ACEO [22] could theoretically also be extended to work with multiple materials. Meanwhile, the other methods (BJ, SLA, DLP, Picsima, Spectroplast) are confined to single material printing [9, 20, 24].

The various available IJP printer models from Stratasys (including the J750 and J850 machines dedicated for anatomic models) [45] are frequently used in literature for producing soft multi-material tissue models [13, 15, 27]. However, the biological realism of the materials that are printable with these printers is often criticized, and IJP technologies are inherently limited in terms of printing unsupported overhangs. We have demonstrated that our system can print steeply overhanging structures, which (combined with other relevant features) may enable more accurate tissue approximation than what is possible with IJP systems. Differentiating our system from other self-built silicone rubber printers, we can note that some are specialized on printing on curved surfaces [52, 53], while others use two-component silicones on a heated building platform [54, 55] and do not feature additional printheads for thermoplastics or other fluids.

2.4.3 Limitations

In case of DIW and FFF, spatial resolution, printing quality and printing speed are tightly connected process parameters, therefore the presented technology is slow compared to the shower-like droplet generation of IJP or BJ, or the scanning laser or full-layer projector of SLA or DLP. Moreover, despite the successful first prints, the system suffers from certain other limitations in its current state. If used in more complex geometries, the removal of PLA supports might damage the contact surface of the silicone. This adverse effect may be minimized by careful support design in the future.

The difficulties with removing the silicone parts from the building platform may be eased by choosing a different printing surface. It must also be pointed out, that the printing abilities were only demonstrated with one silicone and one thermoplastic material, therefore the general applicability to other materials is so far untested. A decisive factor in the compatibility of a silicone-thermoplastic combination is the adhesion between them. Qualitatively testing the adhesion strength between the silicone and PLA or other thermoplastics remains an interesting direction for further research, along with the qualitative testing of the effects of infill structuring on the mechanical properties of silicone objects.

Finally, the extent of applicability to the field of anatomic models depends not only on mechanical property tuning, but also on geometric limitations. To succeed at printing complex anatomic geometries, an optimization method should first be developed to find the ideal printing parameters. This may be done in a follow-up study by printing various basic features at different printing settings and then analyzing the integrity and accuracy of the printed features. Additionally, using the other available DIW extruder to deposit a high-viscosity filler liquid into internal cavities may provide a way to modify viscoelastic mechanical properties.

2.5 Conclusion

In this study, a novel multi-material additive manufacturing technology, targeted at facilitating the production of more realistic anatomical models was established and tested. The printable features enabled by this technology offer promising possibilities in the field of functional anatomic models. Analyzing geometric limitations, along with an evaluation of feasible mechanical properties are needed before this technology could make a significant impact in the field of medical education, device testing, and preoperative planning. However, a medical image-based anatomic model was already successfully printed in this study, implying a long-term applicability for the presented system. Moreover, besides anatomic models, the system may also have potential applications in the field of soft robotics, wearable electronic devices, or sports equipment.

3 Printing Accuracy and Limitations

From the manuscript:

Calibration Dependencies and Accuracy Assessment of a Silicone Rubber 3D-Printer

Laszlo Jaksa, Dieter H. Pahr, Gernot Kronreif, Andrea Lorenz

Published:

MDPI Inventions, April 2022, 7(2):35, DOI: 10.3390/inventions7020035

Abstract

Silicone rubbers are relatively new in additive manufacturing, with only a few commercial printing services and reports on custom-built printers available. Publications and standards on calibration and accuracy assessment are especially lacking. In this study, the printhead calibration process of a custom-built silicone printer is explained, and a set of test objects is proposed and evaluated. The printer in use is based on an open-source filament printer, capable of multi-material printing with silicone rubbers and thermoplastic polymers. Three different high-viscosity single-component liquid silicone rubbers and one polylactic acid thermoplastic filament were used as printing materials. First, the calibration process of the silicone printhead was conducted, and the dependency of the dosing accuracy on silicone viscosity, nozzle diameter and extrusion speed was evaluated. Second, various test specimens were proposed and printed to characterize the accuracy and geometric limitations of this printer. These test parts contained features such as thin walls, slender towers, small holes and slots, unsupported overhangs and bridges. It was concluded that silicone viscosity strongly affects geometric inaccuracies. Design recommendations were deducted from the results, advising for wall thicknesses above 1 mm, slenderness ratios below 2, bridging lengths below 2 mm and unsupported overhang angles below 30°.

Keywords:

silicone rubber; 3D-printing; additive manufacturing; calibration; test geometry; viscosity

3.1 Introduction

Additive manufacturing (AM), or 3D-printing, is a group of technologies that is transforming industry and research by enabling the manufacturing of complex objects from various materials without expensive tooling [63—67]. One of the quickly advancing domains is 3D-printing with various fluid materials that solidify upon some physical or chemical stimulus after deposition, resulting in a soft object. This includes a large variety of materials, such as hydrogels, waxes or rubbers, and the deposition may happen via continuous extrusion or droplet jetting [9]. Such materials have been used in regenerative medicine and tissue engineering [10, 26, 50]. Recent advances in material development also made extrusion-based silicone rubber printing available [10, 19, 49] to a greater variety of medical and technical applications. While silicone rubber 3D-printing is already available through various commercial services and off-the-shelf printers [21, 57, 58], detailed reports [68] on custom-built systems—including their setup and calibration—are scarce, even though custom-built systems may offer greater freedom in customization and lower costs in research.

Every AM technology—including silicone printing—bears various strengths and weaknesses, which must be considered in any given use case. Geometric accuracy and object stability are important factors, since those influence design freedom. To help the assessment of geometric capabilities of various AM systems, several studies [69—73] and standards [74—76] have been published. Geometric limitation assessment is a prerequisite for any further testing, such as mechanical characterization [77—79], since it is preferrable to confirm the manufacturability and accuracy of test specimens before proceeding to further assessments that require those specimens. In theory, printing such test objects should help the user decide whether the system in question can manufacture a desired product.

However, many recommended test objects are general and ignore significant differences among various technologies [73, 76]. Moreover, it is often recommended to test the feasibility of different features on a single, complicated test object [73]. While this approach simplifies and speeds up the assessment process, it makes dimension measurements from certain angles difficult and also runs the risk of “failure transfer”, where the failure of one feature influences the success of another feature, potentially distorting test results. Failure transfer is especially dangerous in extrusion-based technologies, where the material from a failed feature can accumulate on the nozzle and get transferred—and deposited—elsewhere, influencing the success of other features.

Even though such shortcomings are pronounced in both filament-based and fluid extrusion-based printing, they are more neglected in the case of fluid printing including silicone printing. In addition, apart from failure transfer, the viscosity and crosslinking kinematics of the used silicone material may also influence geometric limitations in the case of extrusion-based silicone printing. The evaluation of unstable features, such as high slenderness ratio columns, thin shells, small holes and slots, unsupported overhangs and bridges, is important in many use cases, but test methods and specimens designed for this technology—that also reduce the chance of failure transfer—seem to be lacking in current standards and best practice.

3.1.1 Objectives

There were two aims to this study. The first was to investigate the influence of extrusion speed, nozzle diameter and printing material viscosity on the dosing accuracy of a custom-built silicone 3D-printer through a detailed calibration protocol. This may be helpful for researchers aiming to build their own custom fluid printer based mostly on open-source filament printer hardware, firmware and software. The second aim was to establish an accuracy testing approach that limits the chance of failure transfer and points out the geometric limitations with regards to various geometric features. The identified geometric limits were also compared to those of thermoplastic filament printing, which was used as a benchmark due to the fact of its popularity and accessibility.

3.2 Materials and methods

The printer system used in this study was introduced elaborately in [28]. Therefore, the description given here for the printer and the materials is relatively brief. However, the calibration process of the fluid extruder and the objects for geometric limitation assessment are described in detail.

3.2.1 Printer and materials

The custom 3D-printer used in this study (Figure 3.1) consisted of a Railcore II 300 ZL 3D-printer [61] (Railcore Labs LLC, Goshen, IN, USA) with an E3D V6 filament hotend [80, 81] (E3D-Online Ltd., Oxford, UK), extended with an additional Viscotec Vipro-HEAD 3/3 dual fluid extruder [60] (Viscotec GmbH, Töging am Inn, Germany). In the latter, the liquid silicone rubber material is fed from two 55 ml pressurized cartridges (both at 6 bars) to each extruder. Only one of the two silicone extruders was used for printing in this study, but both may be used within the same print run. The system relies on a Duet 2 control board [62], which allowed for the extension with the Viscotec extruders.

Three high-viscosity single-component liquid silicone rubbers—AMSil 20101, 20102 and 20103, Elkem Silicones (Lyon, France) [82]—were used. These materials are designed for 3D-printing via extrusion at room temperature, therefore no heating or other means of energy input is required during printing. After printing an object, minimum 24 h of curing time is allowed on room temperature before any evaluation. The filament printhead used a poly-lactic acid (PLA) thermoplastic filament (Material 4 Print GmbH, Löhne, Germany), which was chosen as a benchmark due to the popularity and accessibility of PLA filaments. The properties of all used printing materials are visible in Table 3.1 based on the corresponding technical datasheets. Further description concerning the initial test prints with the printer system is available in [28]. The materials are referred to as 20101, 20102, 20103 and PLA in the rest of this study.

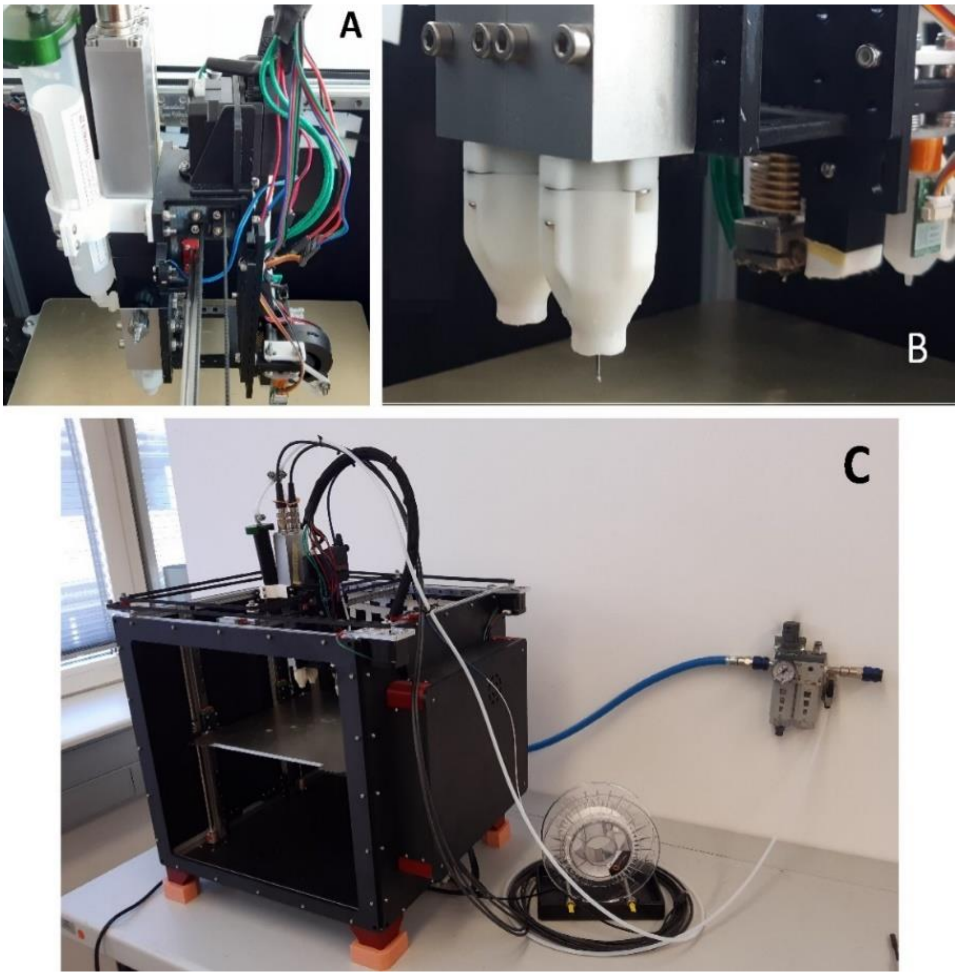

Figure 3.1: (A) The moving unit of the Railcore II 300 ZL printer, extended with the Viscotec Vipro-HEAD 3/3 fluid extruder; (B) the printing nozzles; (C) the printer frame

Table 3.1: The relevant datasheet properties of the printing materials used in this study

Material properties	**Elkem AMSil 20101**	**Elkem AMSil 20102**	**Elkem AMSil 20103**	**Material4Print PLA**
Dynamic viscosity [1] (at 1 Hz) in Pa·s	410	535	1080	-
Dynamic viscosity [1] (at 10 Hz) in Pa·s	120	115	270	-
Density in g/cm³	1.01	1.30	1.04	1.24
Recommended printing temperature in °C	RT[3]	RT	RT	210
Recommended bed temperature in °C	RT	RT	RT	60
Tensile strength [2] in MPa	1.1	3.5	2.5	60
Elongation at break [2] in %	400	540	500	-
Hardness (Shore A)	18	34	25	-
Color	translucent	white	translucent	black

[1] *of fluid material; the frequency values should be understood as sinusoidal excitation frequencies in a standard viscometer. The lower viscosity values at higher frequencies (higher shear rates) imply thixotropy;*

[2] *of solid material;*

[3] *at room temperature*

3.2.2 Fluid extruder calibration

The calibration of the Viscotec fluid extruder for each material is important before any printing test, since the material viscosity and the nozzle diameter both influence the dosing accuracy. The following description focuses on the fluid extruder and 3D-printer used in this study, but the calibration process is likely transferable to other extruders and printer electronics. All data handling in this work was done in Microsoft Excel, and PrusaSlicer v2.3.0 (Prusa Research a.s., Prague, Czech Republic) was used for print file generation.

Typically, in filament 3D-printers, a calibration coefficient, expressed in step/mm (of filament), is used to define the relationship between stepper motor revolution and filament pushed forward. However, no filament is present in a fluid extruder, which makes it more practical to "think" in terms of extruded fluid volume instead of extruded length. This necessitates the calculation of an "equivalent filament diameter" (EFD) to use a fluid extruder with a filament 3D-printer firmware and slicer software (PrusaSlicer) that "thinks" in filament length instead of volume. It was practical to use a 1.13 mm EFD that returns approximately 1 mm^3 volume (V_1) for each 1 mm of "equivalent filament" length (h_1), as expressed in Equation (3.1) below, based on the simple formula of the volume of a cylinder.

$$\mathrm{EFD} = \sqrt{\frac{4V_1}{h_1\pi}} = \sqrt{\frac{4}{\pi}} \cong 1.13\ \mathrm{mm} \qquad (3.1)$$

$$\text{where } V_1 = 1\ \mathrm{mm}^3;\ h_1 = 1\ \mathrm{mm}.$$

This value was used in the slicer software as a filament diameter setting. After this step, the value of the calibration coefficient (normally given in step/mm) in the printer configuration file may also be interpreted in step/mm^3.

Each of the two extruders of the printhead featured an encoded DC motor with built-in position controller, which—from the perspective of the printer control board—made them appear as high angular resolution stepper motors with a 12500 step/revolution constant. Furthermore, each extruder revolution pushed forward a theoretical volume of 30 mm^3 according to the manufacturer. However, the flow rate stemming from these theoretical values is heavily influenced by fluid viscosity and nozzle diameter. Knowing the theoretical volume/revolution (V_{rev} = 30 mm^3) and the motor step/revolution (c_{motor} = 12500 step/rev) values, the theoretical calibration coefficient ccalib,theor can be calculated according to Equation (3.2).

$$c_{\mathrm{calib,theor}} = \frac{c_{\mathrm{motor}}}{V_{\mathrm{rev}}} = \frac{12500}{30} \cong 417\ \frac{\mathrm{step}}{\mathrm{mm}^3} \qquad (3.2)$$

In our case, this returned a 417 step/mm^3 (or step/mm of 1.13 mm imaginary EFD filament) theoretical calibration coefficient. However, this had to be adjusted due to the significant losses caused by a high fluid viscosity and small nozzle diameter. Characterizing this underextrusion for a given material, nozzle and speed was conducted by first commanding the printer to extrude a desired amount of material volume (V_{cmd}, usually 500 mm^3 in the measurements). A weighing of the extruded material followed (m_{extr}) using a KERN EMB 200-3 laboratory scale

(Kern&Sohn GmbH, Balingen, Germany), calculating the extruded volume (V_{extr}) through known density (ρ_{mat}, values in Table 3.1) and, finally, calculating the relative volume error (ε_{rel}) as shown in Equation (3.3). This was repeated for different extruder screw rotation speeds (ω) up to 20 revolutions per minute, which covered the practical range of usage in this study. The graph resulting from the data points shows the connection between extrusion volume error and extrusion speed, assuming a constant material viscosity and density, feed pressure and nozzle diameter.

$$\varepsilon_{rel}(\omega) = \frac{V_{\mathrm{extr}}(\omega) - V_{\mathrm{cmd}}}{V_{\mathrm{cmd}}} \cdot 100\% \tag{3.3}$$

$$\text{where } V_{\mathrm{cmd}} = \mathrm{const};\ V_{\mathrm{extr}}(\omega) = \frac{m_{\mathrm{extr}}(\omega)}{\rho_{\mathrm{mat}}}.$$

These extrusion volume errors along the various nozzle diameters and extrusion speeds were compared across the three silicone rubber materials and three different nozzle diameters. The most practically relevant nozzle diameter (0.41 mm) was chosen for further investigations, since this is the closest to the standard 0.40 mm nozzle diameter frequently used in thermoplastic filament printing, making it an ideal choice for comparisons. The extrusion volume error with the chosen 0.41 mm nozzle was speed dependent over the available extrusion speed range. This is problematic, since in each printhead move, there is an initial acceleration and final deceleration phase, swiping over all possible extrusion speeds between zero and the desired printing speed. If one could only compensate extrusion errors with a single constant multiplier in the firmware—by changing the calibration coefficient—one would need to accept either an overextrusion at the beginning and end of each printed line, or an underextrusion in the middle, because the extrusion error is speed dependent.

Fortunately, the firmware of the Duet 2 control board offers a feature that allows for a compensation with a second-order polynomial. The extrusion correction factor c_{corr} is calculated according to Equation (3.4), where A, B and C are user-defined parameters, and v is the volume flow command understood in mm^3/s. Equation (3.4) also defines the connection between this volume flow command and the extruder screw rotation speed. The nonlinear compensation feature is accessible with G-code command M592 in the Duet firmware, for which the proper syntax and a further description are found in [83]. It must be noted that the naming of the parameters (i.e., A, B and C) is slightly different here than in [83] to make reading easier.

$$c_{\mathrm{corr}} = \mathrm{A}v^2(\omega) + \mathrm{B}v(\omega) + \mathrm{C} = \frac{1}{1 + \varepsilon_{rel}(\omega)} \tag{3.4}$$

$$\text{where } v(\omega) = \frac{\omega \cdot \mathrm{V_{rev}}}{60} = \frac{\omega}{2}\,\frac{\mathrm{mm}^3}{\mathrm{s}}.$$

The extrusion correction factors were calculated from the relative volume error data obtained in the previous step, using three materials, focusing on a 0.41 mm nozzle diameter. While the A and B parameters of the fitted second-order polynomials provided the parameters to use in G-code command M592, the parameter C helped us determine the true calibration coefficient ($c_{\mathrm{calib,true}}$) according to Equation (3.5).

$$c_{\mathrm{calib,true}} = c_{\mathrm{calib,theor}} \cdot \mathrm{C} \tag{3.5}$$

For this study, the parameters in Table 3.2 ensured sufficient printing accuracy for the test specimens described in the following subsection. With this, the extruder calibration for each silicone material is complete. The process described in this subsection may serve as a reference for other self-built systems featuring similar deposition principles but different hardware and firmware.

3.2.3 Assessment of geometric limitations

The next step after calibration was evaluating the geometric limitations of the printer with the given materials. This was conducted by printing different geometries that demonstrated various features both in the layer plane and the building direction. The chosen geometries are described further in this subsection. To minimize the chance of “failure transfer”, different geometries were printed in different print runs, while all replicates of the same geometry were printed sequentially within the same run.

All silicone rubber and PLA objects were printed at a constant 30 mm/s printing speed, understood as the target travel speed of the printhead on its trajectory. All objects, except shells, featured a double-line contour, a 0.3 mm layer thickness and a 100% rectilinear infill structure with the infill printed before the contour in each layer. The silicone rubber objects were printed with a 0.41 mm nozzle with direct contact to the unheated building platform. The PLA objects were printed at a 200 °C nozzle and a 60 °C building platform temperature with a 0.4 mm nozzle and with two raft-layers to increase stability during printing. These rafts were removed after printing. All printing was conducted in an ambient temperature of 20–25 °C and 60–70% relative humidity; both were logged with an EL-USB-2 logging device (Lascar Electronics Ltd., Salisbury, UK) and placed next to the printer. After printing, the silicone objects were left in the same ambient conditions to crosslink for 24 h; then, they were carefully removed from the building platform using a razor blade.

The silicone nozzle diameter choice of 0.41 mm (0.4 mm for filaments) also determines the minimal feature size with the given nozzle by constraining the thickness of a single extruded line. In our case, this extruded line width was 0.46 mm (0.45 mm for filaments) according to PrusaSlicer. Thus, a theoretical minimal positive feature size in the layer plane could be determined without the need to print specimens. It must be noted that printing thinner or thicker lines is also possible through certain G-code generator software tools [84] or controlled under- or overextrusion, but such manipulations were out of the scope of this study.

All printed objects (Figure 3.2) were weighed, and their mass was compared to their expected mass as a form of quality control. A ±5% relative mass error was chosen as an acceptance threshold to qualify for further assessment. Once qualified, the integrity of the qualitative specimens (Figure 3.2 A, B) was judged based on visual inspection, while the deformations of quantitative specimens (Figure 3.2 C–E) were examined further with profilometers.

To qualitatively assess the stability of thin walls, cylindrical shells 20 mm in height and 20 mm in diameter were printed with triple-, double- and single-line walls (Figure 3.2 A). Each wall thickness variation was printed 3 times per material, and they were assigned to 3 outcome categories based on visual inspection of integrity: "failed" (meaning that the object completely collapsed); "deformed" (meaning that the object suffered some deformation but maintained its posture); "successful" (meaning that the object was printed as intended as far as a simple visual inspection was concerned).

Examples of this categorization is visible in Figure 3.3. The same categorization was performed with a series of full cylinders, where 2 levels for height (i.e., 10 and 20 mm) and 3 levels for diameter (i.e., 3, 6 and 9 mm) were used (Figure 3.2 B). These resulted in various height-over-diameter ratios (slenderness ratios) that provided insight into how nozzle forces influenced the success of "tower-like" structures. A "success score" was also introduced as a convenient way of comparing overall stability across materials in the case of thin-walled cylinders and tower-like features. Cases of failure did not contribute to the score, while deformed and successful objects contributed 0.5 and 1 points, respectively. With 3 replicates of 9 different object configurations (Figure 3.2 A, B), this success score could range from 0 to 27 points for each material.

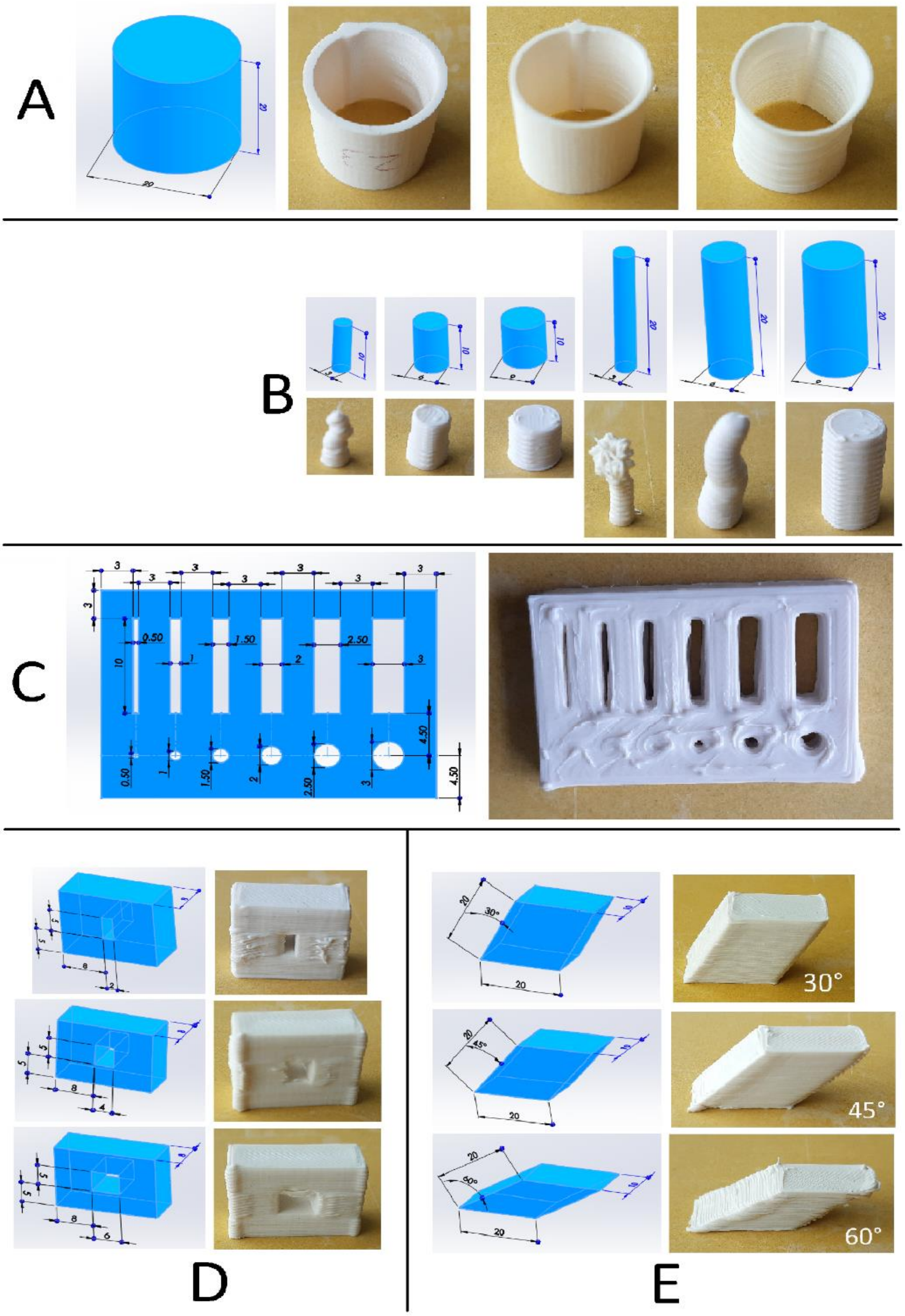

Figure 3.2: Test objects for the geometric limitation assessment printed from 20102 silicone rubber, where the assessed features were (A) thin walls; (B) tower-like structures; (C) holes and slots in the layer plane; (D) unsupported bridges; and (E) unsupported overhangs

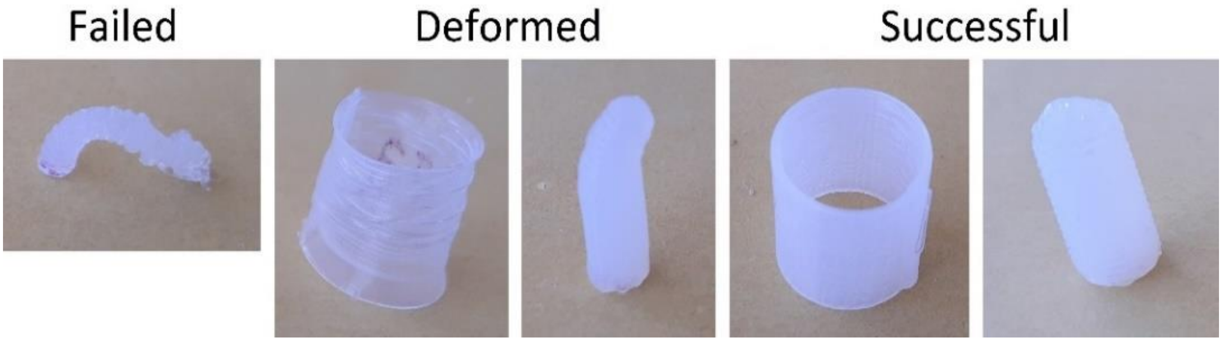

Figure 3.3: Examples of the categorization for cylindrical shells and columns made of 20101 silicone

Quantitative insight into the behavior of small through holes and slots in the layer plane was provided by printing 6 rectangular plates with holes and slots of various diameters and widths, respectively, with each material. These dimensions ranged from 0.5 to 3 mm with 0.5 mm increments, while the overall dimensions of the plate were 31.5 x 22 x 5 mm (Figure 3.2 C). Each hole diameter and slot width were measured manually on a Nikon V-12 manual profile projector (Nikon Corp., Tokyo, Japan) once, in the direction parallel with the longer side of the object.

To quantitatively evaluate bridging stability, rectangular blocks were printed with a rectangular through hole (or “window”) of 5 mm in height and varying widths (2, 4 and 6 mm) in their middle (Figure 3.2 D). The width of this through hole represented the bridge length, since closing this feature required unsupported bridging movement during printing. The envelope height and thickness of these rectangular blocks were 15 and 8 mm, respectively, while the width was 16 mm plus the bridge length. For the evaluation of overhangs, parallelogram blocks of 20 mm side lengths (all parallelogram sides) and 10 mm in thickness were printed with 30°, 45° and 60° overhang angles measured downwards from vertical (Figure 3.2 E). Each configuration of these bridge and overhang specimens was printed 6 times per material.

The bridge and overhang specimens were evaluated using an OGP MVP Smartscope 300 automatic profilometer (QVI Inc, Rochester, NY, USA). A custom measurement program was written to determine the geometric inaccuracies of the unstable areas of the specimens automatically. In the case of overhangs, this meant comparing the non-overhanging side of the parallelogram block to the overhanging side by measuring their distance at 10 evenly distributed points for the 45° and 60° specimens and 11 points for the 30° specimens as explained by Figure 3.4 A. For the bridge specimens, the sagging of the bridge was measured through 10 evenly distributed points along the bridge length as shown in Figure 3.4 B. In the case of the PLA bridge specimens, some stringing between the "bridgeheads" caused the measurement program to confuse the strings with the actual bridge in some cases, corrupting approximately 8% of the data points. These largely outlying values were easy to identify and were removed from the data set. After the measurements, the average errors and their deviations were calculated for all quantitative specimens. Finally, the correlation coefficients between the silicone viscosity values (Table 3.1) and all average errors were calculated.

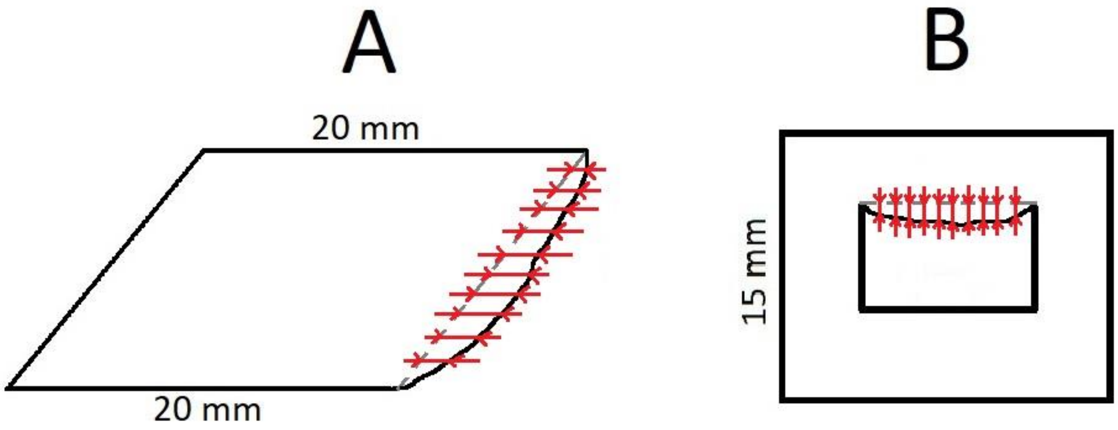

Figure 3.4: Measured dimensions on the overhang (A) and bridge (B) specimens

3.3 Results

The extrusion volume error curves—calculated using Equation (3.3)—of silicone material 20103 are visible in Figure 3.5 with three different nozzles. The results with the other two silicones showed similar trends, but the nonlinearities were somewhat less pronounced due to the lower viscosities.

Applying Equation (3.4) to the data points shown in Figure 3.5, in the case of the 0.41 mm nozzle, provided the required compensation factors for the precise material dosing. These factors are visible in Figure 3.6. Fitting a second-order polynomial to the factors in Figure 3.6 reveals the parameters A, B and C as defined by Equation (3.4). The same steps were repeated for the other two silicones (also in Figure 3.6), and the resulting parameters are shown in Table 3.2. The second-order "A" coefficients were neglected in all three cases due to the fact of their near-zero value, even though smaller nozzle diameters would likely yield more pronounced A values. Moreover, the "true" calibration coefficients in Table 3.2 were calculated using Equation (5). These were directly used in the printer firmware as step/mm values.

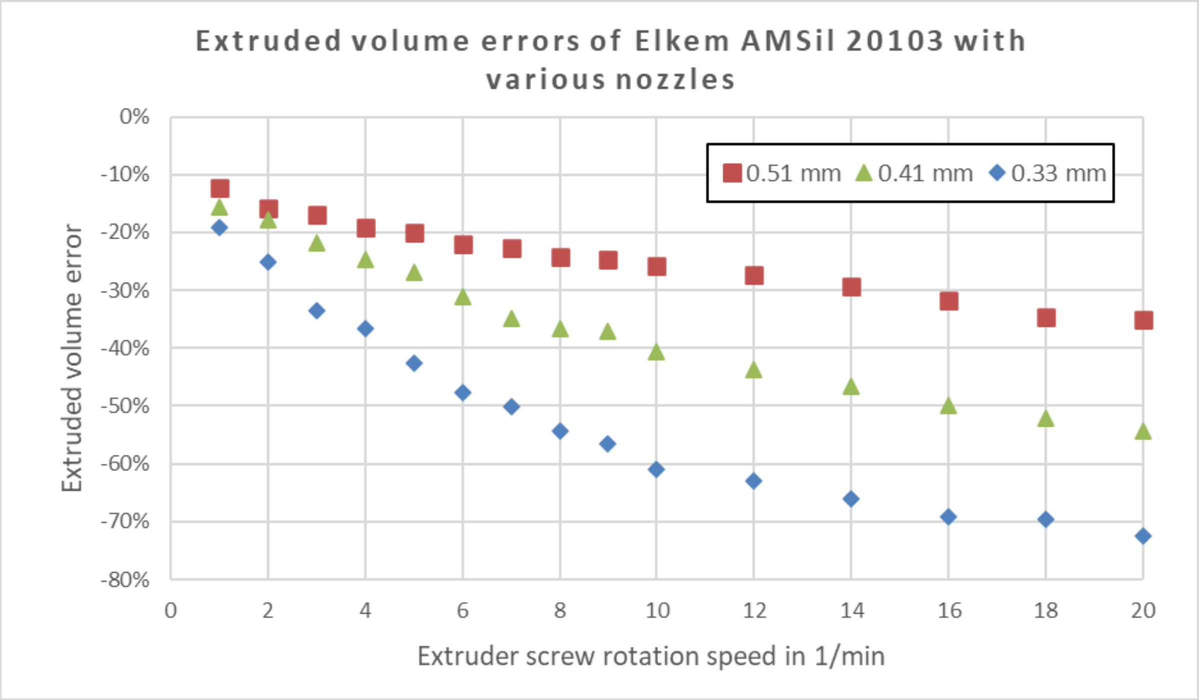

Figure 3.5: Extruded volume errors against extrusion speed with three different nozzle diameters using the 20103 silicone (the other two silicones showed similar behavior)

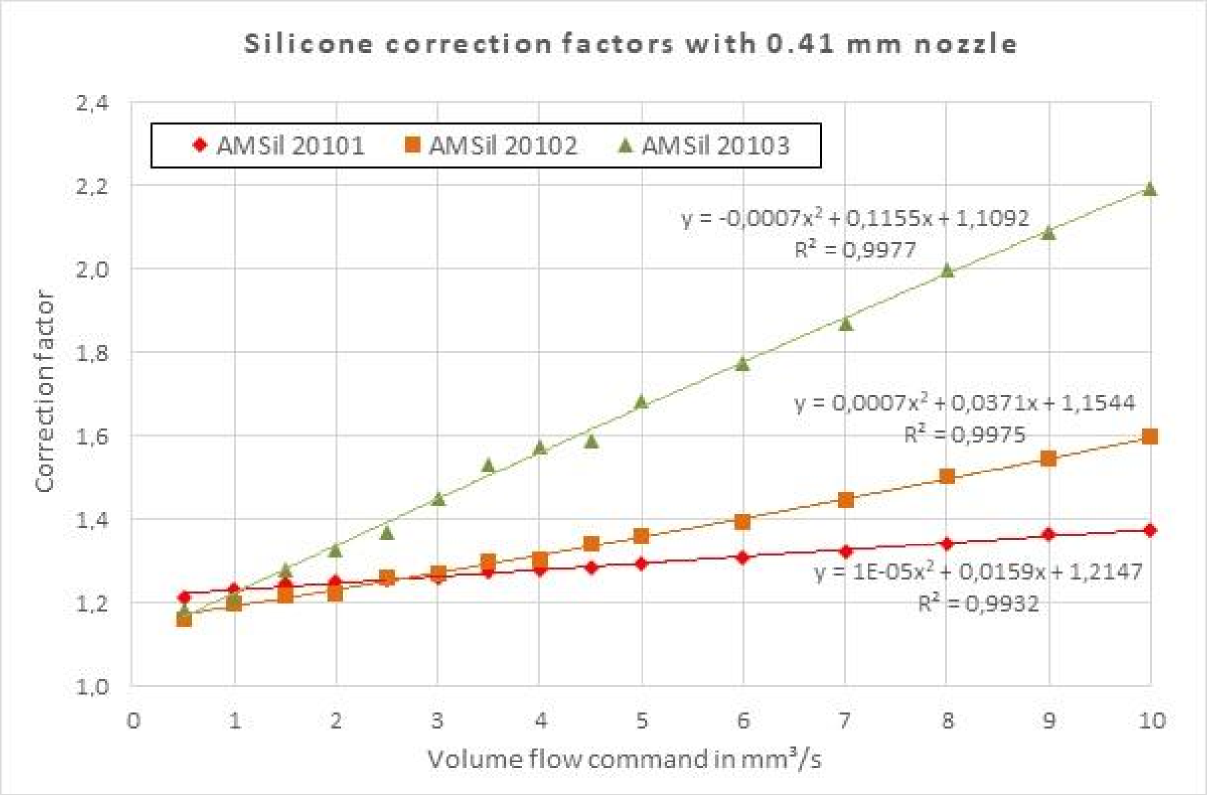

Figure 3.6: Compensation factor curves based on the volume error measurement results of all three silicone materials with a 0.41 mm nozzle diameter

Table 3.2: Compensation parameters and calibration coefficients for the used materials

Material	**A**	**B**	**C**	**True calibration coefficients [2] in step/mm³**
20101	0	0.0159	1.2147	506
20102	0	0.0371	1.1544	481
20103	0	0.1155	1.1092	462
PLA [1]	-	-	-	837

[1] *Nonlinear compensation was not used for the E3D V6 filament printhead, and the calibration coefficient should be understood in step/mm.*

[2] *These coefficients were used in the printer configuration file, and for silicones, they were only valid if the "filament" diameter in the slicer software was set to our EFD value, namely, 1.13 mm.*

After ensuring proper dosing accuracy on the silicone printhead through calibration, all of the specimen types presented in Figure 3.2 were printed, with three replicates per level for the qualitative specimens (i.e., shells and columns) and six replicates per level for all other specimens., After weight check, the overall relative mass error of all printed objects was 0.52 ± 2.17%, and all objects were within the permitted range of ±5%. This way, the effectiveness of the calibration process of the silicone printhead was verified, and all printed objects qualified to further assessment. Meanwhile, the PLA specimens showed an overall relative mass error of 0.26 ± 1.32%, and all specimens were within a ±4% range.

The results of inspecting the cylindrical shells and columns are summarized in Table 3.3, showing that there was no case of variability for the same material and geometry: all three objects always fell in the same category. The success scores of the materials showed that the PLA outperformed the silicone prints and that higher silicone viscosity had a stabilizing effect.

Table 3.3: Results after qualitative visual observation of thin shells and columns, with each object categorized as “Failed” (Fail.), “Deformed” (Def.) and “Successful” (Succ.)

Object	**20101**			**20102**			**20103**			**PLA**		
	Fail.	Def.	Succ.	Fail.	Def.	Succ.	Fail.	Def.	Succ.	Fail.	Def.	Succ.
Shell-1 line	0	3	0	0	3	0	0	3	0	0	0	3
Shell-2 line	0	0	3	0	0	3	0	0	3	0	0	3
Shell-3 line	0	0	3	0	0	3	0	0	3	0	0	3
Column [1] H10 x D3	3	0	0	3	0	0	3	0	0	0	3	0
Column H10 x D6	0	0	3	0	0	3	0	0	3	0	0	3
Column H10 x D9	0	0	3	0	0	3	0	0	3	0	0	3
Column H20 x D3	3	0	0	3	0	0	3	0	0	0	3	0
Column H20 x D6	3	0	0	3	0	0	0	3	0	0	0	3
Column H20 x D9	0	3	0	0	0	3	0	0	3	0	0	3
Success score [2]	0	3	12	0	1.5	15	0	3	15	0	3	21
	15			16.5			18			24		

[1] *In the case of columns, H refers to height in mm, and D refers to diameter in mm.*

[2] *A material’s “Success score” was determined by giving 0 points after failed, 0.5 points after deformed, and 1 point after successful objects including all shells and columns. This metric helps the comparison of materials.*

The objects with holes and slots of various sizes in the layer plane (Figure 3.4 C) provided information both on the minimal feature size that stays open, and the offsets that occur in the case of these two types of features. The results from the manual profilometer measurements of six replicates are found in Table 3.4. Both the average dimensional errors and their standard deviations were further averaged for both feature types (i.e., holes and slots) and for all features for each material, allowing a comparison of material performances. The PLA object produced less error variability but similar error magnitude to silicone objects.

Table 3.4: Results from the manual profilometer measurements on the holes and slots specimens

Feature	**20101**			**20102**			**20103**			**PLA**		
	Closed (of 6)	Error average in mm	Error SD in mm	Closed (of 6)	Error average in mm	Error SD in mm	Closed (of 6)	Error average in mm	Error SD in mm	Closed (of 6)	Error average in mm	Error SD in mm
Hole [1] D0.5	6	-	-	6	-	-	6	-	-	6	-	-
Hole D1.0	6	-	-	6	-	-	6	-	-	6	-	-
Hole D1.5	6	-	-	5	-1.26	-	6	-	-	6	-	-
Hole D2.0	1	-1.37	0.38	1	-1.11	0.11	2	-0.93	0.10	6	-	-
Hole D2.5	0	-1.04	0.26	0	-1.13	0.47	0	-0.70	0.28	0	-0.67	0.07
Hole D3.0	0	-1.12	0.25	0	-1.00	0.33	0	-0.97	0.14	0	-0.63	0.07
Slot [1] W0.5	5	-0.27	-	2	-0.25	0.05	2	-0.21	0.17	6	-	-
Slot W1.0	2	-0.40	0.22	1	-0.26	0.07	0	-0.03	0.18	0	-0.43	0.02
Slot W1.5	0	-0.34	0.16	0	-0.35	0.19	0	0.02	0.04	0	-0.38	0.03
Slot W2.0	0	-0.27	0.16	0	-0.25	0.14	0	0.02	0.05	0	-0.39	0.05
Slot W2.5	0	-0.30	0.14	0	-0.27	0.13	0	0.05	0.08	0	-0.47	0.04
Slot W3.0	0	-0.22	0.12	0	-0.23	0.10	0	-0.14	0.34	0	-0.47	0.05
Hole Avg.	-	-1.18	0.30	-	-1.12	0.30	-	-0.87	0.17	-	-0.65	0.07
Slot Avg.	-	-0.30	0.16	-	-0.27	0.11	-	-0.05	0.14	-	-0.43	0.04
Combined Average [2]	-	-0.59	0.21	-	-0.61	0.18	-	-0.32	0.15	-	-0.49	0.05

[1] *In the case of both holes and slots, D refers to the hole diameter in mm, and W refers to slot width in mm.*

[2] *The average values for all objects of a given material was taken to aid comparison between materials.*

The bridge and overhang specimens helped us characterize the stability of unsupported features. The automatic profilometer measurement results based on six specimens of each level of each object type are presented in Table 3.5. The average sagging and standard deviation values (of six replicates) were also further averaged here for both object types to allow for a comparison across materials.

Table 3.5: Results from automatic profilometer measurements on the bridge and overhang specimens

Object	**Level**	**20101**		**20102**		**20103**		**PLA**	
		Sagging average in mm	Sagging SD in mm	Sagging average in mm	Sagging SD in mm	Sagging average in mm	Sagging SD in mm	Sagging average in mm	Sagging SD in mm
Bridge	2 mm	0.554	0.151	0.683	0.164	0.596	0.422	0.571	0.399
Bridge	4 mm	0.959	0.171	0.857	0.177	1.015	0.416	0.703	0.435
Bridge	6 mm	1.311	0.293	1.335	0.351	1.599	0.545	0.595	0.288
Overhang	30°	0.961	0.205	1.409	0.194	1.092	0.162	0.026	0.298
Overhang	45°	1.557	0.586	1.779	0.711	1.786	0.586	0.805	0.569
Overhang	60°	3.732	1.775	3.382	1.942	3.937	1.999	0.479	1.013
Bridge Average		0.941	0.205	0.959	0.231	1.070	0.461	0.623	0.374
Overhang Average		2.083	0.855	2.190	0.949	2.271	0.915	0.436	0.627
Combined Average [1]		1.512	0.530	1.574	0.590	1.671	0.688	0.530	0.500

[1] *The average values for all objects of a given material was taken to aid comparison between materials.*

The last rows of Tables 3.3–3.5 all contain some form of averaging over all results in each test, concerning each material separately. These values were introduced to help us evaluate material performance in a general manner and to reveal correlations between silicone rubber flow viscosity and geometric freedom. The respective correlation coefficients were calculated and are shown in Table 3.6.

Table 3.6: Correlations between silicone viscosity and results seen in Tables 3.2–3.5

Material	**20101**	**20102**	**20103**	**Correlation coefficient with viscosity at 1 Hz**	**Correlation coefficient with viscosity at 10 Hz**
Viscosity at 1 Hz in Pa·s (from Table 3.1)	410	535	1080		
Viscosity at 10 Hz in Pa·s (from Table 3.1)	120	115	270		
Correction factor model B parameter (from Table 3.2)	0.016	0.037	0.116	1.000	0.974
Correction factor model C parameter (from Table 3.2)	1.215	1.154	1.109	-0.907	-0.803
Cylinder/column success score (from Table 3.3)	15	16.5	18	0.940	0.851
Holes/slots combined average error in mm (from Table 3.4)	-0.59	-0.61	-0.32	0.973	1.000
Holes/slots combined average error standard deviation in mm (from Table 3.4)	0.21	0.18	0.15	-0.901	-0.794
Bridges/overhangs combined average sagging in mm (from Table 3.5)	1.512	1.574	1.671	0.976	0.911
Bridges/overhangs combined average sagging standard deviation in mm (from Table 3.5)	0.530	0.590	0.688	0.979	0.917

3.4 Discussion

The goals of this study were to demonstrate the calibration process of a fluid extruder using experimental firmware features (Section 3.2.2) to establish a test method to evaluate the geometric limitations of this type of silicone printing compared to thermoplastic filament extrusion (Section 3.2.3) and, finally, to reveal dependencies on silicone viscosity concerning geometric stability and accuracy.

3.4.1 Assessment of geometric limitations

The results from the qualitative stability tests (Table 3.3) show that all three silicone rubbers struggled to maintain form in the case of a single-line cylindrical shell and that the PLA material—unsurprisingly—outperformed silicones in this regard. This suggests that a minimum of two contour lines should be used in case of printing similar structures with silicone rubbers, implying a minimum wall thickness of approximately 0.92 mm using a 0.41 mm nozzle. The 10 mm tall columns were stable with all materials down to 6 mm in diameter, which yields a slenderness ratio of 1.67. In this case, the PLA material performed similarly to the silicones. On the other hand, the 20 mm tall silicone columns (except for 20101, which never succeeded here) were only successful with a 9 mm diameter (slenderness ratio 2.22), while it was also possible to print the 6 mm diameter versions with PLA (slenderness ratio 3.33).

A potential explanation for the difference between PLA and silicone performance may be found in the bending stress caused by the nozzle swiping over the top of the columns during printing [79, 85] while the bottom of the column was fixed (given sufficient adhesion). As silicones take several hours to crosslink, the columns remain highly compliant during the whole print run, which yields greater deformations under similar nozzle forces, limiting the printable slenderness ratio range. As a rough design guideline, assuming a 0.41 mm nozzle and 30 mm/s speed, it may be concluded that a tower-like structure should be avoided with silicone rubbers under a diameter of 6 mm or—for greater diameters—above a slenderness ratio (height over diameter) of two. According to the success scores in Table 3.3, it can also be stated that PLA generally outperformed the silicone rubbers in terms of printing thin walls and slender columns.

Looking at the holes and slots of various dimensions printed in the layer plane (Table 3.4), it is surprising to see that silicone rubbers slightly outperformed PLA in terms of minimal printable hole and slot size. The diameter limits for where holes started closing were 1.5 and 2 mm for silicones and PLA, respectively, while the limit for slot width was 0.5 mm for both. The average error values show that a negative offset should be used for such features while designing the object, and the offset values were approximately 1 mm for holes and 0.2 mm for slots in the case of silicone rubbers, while a higher variability should be expected for holes than for slots. This offset seemed independent of the width or diameter as long as the feature was not closed, so considering relative errors instead of absolute ones is likely impractical. The difference between hole and slot errors may be related to surface tension, as the material in the fluid state may “pull itself together” easier if deposited into a small circle as opposed to a long slot. However, the authors are uncertain of this explanation, and this difference would deserve further investigation.

Both the sagging values of silicone rubber bridge and overhang specimens and their standard deviations (Table 3.5) showed a strong correlation with the respective bridge length or overhang angle levels. This is not surprising, as one would intuitively expect longer bridges and steeper overhangs to become more deformed [73]. However, the same was not true in every case for PLA specimens, and those generally showed lower average sagging values but similar standard deviations when compared to silicones. It must be noted that printing such objects of thermoplastic materials with a 100% infill percentage is not how this technology is used in most cases of prototype manufacturing, especially above a certain object volume. Instead, the standard practice is having a few contour lines and filling the inside of the object with a much looser infill density (10–40%, for example) [86]. In the case of our objects, this may have resulted in somewhat lower sagging values due to the better heat dissipation. Irrespective of this remark, the goal in this study was to compare the exact same geometries. Even though this was not optimal for thermoplastic filament printing, the PLA outperformed the silicones in terms of unsupported feature stability, nevertheless.

3.4.2 The effect of viscosity

In the silicone datasheets, two kinds of dynamic viscosity are given (Table 3.1). One is measured (by the material supplier) with a viscometer at a 1 Hz excitation frequency, the other at 10 Hz. For all three silicone rubbers, the 1 Hz viscosity was much higher than the 10 Hz viscosity, implying that all three fluids were strongly thixotropic, or shear-thinning. This makes them ideal for cold extrusion-based 3D-printing, since they flowed relatively easily when pushed through the extruder, but they remained stable once deposited, within some limits outlined in Section 3.4.1. above. One would therefore rightfully expect that higher viscosities lead to better stability and, thus, more geometric freedom. This hypothesis was confirmed by the correlation coefficients in Table 3.6. The viscosities at both frequencies showed strong (positive or negative) correlations with volume losses during extrusion with the stability of shells and columns, with the offsets of holes and slots, with the sagging of bridges and overhang and with the variability of outcomes in any of the listed cases.

One must keep in mind that correlation does not equal causation, and that several factors could have influenced the results as outlined in the following section. However, the fact that so many different markers of material performance are so strongly correlated to viscosity let the authors conclude, with a relatively high degree of confidence, that in the case of cold extrusion-based silicone rubber 3D-printing, both extrusion losses and geometric freedom increase with material viscosity.

3.4.3 Limitations

While the printer firmware offers a versatile nonlinear compensation method for precise extrusion, the material datasheets do not include a tolerance range on density or viscosity values. Since the calibration process relied solely on datasheet density values, this may have affected the calibration quality. Moreover, the ±5% relative weight error was a relatively coarse range of acceptance for the printed objects. This may have contributed to the variabilities seen in Tables 3.3–3.5. Possible deviations from the datasheet viscosity values and actual change in viscosity due to the fact of temperature fluctuations (20–25 °C) in the environment may also have affected the results [87]. In addition, the printing tests were only conducted at a single printing speed of 30 mm/s and a single nozzle diameter of 0.41 mm, as those represent a representative use case of filament printing, which was used as a basis of comparison.

Concerning the used geometries, cylindrical shells are relatively stable structures compared to rectangular or triangular shells, for example. The diameter and height are expected to influence the wall thickness limit where the structure starts to collapse. Choosing larger dimensions may have resulted in a higher minimum wall thickness. A similar statement could be found for every geometry used in this study, but it was necessary to make dimensioning choices without a firm standard or guideline available. Dimensions and levels were chosen such that they entailed practically feasible printing times and material consumption, covered the expected performance range of the used printing principles and allowed measurements with simple profilometers. Similar tests with more speed levels and nozzle diameters and even materials may be conducted to deepen the knowledge about this technology. The same testing protocol may also be used with different extrusion-based printer systems, since a comparison of the results would likely reveal useful design ideas concerning the entire mechanical structure of a printer.

3.4.4 Summary of identified guidelines

Concerning this type of silicone printing with a 0.41 mm nozzle and 30 mm/s printing speed, the most important calibration and design guidelines and material selection recommendations collected through this study are summarized below:

- Avoid thin walls with a thickness below 1 mm;
- Avoid column-like structures of a diameter below 6 mm or a slenderness ratio (height over diameter) above two;
- In the layer plane, increase slot widths by 0.2 mm and hole diameters by 1 mm compared to the nominal size;
- Use support structures in case of a bridge length over 2 mm or overhang angle over 30°;
- Higher material viscosity will likely increase overall geometric accuracy and stability, but also the extrusion losses, so more significant compensation is needed;
- Lower speed will reduce extrusion losses, requiring less compensation;
- Smaller nozzle diameters will increase the level of detail but also the extrusion losses, so more significant compensation or lower speed is needed.

3.5 Conclusion

In this study, a calibration process of a fluid printhead for extrusion-based silicone rubber 3D-printing was developed, and a set of accuracy test geometries was realized with a custom-made printing system. The results revealed that traditional thermoplastic filament printing slightly outperforms silicone printing in geometric accuracy and feature stability, even though reaching a comparable performance with soft materials, such as silicones, is still impressive. It was found that silicone viscosity influences both compensation requirements during calibration and geometric accuracy and stability during printing. A set of design recommendations were identified based on these results. The implications of the uncovered dependencies on material viscosity may aid material suppliers in their product development. Relying on open-source, self-built machines for fluid printing research is encouraged by the authors, since such systems allow a great freedom of customization without warranty breach, and they may be set-up for a lower total cost than the currently available commercial silicone printers. Both the calibration and the geometric testing protocol presented in this study may save other workgroups some precious time and effort when building or calibrating their own machines or optimizing printing parameters.

4 Proof of Concept for Printing Tissue-Mimicking Materials

From the manuscript:

3D-printed multi-material liver model with simultaneous mechanical and radiological tissue-mimicking features for improved realism

Laszlo Jaksa, Othniel J. Aryeetey, Sepideh Hatamikia, Katharina Nägl,
Martin Buschmann, Dieter H. Pahr, Gernot Kronreif, Andrea Lorenz

Published:

International Journal of Bioprinting, March 2023, 9(3):721, DOI: 10.18063/ijb.721

Abstract

Anatomic models have an important role in the medical domain. However, soft tissue mechanical properties' representation is limited in mass-produced and 3D-printed models. In this study, a multi-material 3D-printer was used to print a human liver model featuring tuned mechanical and radiological properties, with the goal of comparing the printed model with its printing material and real liver tissue. The main target was mechanical realism, while radiological similarity was a secondary objective. Materials and internal structure were selected such that the printed model would resemble liver tissue in terms of tensile properties. The model was printed at 33% scaling and 40% gyroid infill with a soft silicone rubber, and silicone oil as a filler fluid. After printing, the liver model underwent CT-scanning. Since the shape of the liver is incompatible with tensile testing, tensile testing specimens were also printed. Three replicates were printed with the same internal structure as the liver model and three more out of silicone rubber with 100% rectilinear infill to allow a comparison. All specimens were tested in a four-step cyclic loading test protocol to compare elastic moduli and dissipated energy ratios. The fluid-filled and full-silicone specimens had initial elastic moduli of 0.26 MPa and 0.37 MPa, respectively, and featured dissipated energy ratios of 0.140, 0.167, 0.183 and 0.118, 0.093, 0.081, respectively, in the 2nd, 3rd, and 4th loading cycles. The liver model showed 225±30 Hounsfield units (HU) in CT, which is closer to real human liver (70±30 HU) than the printing silicone (340±50 HU). Results suggest that the liver model became more realistic in terms of mechanical and radiological properties with the proposed printing approach as opposed to printing only with silicone rubber. Thus, it has been demonstrated that this printing method enables new customization opportunities in the field of anatomic models.

Keywords:

anatomic model; additive manufacturing; liver; silicone; 3D-printing

4.1 Introduction

Anatomic models have subtle but important roles in medical technology and healthcare. In medical education, they facilitate lecturing and hands-on training in a risk-free way [31, 33]. In medical device development, they accelerate progress and decrease costs by enabling repeatable testing and reducing animal or cadaver use [1]. In complex surgical cases, they aid preoperative planning and intraoperative orientation, which reduce operation time and the likelihood of errors, improving overall patient safety [4, 43]. Furthermore, anatomic models can facilitate progress in other fields such as vehicle safety [88] or forensic medicine [89]. Thus, the overall improvement of anatomic models bears a considerable social impact.

Traditionally, anatomic models are mass-produced, commercial products where hard tissue models are made of hard plastics via injection molding, while soft tissue models use rubbers via casting [90—92]. Such models are widely used in medical education and device development due to their low price and availability, even though they come with three distinct limitations. The first one is that these mass-produced models do not match the anatomy of any specific patient, rendering them impractical for preoperative planning. This problem is eased by various 3D-printing technologies that became mainstream over the past decade [9]. They enable the reproduction of patient anatomy, based on 3D-geometry data segmented from medical images [93, 94].

The second limitation is the representation of soft tissue mechanical properties, which affects all domains of anatomic model use cases. Neither mass-produced nor 3D-printed anatomic models capture the viscoelastic soft tissue behavior which determines the forces arising from tool-tissue interaction or manual tissue handling during surgery [15]. Even though certain commercial technologies can print with various rubbers [23, 24, 45, 57, 58], their soft tissue model use cases are targeted at simply providing patient-specific geometries with an elastic material [5]. To ease the approximation of soft tissues using rubbers, Estermann *et al*. (2020) [95] compared various cast and 3D-printed rubber materials with fresh porcine and bovine liver tissues, pointing out that none of the discussed rubbers mimic the liver tissues from both an elastic and a viscous standpoint simultaneously. Meanwhile, according to a review by Witowski *et al*. (2017) [96] most reported 3D-printed liver models only target geometric accuracy and use hard materials. Ratinam *et al*. (2019) [27] reviewed various 3D-printed tissue mimicking options and suggested that soft tissues could be represented better if viscous liquids were included in 3D-printed structures. Further research efforts have visited this problem of soft tissue representation in anatomic models, by either using commercial printers in innovative ways [10, 11, 97, 98], or experimenting with self-built prototype printers [19, 25, 26, 59, 99]. However, none of these have experimented with combining different 3D-printing technologies to improve soft tissue anatomic model realism.

Finally, the third limitation is a lack of anatomic models that mimic tissues in their appearance under various medical imaging modalities, while also retaining realistic mechanical properties [100]. Taking advantage of 3D-printing to create image-based (thus potentially patient-specific) geometries, with materials and structures that mimic tissues from both a radiological and mechanical standpoint, is therefore a potential – albeit complex – way to improve anatomic model realism. Moreover, ample available data and the challenging mechanical properties of liver tissue [95, 101, 102] make it an ideal target for such investigations and test prints.

In recent publications, a custom-built prototype printer [28] was described, that combines fused filament fabrication (FFF) and direct ink writing (DIW) technologies. The capabilities of this system in terms of printable geometries [29] have also been explored.

4.1.1 Objectives

In this case study, the complete design and manufacturing process of a mechanically and radiologically tuned liver model is presented. The goal of the study was twofold. The first goal was to develop a liver model that mimics real liver tissue concerning the initial elastic modulus and dissipated energy ratio of the multi-material structure, while also considering printing limitations. The second goal was to compare the printed liver model in terms of mechanical and radiological properties with actual liver tissue as reported in literature. Finally, a reflection is provided on the potential uses, limitations, and development opportunities of the used printing technology in the domain of anatomic models.

4.2 Materials and methods

To achieve the goals of this study stated above, a liver model and a set of tensile testing specimens have been designed and manufactured. The tensile testing specimens were necessary since the organic shape of the liver model is problematic in case of tensile testing. The liver model then underwent CT-scanning to reveal its radiological properties, while the tensile testing specimens were cyclically tested to evaluate the mechanical properties. Figure 4.1 provides an overview of what has been done in this study.

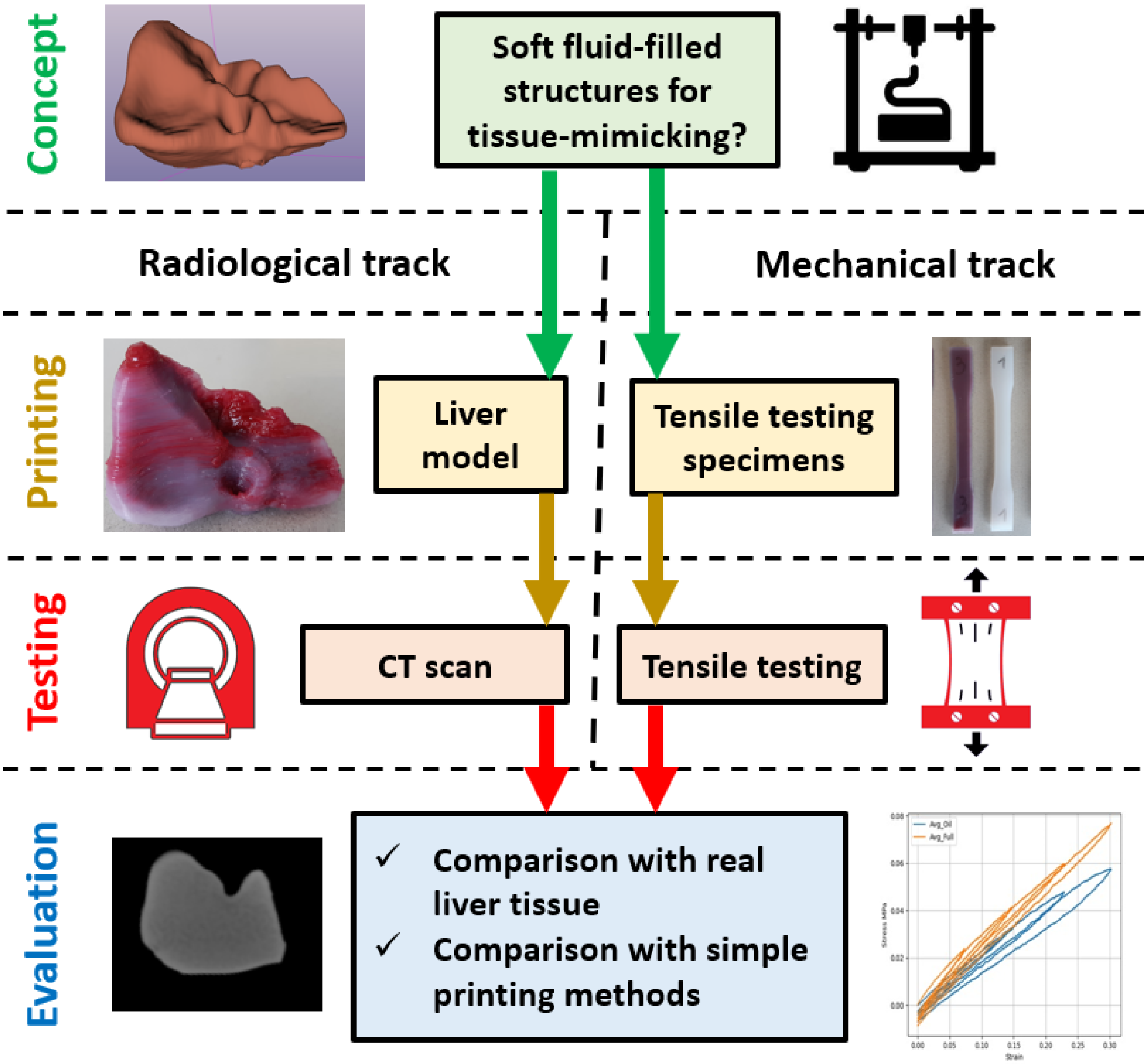

Figure 4.1: A summary of design, manufacturing and evaluation steps performed in present study

4.2.1 Segmentation and post-processing

To obtain the geometry of a human liver, its shape was segmented from an anonymous torso Computed Tomography (CT) scan, using the region growing segmentation tool of the open-source 3D-Slicer v5.0.3 software [103]. After exporting from 3D-Slicer in STL format, the 3D data was post-processed in Autodesk Meshmixer v3.5 [104]. The main goal of the post-processing was to smoothen the effects of the rather coarse CT-scan resolution, and to repair any mesh errors stemming from exporting.

4.2.2 Design and materials

The primary objective in selecting materials and material structure for the liver model was achieving a degree of macroscopic mechanical realism. Realizing an anatomically correct internal organ structure was not in the scope of this study. In previous studies [101, 102], fresh human, porcine and bovine liver tissue samples were found to exhibit strain-stiffening and viscoelastic tensile behavior. These studies suggest that for a liver-mimicking anatomic model, a material structure with an initial elastic modulus of approx. 100 kPa should be used, after which some degree of strain-stiffening and viscoelastic behavior should be exhibited.

This is challenging, as all the previously tested single-component printing silicones are an order of magnitude stiffer according to their technical datasheets [29]. However, prior printing experience with the system [28, 29] suggests that lower infill structures can make printed objects macroscopically softer than the bulk printing material, but printing infill structures below 40% silicone volume fraction is often unreliable in terms of printing success. Furthermore, preliminary experience of printing a viscous fluid into an infill structure has shown to increase viscous macroscopic mechanical behavior upon deformation.

Considering these limitations, a 40% gyroid infill volume fraction was chosen for the liver model, which would be filled with a viscous but inert filler fluid. This material structure is not expected to perfectly mimic the mechanical properties of human liver due to technological limitations, but to offer a more realistic – albeit still printable – alternative to printing or casting solely out of silicone rubber, while getting as close to the target elastic modulus (100 kPa) as possible with the printer and the known single-component printing materials.

The material chosen to print the shell and infill structure of the liver model was the softest available single component liquid silicone rubber already tested with the system [29], namely the Elkem AMSil 20101 (Elkem Silicones SAS, Lyon, France) [82]. This material starts curing upon contact with air, with skin formation within 10 minutes and full crosslinking within 24 hours after deposition at room temperature.

The rest of the internal space was filled up with a red-colored poly-dimethyl-siloxane (PDMS) oil with 100 Pas dynamic viscosity (Optimal Products GmbH, Bad Oeynhausen, Germany) [105]. This was chosen as the highest viscosity fluid available at the supplier that could still be filled into a cartridge to feed the printhead. Preliminary experience also shows that the presence of PDMS oil does not inhibit the crosslinking of the chosen silicone, as long as they are not mixed together. Dark red color was chosen to improve visual appearance and was achieved by mixing 1 w/w% of Silc Pig "Blood" paint (Smooth-On Inc., Macungie, PE) [106] into the PDMS oil. It was assumed that this coloring additive does not have a significant effect on the overall mechanical behavior of the PDMS oil.

It was also expected that the liver geometry will require some degree of hard overhang support during printing. A common poly-lactic-acid (PLA) filament was selected (Material4Print GmbH & co. KG, Löhne, Germany) for printing the required support structure. The properties of all used materials are summarized in Table 4.1.

Table 4.1: Properties of the materials used to print the liver model

Material Property	**Silicone rubber (Structure)**	**PDMS Oil (Filler Fluid)**	**PLA (Support)**
Color	translucent	red	black
Density (g/cm³)	1.01	1.00	1.24
Viscosity (Pas)	410	100	n/a
Shore Hardness	A 18	n/a	approx. D 70
Tensile Strength (MPa)	1.10	n/a	60
Elongation at break (%)	400	n/a	160
Printing temperature (°C)	room temp.	room temp.	200
Shear thinning / shape holding	yes	no	n/a
Pot life	approx. 10 min.	inf.	n/a
Cure time	approx. 24 h	n/a	n/a

4.2.3 Print settings and slicing

The print setup, slicing and G-code generation was conducted in the open-source Prusa Slicer v2.4.2 [107] software (Figure 4.2). The liver model size was linearly downscaled to 33% in all three directions, so that printing the whole object would be possible with a single 55 ml cartridge of each material and within a working day. This downscaled STL file represented the outer shape of the liver model.

Due to the organic and often overhanging shape, a relatively thick contour was desired to ensure sufficient sealing against filler fluid leakages, requiring an approx. 2 mm thick solid shell around the infill structure. To achieve this, the downscaled STL of the outer shape was further offset by 2 mm inwards in Meshmixer to represent the shape of the inner structure of the liver model (Figure 4.2 A), occupied by both the infill structure and the filler fluid.

To enable filling the infill structure with a fluid, the infill structure was generated and sliced first, then the resulting G-code pathways were exported as an OBJ file from Prusa Slicer (Figure 4.2 B). This gyroid geometry was then smoothened in Meshmixer (Figure 4.2 C), saved as a standalone STL file and re-imported into Prusa Slicer (Figure 4.2 D). Finally, this gyroid infill geometry was overlaid with the original outer shape as a multi-part (and multi-material) object, allowing the assignment of the silicone rubber nozzle to the outer shell and the gyroid pattern, and the PDMS oil nozzle to the cavities within the gyroid infill (Figure 4.2 E). Support structures were generated under the overhanging features of the liver model, and the FFF-nozzle (loaded with PLA filament) was assigned to all support structures (Figure 4.2 E).

Since the liver model´s organic shape is incompatible with standard tensile testing protocols, the ASTM D638-14 Type I [108] tensile testing specimen geometry was printed three times with 7 mm thickness, approx. 1 mm solid shell (Table 4.2) and the same internal structuring as in the liver model to enable tensile testing and reveal how the liver model would behave if it could be tested. Additionally, three more tensile testing specimens were printed with 100% rectilinear infill out of silicone, to enable a comparison between the chosen fluid-filled gyroid structuring and the raw silicone material (Figure 4.3). The liver-matching tensile testing specimens were given a shell thickness of only 1 mm (as opposed to 2 mm in case of the liver model) to improve the quality and relevance of the tensile testing results. Preliminary experience shows that choosing a thinner shell may cause leakages of the filler fluid, while choosing a thicker shell would severely influence tensile testing results. Finally, a printing speed of 20 mm/s was selected for all seven print runs. A summary of the most important print settings is provided in Table 4.2.

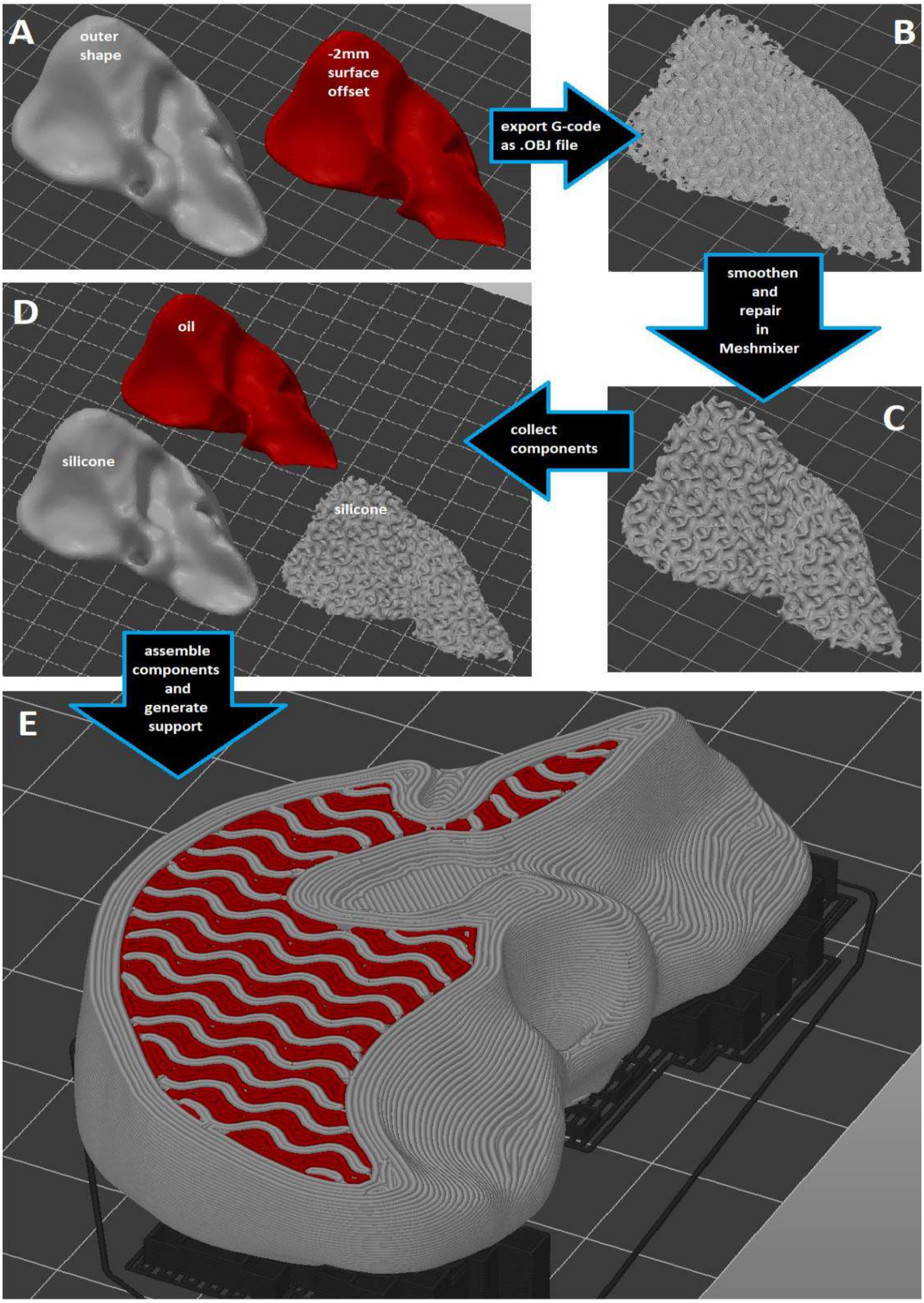

Figure 4.2: The workflow of generating the material structure in Prusa Slicer, involving (A) offsetting the outer shape, (B) slicing into the desired infill structure and exporting G-code pathways as an .OBJ file, (C) repairing and smoothening in Meshmixer, (D) re-importing all necessary components in Prusa Slicer, (E) assembling the liver model and generating support

Table 4.2: Key print settings of the liver model and tensile testing specimens

Setting	Value	Unit
Extrusion width	0.5	mm
Layer thickness	0.3	mm
Infill volume fraction (liver model and equivalent tensile specimens)	40	%
Infill volume fraction (full-silicone tensile specimens)	100	%
Infill type (liver model and equivalent tensile specimens)	gyroid	
Infill type (full-silicone tensile specimens)	rectilinear	
Contour (liver model)	4	lines
Contour (all tensile testing specimens)	2	lines
Solid top and bottom (liver model)	6	layers
Solid top and bottom (all tensile testing specimens)	3	layers
Print speed	20	mm/s
Travel speed	50	mm/s
Travel and tool change Z-lift	1	mm
Acceleration	500	mm/s²

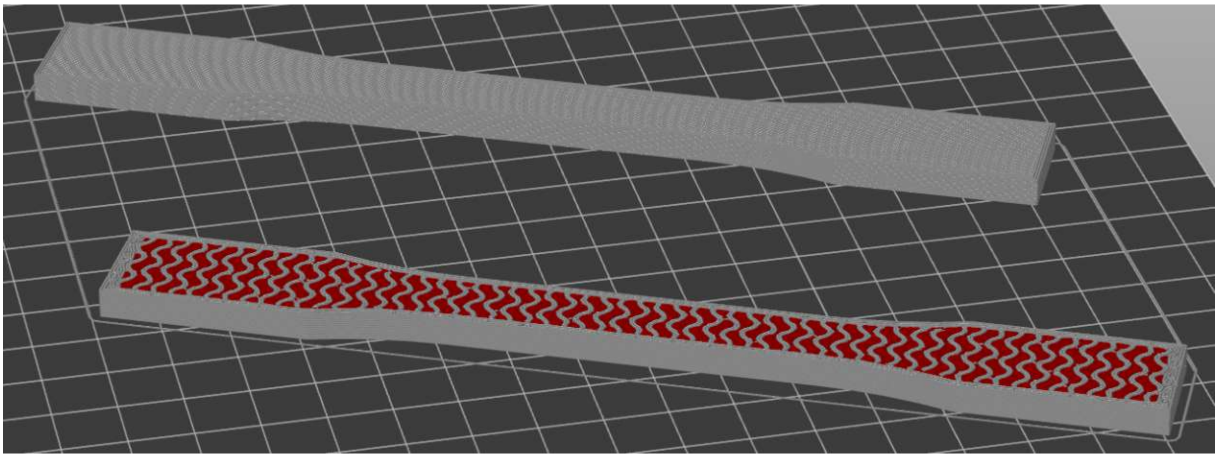

Figure 4.3: Tensile testing specimens after slicing in Prusa Slicer, with a liver-matching specimen (bottom) and a full-silicone benchmark specimen (top) displayed with the top layers hidden, to compare the inside of the specimens

4.2.4 Printer calibration and printing

The printer used in this study is an open-source FFF machine that was modified to accommodate a dual fluid extruder while retaining its original FFF printhead. It is described in more technical detail in [28] and [29]. The two halves of the fluid extruder are operable independently. One was filled with the liquid silicone rubber, the other with the red-colored high-viscosity PDMS oil, both fed from air-pressurized 55 cm³ cartridges at 6 bars. The PLA filament was loaded into the original FFF printhead of the printer. All three extruders used nozzles with 0.4 mm inner diameter. This resulted in an approx. 0.5 mm extrusion width for each nozzle, while the layer thickness was 0.3 mm in general. Both fluid extruder halves were calibrated to their respective material along the calibration process described in [28] to ensure accurate dosing. After extruder calibration, the liver model (Figure 4.4 A), three tensile testing specimens matching the liver model´s internal structure (Figure 4.4 B) and three silicone-only benchmark specimens were printed. All printing was done in ambient conditions, at room temperature. The objects were left to crosslink for approx. 48 hours on room temperature after printing. After removal from the building platform – and removal of PLA support structures in case of the liver model – the objects were weighed on a KERN EMB 200-3 laboratory scale (Kern&Sohn GmbH, Balingen, Germany) to ensure that none of them has a relative weight error larger than ±5%.

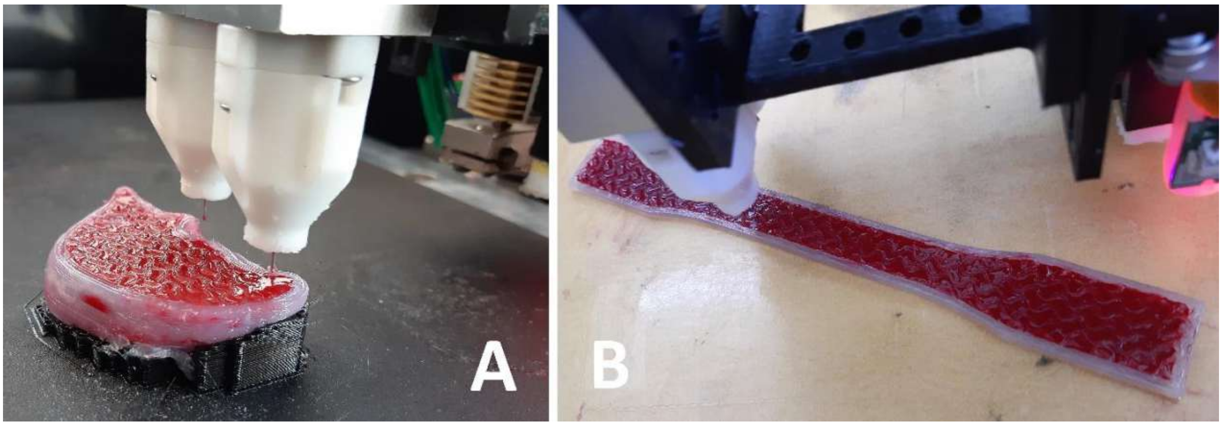

Figure 4.4: (A) printing the liver model; (B) printing a tensile testing specimen

4.2.5 Mechanical testing

The tensile testing specimens underwent a cyclical quasi-static uniaxial tensile testing protocol. The test setup involved a ZwickRoell Z030 tensile testing machine (Zwick Roell GmbH, Ulm, Germany) operating at 10 Hz sampling frequency and a Sony α-6400 high-resolution camera (Sony, Tokyo, Japan) at 1 Hz frame frequency (Figure 4.5 A). White dot markers were placed onto the specimens for deformation tracking (Figure 4.5 B) as also described in [109] and [110]. Effective gauge length (defined by the dot markers) was approx. 72 mm for all specimens.

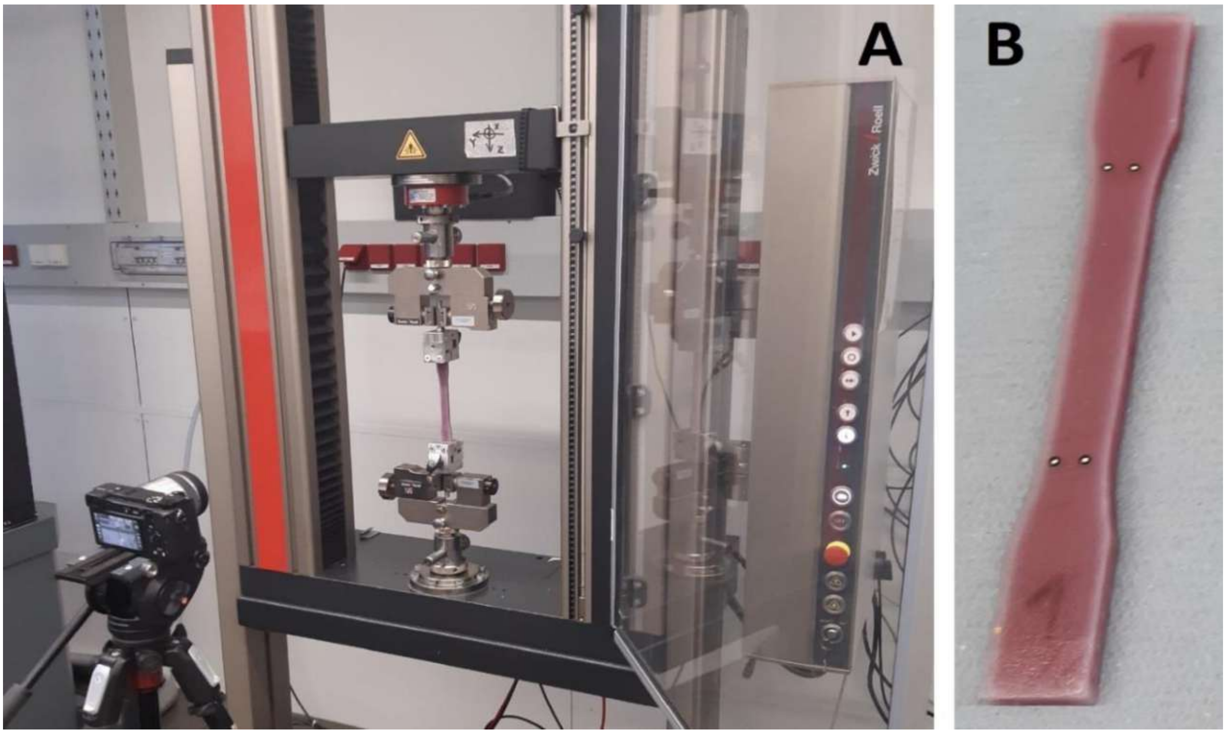

Figure 4.5: (A) the tensile testing setup; (B) the marker placement on a tensile testing specimen

The test protocol started with a preload of 5 mm, and involved four consecutive loading cycles, with 7.5%, 15%, 22.5%, and 30% target strains respectively, providing information not only about stiffness, but also about viscous behavior. All cycles were performed at 0.1 mm/s displacement rate. Deformation values were obtained via digital image correlation (DIC) as explained in further detail in [109]. During DIC, the marker positions are tracked and the relative displacement between them is calculated. Afterwards, the engineering strain (ε) is computed according to Equation (4.1):

$$\varepsilon = \frac{L - \mathrm{L}_0}{\mathrm{A}_0} \tag{4.1}$$

where L_0 is the initial distance between markers (at preload only) and L is the actual distance between markers at a given sampling moment based on DIC results, while A_0 is the initial cross-sectional area, measured with a caliper before testing.

Meanwhile, the uniaxial linear engineering stress (σ) is calculated as in Equation (4.2):

$$\sigma = \frac{f}{\mathrm{A}_0} \tag{4.2}$$

where f is the measured axial force and A_0 is the initial cross-sectional area.

The ratio of dissipated energy over a loading-unloading cycle was taken a measure of the overall viscous behavior of the multi-material structure. The total energy of a loading cycle is the area under the stress-strain curve of the loading half-cycle, while the dissipated energy of a loading cycle is the area within the hysteresis loop formed by the stress-strain curves of loading and unloading half-cycles [111]. The dimensionless ratio of the dissipated energy to the total energy is referred to as the dissipated energy ratio. Besides plotting the stress-strain curves of all four loading-unloading cycles and the initial and final elastic moduli on the last loading cycle the dissipated energy ratios for the 2nd, 3rd and 4th cycles were also calculated. In this regard, the 1st loading cycle was ignored due to distortions coming from the preload.

4.2.6 Imaging

Since the lack of respective data on fluid-filled structures and the chosen design logic of the liver model did not allow for deliberate tuning for radiological properties, achieving a degree of imaging realism was only an optional but nevertheless preferred outcome. Therefore, the liver model underwent computed tomography (CT) scanning (SOMATOM Definition AS, Siemens Healthineers, Erlangen Germany) with a modified clinical CT protocol to evaluate the radiodensity properties. The CT scan settings are listed in Table 4.3.

Table 4.3: Key CT settings used on the liver model

Setting	Value	Unit
Tube voltage	120	kVp
Tube current time product (with tube current modulation)	80	mAs
Slice thickness	0.60	mm
Pixel size	0.29	mm
Pitch	0.55	-

The table height was set to 120.5 mm and no surrounding material was used. For all sample scans a smooth J30s reconstruction kernel was applied. Analyze 12.0 toolkit (AnalyzeDirect, Over-land Park, United States) was used to estimate the average Hounsfield Unit (HU) values of the liver model. Various line profiles were manually selected inside the internal structure of liver model, and the overall HU was estimated by calculating the average and the standard deviation over all points along the selected line profiles. The same method was used on the solid silicone shell of the liver model, for comparison with the internal structure.

4.3 Results

The liver model and the tensile testing specimens were printed successfully (Figure 4.6), and all seven objects were found acceptable upon weighing. The liver model, the three matching tensile testing specimens, and the three full-silicone benchmark tensile testing specimens took approx. 10, 4 and 3 hours of printing time apiece, respectively.

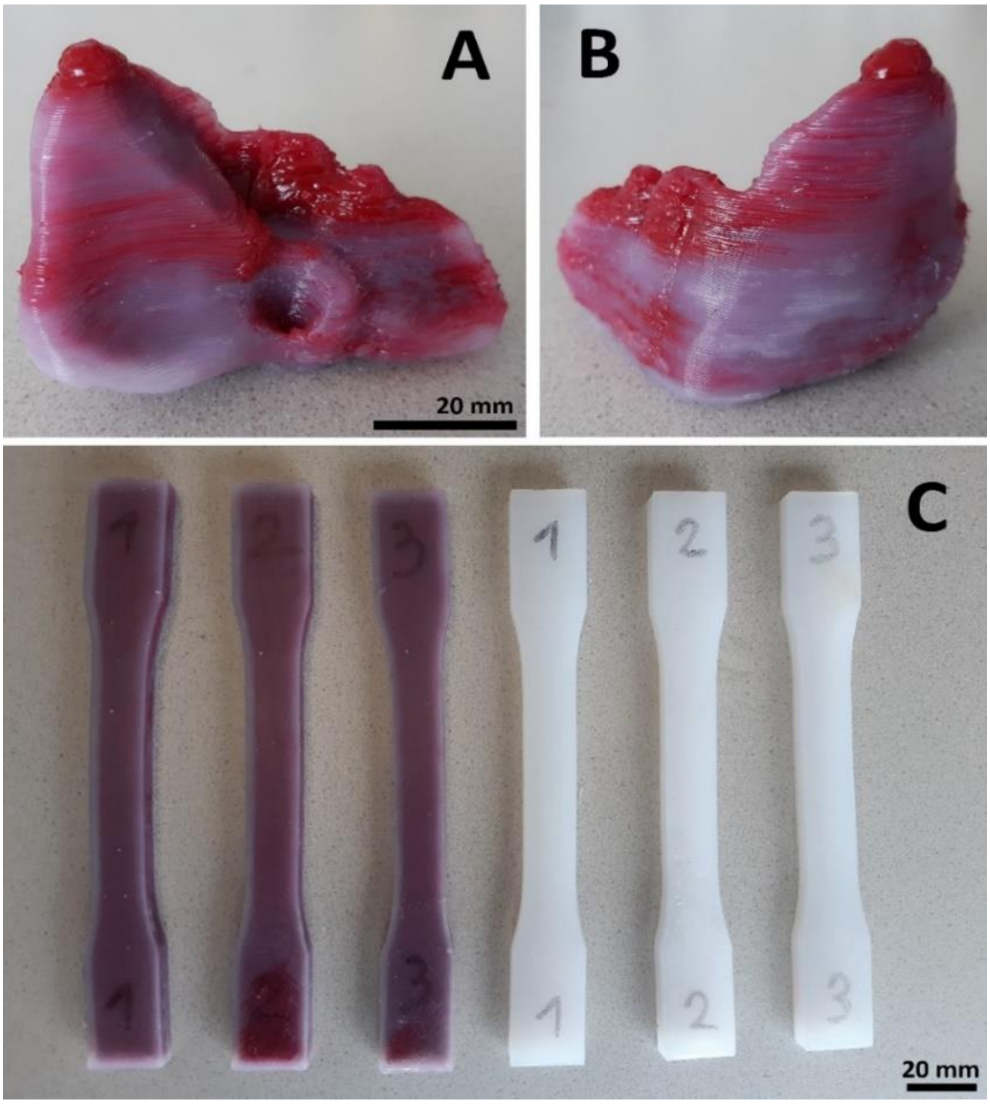

Figure 4.6: (A and B) the liver model after crosslinking and support removal; (C) the tensile testing specimens after crosslinking

The tensile testing results showed a more elastic and more viscous behavior in case of the fluid-filled tensile testing specimens compared to the full-silicone benchmark specimens (Figure 4.7 A-C). In the last loading cycle, the average initial elastic moduli (calculated between 0% and 3% strain) of the fluid-filled structure and the full silicone were 0.26 MPa and 0.37 MPa respectively, while the final moduli (calculated between 22% and 27% strain) were 0.19 MPa and 0.25 MPa respectively (Figure 4.7 D). The average dissipated energy ratios were higher and increasing across loading cycles in case of the fluid-filled structure, while lower and decreasing across loading cycles in case of full silicone. The first loading cycle was ignored in this regard due to the preload.

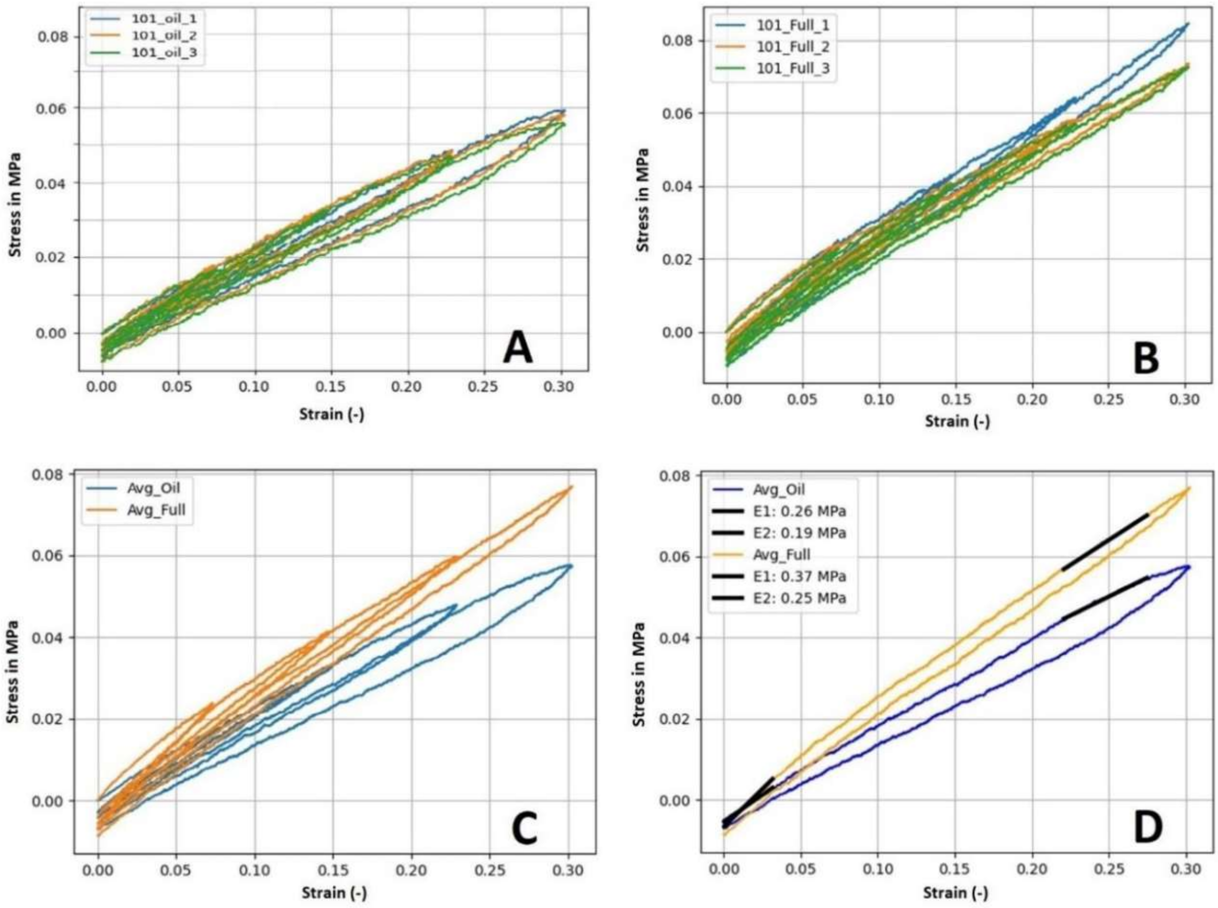

Figure 4.7: (A) tensile behavior of the individual fluid-filled specimens over all four loading cycles; (B) tensile behavior of the individual full silicone specimens; (C) average tensile behavior of the fluid-filled tensile testing specimens compared to the full silicone ones; (D) comparison in average behavior over the last loading cycle only, also comparing the initial (E1 between 0% and 3% strain) and final (E2 between 22% and 27% strain) tensile moduli

Finally, the CT scan showed an average HU density and standard deviation of 225 ± 30 HU for the internal structure of the liver model, excluding its solid shell (Figure 4.8). Meanwhile, the pixels of the solid shell showed a HU of 340 ± 50, suggesting that the liver model became more realistic due to the internal structuring compared to the bulk silicone (Table 4.4). A summary of the elastic moduli, dissipated energy ratios and HUs is given in Table 4.4, along with liver tissue values for comparison.

Table 4.4: Average elastic moduli, dissipated energy ratios and Hounsfield Units

	Liver model and fluid-filled specimens (n = 1 + 3)	**Full silicone specimens** (n = 3)	**Liver tissue** based on [101, 102, 112, 113]
Initial elastic modulus (kPa) (E1 on Figure 4.7 D, at 0-3% strain)	260	370	approx. 100 (target in this study)
Final elastic modulus (kPa) (E2 on Figure 4.7 D, at 22-27% strain)	190	250	n/a
Dissipated energy ratio (-) of 1st loading cycle (0-7.5% strain)	n/a	n/a	approx. 0.6 ± 0.1
Dissipated energy ratio (-) of 2nd loading cycle (0-15% strain)	0.140	0.118	
Dissipated energy ratio (-) of 3rd loading cycle (0-22.5% strain)	0.167	0.093	
Dissipated energy ratio (-) of 4th loading cycle (0-30% strain)	0.183	0.081	
HU of fluid-filled internal structure of liver model	225 ± 30	n/a	approx. 70 ± 30
HU of bulk outer shell of liver model	340 ± 50	n/a	

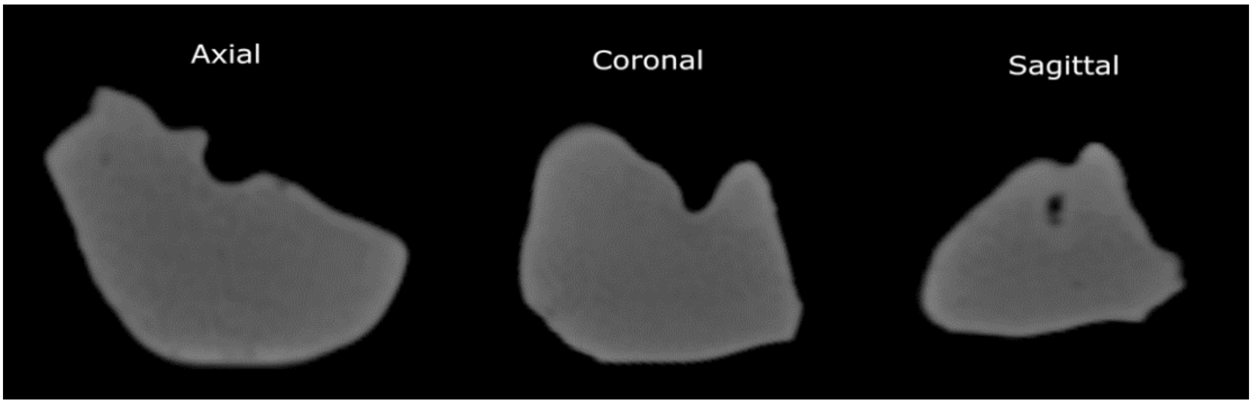

Figure 4.8: The appearance of the liver model in the CT scan in all three planes, with each view sectioned approx. at the middle of the respective envelope dimension of the model

4.4 Discussion

In this study, a liver model was designed based on a CT-image regarding its shape and available literature regarding its desired mechanical properties, while accounting for technological limitations. The infill pattern generation workflow relies on open-source software, which may be useful for other researchers for filling infill structures with fluids. A previously published and tested open-source printer [28, 29] was used to manufacture the liver model and a set of tensile testing specimens out of silicone rubber and PDMS oil, using PLA as support. The printed liver model underwent CT scanning, and it was found that its internal structuring has brought it closer to actual liver tissue HUs compared to the bulk silicone material. Meanwhile the tensile testing results show that the used internal structure has also brought the liver model closer to real liver tissue from a mechanical standpoint compared to bulk silicone, decreasing elastic moduli and increasing dissipated energy ratios.

4.4.1 Printing performance

Despite the extensive use of PLA support structures, the liver model presented a relatively straightforward print run. The visible color inhomogeneities (Figure 4.6 A, B) were likely caused by unwanted droplets of the filler fluid falling onto the object from the inactive nozzle. This could be avoided with either longer pullback settings upon tool switching, or by upgrading the printer with a tool-changing or lifting mechanism for inactive extruders as in [23] and [58].

Theoretically, the liver model could also be printed without downscaling to 33% in each direction, but a full-scale model would consume large amounts of material, and require frequent cartridge changes, and either a printing time over a week, or a much coarser printing resolution with larger nozzle. In such a case, some anatomical features – like larger and medium-sized vessels – could also be represented inside the internal structure of the liver model, but at a cost of potentially compromising freedom in mechanical and radiological property tuning.

Moreover, in case of larger prints with soft materials, the deformation of the printed object under its own weight would likely require some degree of compensation, and such a feature is not yet available in current 3D-printing software. Alternatively, printing could happen in a support bath with the same density as the printing materials, which would prevent a large soft object from such deformations. However, this would also prevent the use of any closed internal cavities or filler fluids. In general, solving such practical limitations of the printer were not in the scope of this study, since the demonstration of material property tuning was possible, nevertheless.

4.4.2 Mechanical behavior

In case of the fluid-filled structure, the lower elastic moduli (compared to full silicone) are likely caused by having less silicone in the internal structure (Figure 4.8), while the increase in dissipated energy ratios (Table 4.4) can be associated with the viscous filler fluid circulating within the silicone gyroid structure upon deformation.

As stated in Section 4.2.2 and Table 4.4, the desired initial elastic modulus was 100 kPa, after which some degree of strain-stiffening and overall viscoelastic behavior was desired. As expected with the knowledge of printing limitations, the fluid-filled tensile testing specimens (and thus the liver model) provided a mechanical behavior that is closer to real liver tissue than the behavior of the full silicone benchmark specimens, in terms of both elasticity and viscosity, although not matching it perfectly with an initial elastic modulus of 260 kPa instead of 100 kPa, and dissipated energy ratios in the range of 0.14 – 0.19 instead of approx. 0.5 – 0.7 (Table 4.4). The elastic modulus could have been even lower with a softer material or if the specimens were printable with no solid outer shell. Unfortunately, the latter is not possible by principle, as the fluid would leak from the specimens upon deformation if there was no shell.

Also, the typical strain-stiffening behavior characteristic to liver tissue [101] was not reflected in the results in this study. This is not surprising, since most biological tissues feature a fibrous hierarchic structure, which stiffens when strained. Such fibers were not present in the current internal structuring strategy, suggesting further potential topics for future trials. In general, conducting future trials with multiple levels of design parameters and various materials – as in

[114] or [115] – may reveal further material combinations that are especially useful in tissue mimicking.

Comparison of the present liver model with others in literature is difficult, as most clinical studies involving printed liver models do not report the exact material properties of the printing materials according to systematic reviews on the topic by Witowski *et al*. (2017) and Qiu *et al*. (2018) [5, 96]. However, most reported liver models rely on FFF or Stereolithography technologies with hard materials and focus on geometry only. The ones that use droplet jetting (PolyJet) also focus on geometry and use transparent but relatively hard materials (Vero) instead of softer ones (TangoPlus), which could theoretically enable some degree of mechanical tissue mimicking [5].

4.4.3 Radiological behavior

The comparability between the obtained CT scan of the liver model and scans of real human liver tissue in literature is somewhat limited due to numerous differences in CT systems, energy settings, surrounding materials, orientation, and post-processing methods. However, such a comparison of HUs may help evaluate the results at least from a qualitative standpoint, nevertheless.

The HU values of the human liver are approx. 70 ± 30 HU [112, 113] within a typical general CT value range of approx. -1000 (air) to +1000 (cortical bone) HU. Meanwhile, an average 225 ± 30 HU was observed in the internal structure of the liver model. Printing the model out of pure silicone rubber would have yielded a higher, 340 ± 50 average HU for the inside of the model as well, not only for the outer shell. Moreover, it is known from prior experiments [116] that a gyroid infill structure of 40% with single-component silicones (without filler fluid) yields approx. –500 HU.

Therefore, the chosen fluid-filled internal structuring has made the model more realistic from a radiological standpoint compared to both the bulk silicone material and the same infill structure without fluid filling. Furthermore, the radiological appearance of such fluid-filled internal structures may be further altered by using various filler fluid mixtures to reach a wider range of HUs [100], considering a potential future direction of research.

4.5 Conclusion

In this study, a custom-built multi-material 3D-printer was used to print a downscaled liver model out of silicone rubber and PDMS oil, using PLA for support structures. The chosen fluid-filled internal structure has brought the model closer to actual liver tissue from both a mechanical and a radiological standpoint at the same time compared to both bulk silicone and matching but fluid-free infill structuring. These results prove that extrusion-based multi-material fluid printing represents a versatile platform for tissue approximation in terms of both mechanical and radiological properties in functional anatomic models. Meanwhile, hardware, software and material constraints that limited tissue mimicking accuracy in the case of the present liver model have been identified, and respective upgrades or improvements were proposed. Once such improvements are made, the present printing and material structuring method could significantly contribute to the current state of the art in realistic anatomic models, offering an extrusion-based alternative to droplet jetting and an open-source alternative to commercial systems at the same time.

5 Conclusion and Outlook

After the introduction and goal statements in Chapter 1, the consecutive Chapters 2–4 contained the original contributions that were published in peer-reviewed journals, forming the core content of this dissertation. The initial research objectives were establishing a multi-material 3D-printer with the potential to print tissue-mimicking material structures, evaluating the limits of this printer, and finally printing an actual anatomic model with tissue-mimicking features. These were all accomplished along Chapters 2–4, offering new opportunities for customization and increased realism in medical education, device development and preoperative planning. This final chapter provides a big-picture reflection on the key learnings from this research and related future possibilities.

5.1 Key takeaways

1. A 3D-printer was built, that combines FFF and DIW techniques to print anatomic models. This combination enables the use of various printing materials in liquid and filament form, which is useful for creating anatomic models with tissue-mimicking material structures. The combination of FFF and DIW techniques in 3D-printing could have significant implications for the creation of anatomic models with tissue-mimicking material structures, which could be useful in medical education, surgical planning, and simulation of medical procedures, especially if a larger range of materials is tested.

2. This printer can deposit soft and hard materials to represent soft tissue and bone in one print. This is due to the adhesion between single-component silicone rubber and thermoplastic materials to create multi-material objects with both soft and hard parts. This printing modality is ideal for creating anatomic models involving both soft and hard tissues, and the FFF printhead may be used to print hard support under soft silicone structures irrespective of adhesion. Moreover, the established printer is capable of printing thin-walled structures, large internal cavities, and fine infill structures out of silicone rubber.

3. In terms of geometric limitations, printing with highly viscous silicones was somewhat more limited but overall similar to FFF printing with PLA. The observations concerning the effect of viscosity and unstable geometric features may also serve as a guide in fluid printing. Furthermore, a printhead calibration method was proposed for accurate material dosing, which is crucial for evaluating printing limitations, and tested geometric printing limitations with three silicone rubber materials. This calibration method could be useful in improving the accuracy and reliability of similar 3D printers more generally.

4. Counter-intuitively, higher silicone viscosity correlated with larger dimensional errors and higher failure rates. The observation that a higher dynamic viscosity does not necessarily lead to more stable printing, suggests that there is a higher limit to viscosity, above which the drawbacks – higher losses in extruder feeding and printing, more difficult cartridge filling, etc. – outweigh the printability benefits, and may even lead to inferior printing results.

5. Encapsulation of viscous filler fluid inside a soft infill structure was used to mimic liver tissue. This happened in a proof-of-concept printing case of a CT image-based human liver mode, with a multi-material structure consisting of silicone rubber gyroid pattern with PDMS oil as a filler fluid. This structure achieved closer mechanical behavior to real liver tissue than printing the whole object out of silicone rubber would have, in terms of elasticity and dissipated energy ratio. The development workflow of such fluid-filled multi-material structures – including the generation of the "negative gyroid" to define filler fluid printing trajectories – could prove helpful in further research that relies on open-source software.

6. The liver model became more realistic in radiological appearance as well, besides mechanical properties. The multi-material structure of the liver model got closer to real human liver tissue in terms of Hounsfield Units under CT, proving that the printer can create tissue-mimicking material structures in the realm of radiological properties too. In case of overlaps between the optimal – or acceptable – multi-material structures for mechanical and radiological realism, multi-purpose models may also become feasible for certain tissues.

5.2 Future possibilities

1. The used methods are transferable to other organs or anatomic structures. The same design method that was explained in Chapter 4 is easily transferable to other soft organ models, while the last printing case of Chapter 2 is a good example of anatomic models involving both bones and soft tissues.

2. Upon sufficient material availability and some hardware modifications, the printed models may be scaled to normal size and printed with larger nozzles.

3. Models involving muscle, tendons and ligaments could include fibers. This could be realized by using one printhead to print the shape, and another to deposit fibers into the object, potentially creating anisotropic, composite-like behavior. Additionally, soft organ models could be printed in such a manner that the infill structure is chosen to match a desired radiological appearance. This may either mean an "empty" infill structure, or a fluid-filled one where the fluid choice is another degree of freedom available for property tuning.

4. Introducing color mixing is also an option. With certain modifications to the printheads, objects may be printed with paint mixed into the silicone rubber right before deposition, yielding either gradient or sharp changes in color, significantly improving visual appearance.

5. Lastly, all the printing strategies explained throughout this dissertation would largely benefit from gantry systems and appropriate software that enable non-planar slicing and printing of the objects, providing additional degrees of freedom – both in the literal and the abstract sense – to make anatomic models even more realistic.

Such improvements remain to be seen and were out of the scope of this dissertation, but they could serve as inspiring starting ideas for the future continuation of this research.

List of Figures and Image Credits

List of Tables

Table and description **Page**

List of References

[1] K. Wang, C. C. Ho, C. Zhang, B. Wang: A Review on the 3D Printing of Functional Structures for Medical Phantoms and Regenerated Tissue and Organ Applications, *Engineering*, 3(5):653–662, 2017, DOI: 10.1016/J.ENG.2017.05.013

[2] A. Pietrabissa, S. Marconi, E. Negrello, V. Mauri, A. Peri, E. M. Marone, F. Auricchio: An overview on 3D printing for abdominal surgery, *Surgical Endoscopy*, 34:1-13, 2019, DOI: 10.1007/s00464-019-07155-5

[3] F. Rengier, A. Mehndiratta, H. Tengg-Kobligk, C. M. Zechmann, R. Unterhinninghofen, H. U. Kauczor, F. L. Giesel: 3D printing based on imaging data: review of medical applications, *International Journal of Computer Assisted Radiology and Surgery*, 5:335–341, 2010, DOI: 10.1007/s11548-010-0476-x

[4] P. Tack, J. Victor, P. Gemmel, L. Annemans: 3D-printing techniques in a medical setting: a systematic literature review, *Biomedical Engineering Online*, 15:115, 2016, DOI: 10.1186/s12938-016-0236-4

[5] K. Qiu, G. Haghiashtiani M. C. McAlpine: 3D Printed Organ Models for Surgical Applications, *Annual Review of Analytical Chemistry*, 11(1):287-306, 2018, DOI: 10.1146/annurev-anchem-061417-125935

[6] A. R. Studart: Additive manufacturing of biologically-inspired materials, *Chemical Society Reviews*, 45(2):359–376, 2016, DOI: 10.1039/C5CS00836K

[7] W. Oropallo, L. A. Piegl: "Ten challenges in 3d printing" *Engineering with Computers*, 32:135–148, 2016, DOI: 10.1007/s00366-015-0407-0

[8] C. L. Ventola: Medical Applications for 3D Printing: Current and Projected Uses, *Pharmacy and Therapeutics*, 39(10):704–711, 2014, PMCID: PMC4189697

[9] T. D. Ngo, A. Kashani, G. Imbalzano, K. T. Q. Nguyen, D. Hui: Additive manufacturing (3D printing): A review of materials, methods, applications and challenges, *Composites Part B*, 143:172-196, 2018, DOI: 10.1016/j.compositesb.2018.02.012

[10] R. L. Truby, J. A. Lewis: Printing soft matter in three dimensions, *Nature*, 540:371–378, 2016, DOI: 10.1038/nature21003

[11] C. N. Ionita, M. Mokin, N. Varble, D. R. Bednarek, J. Xiang, K. V. Snyder, A. H. Siddiqui, E. I. Levy, H. Meng, S. Rudin: Challenges and limitations of patient-specific vascular phantom fabrication using 3D Polyjet printing, *Proceedings - SPIE - The International Society for Optical Engineering*, 2014, DOI: 10.1117/12.2042266

[12] M. Reiter, Z. Major: A combined experimental and simulation approach for modelling the mechanical behaviour of heterogeneous materials using rapid prototyped microcells, *Virtual and Physical Prototyping*, 6(2):111–120, 2011, DOI: 10.1080/17452759.2011.586949

[13] K. Wang, Y. Zhao, Y. H. Chang, Z. Qian, C. Zhang, B. Wang, M. A. Vannan, M. J. Wang: Controlling the mechanical behavior of dual-material 3D printed meta-materials for patient-specific tissue-mimicking phantoms, *Materials & Design*, 90:704-712, 2016, DOI: 10.1016/j.matdes.2015.11.022

[14] J. Hiller, H. Lipson: Tunable digital material properties for 3D voxel printers, *Rapid Prototyping Journal*, 16 (4):241–247, 2010, DOI: 10.1108/13552541011049252

[15] K. Wang, C. Wu, Z. Qian, C. Zhang, B. Wang, M. Vannan: Dual-material 3D printed metamaterials with tunable mechanical properties for patient-specific tissue-mimicking phantoms, *Additive Manufacturing*, 12(A):31-37, 2016, DOI: 10.1016/j.addma.2016.06.006

[16] D. Godec, K. Krizetic, A. Pilipovic, Influence of Infill Pattern on 3D-Printed Parts Compression Strength, *Technical Journal*, 16(3):315-319, 2022, DOI: 10.31803/tg-20220413112955

[17] Da Vinci Color Printer: www.xyzprinting.com/en/product/da-vinci-color (Accessed 14.03.2023)

[18] Diamond FFF Hotend: www.reprap.org/wiki/Diamond_Hotend (Accessed 14 03 2023)

[19] M. A. Skylar-Scott, J. Mueller, C. W. Visser, J. A. Lewis: Voxelated soft material via multimaterial multinozzle 3D printing, *Nature*, 575:330–334, 2019, DOI: 10.1038/s41586-019-1736-8

[20] Fripp Design Ltd.: www.picsima.com (Accessed 14.03.2023)

[21] InnovatiQ GmbH: www.innovatiq.com (Accessed 14 03 2023)

[22] Wacker Chemie AG: www.wacker.com/cms/en-us/products/brands/aceo/aceo.html (Accessed 14.03.2023)

[23] Deltatower GmbH: www.deltatower.ch/en/home-2 (Accessed 14.03.2023)

[24] Spectroplast AG: www.spectroplast.com (Accessed 14.03.2023)

[25] J. O. Hardin, T. J. Ober, A. D. Valentine, J. A. Lewis: Microfluidic Printheads for Multimaterial 3D Printing of Viscoelastic Inks, *Advanced Materials*, 27(21):3279-3284, 2015, DOI: 10.1002/adma.201500222

[26] W. Liu, Y. S. Zhang, M. A. Heinrich, F. DeFerrari, H. L. Jang, S. M. Bakht, M. M. Alvarez, J. Yang, Y. C. Li, G. T. de Santiago, A. K. Miri, K. Zhu, P. Khoshakhlagh, G. Prakash, H. Cheng, X. Guan: Rapid Continuous Multimaterial Extrusion Bioprinting, *Advanced Materials*, 29(3):1604630, 2016, DOI: 10.1002/adma.201604630

[27] R. Ratinam, M. Quayle, J. Crock, M. Lazarus, Q. Fogg, P. McMenamin: Challenges in creating dissectible anatomical 3D prints for surgical teaching, *Journal of Anatomy*, 234(4):419–437, 2019, DOI: 10.1111/joa.12934

[28] L. Jaksa, D. Pahr, G. Kronreif, A. Lorenz: Development of a Multi-Material 3D Printer for Functional Anatomic Models, *International Journal of Bioprinting*, 7(4):420, 2021, DOI: 10.18063/ijb.v7i4.420

[29] L. Jaksa, D. Pahr, G. Kronreif, A. Lorenz: Calibration Dependencies and Accuracy Assessment of a Silicone Rubber 3D Printer, *Inventions*, 7(2):35, 2022, DOI: 10.3390/inventions7020035

[30] L. Jaksa, O. J. Aryeetey, S. Hatamikia, K. Nägl, M. Buschmann, D. H. Pahr, G. Kronreif, A. Lorenz: 3D-printed multi-material liver model with simultaneous mechanical and radiological tissue-mimicking features for improved realism, *International Journal of Bioprinting*, 9(3):721, 2023, DOI: 10.18063/ijb.721

[31] Z. Khot, K. Quinlan, G. R. Norman, B. Wainmane: The relative effectiveness of computer-based and traditional resources for education in anatomy, *Anatomical Sciences Education*, 6(4):211–215, 2013, DOI: 10.1002/ase.1355

[32] A. Sulaiman, L. Boussel, F. Taconnet, J. M. Serfaty, H. Alsaid, C. Attia, L. Huet, P. Douek: In vitro non-rigid life-size model of aortic arch aneurysm for endovascular prosthesis assessment, *European Journal of Cardio-Thoracic Surgery*, 33(1):53–57, 2008, DOI: 10.1016/j.ejcts.2007.10.016

[33] D. Preece, S. B. Williams, R. Lam, R. Weller: Let's get physical: advantages of a physical model over 3D computer models and textbooks in learning imaging anatomy, *Anatomical Sciences Education*, 6(4):216–224, 2013, DOI: 10.1002/ase.1345

[34] F. L. Giesel, A. R. Hart, H. K. Hahn, E. Wignall, F. Rengier, R. Talanow, I. D. Wilkinson, C. M. Zechmann, M. A. Weber, H. U. Kauczor, M. Essig, P. D. Griffiths: 3D reconstructions of the cerebral ventricles and volume quantification in children with brain malformations, *Academic Radiology*, 16(5):610-617, 2009, DOI: 10.1016/j.acra.2008.11.010

[35] A. Golab, T. Smektala, K. Kaczmarek, R. Stamirowski, M. Hrab, M. Slojewski: Laparoscopic Partial Nephrectomy Supported by Training Involving Personalized Silicone Replica Poured in Three-Dimensional Printed Casting Mold, *Journal of Laparoendoscopic and Advanced Surgical Techniques*, 27(4):420–422, 2017, DOI: 10.1089/lap.2016.0596

[36] M. E. Mavili, H. I. Canter, B. Saglam-Aydinatay, S. Kamaci and I. Kocadereli: Use of Three-Dimensional Medical Modeling Methods for Precise Planning of Orthognathic Surgery, *Journal of Craniofacial Surgery*, 18(4):740-747, 2007, DOI: 10.1097/scs.0b013e318069014f

[37] J. Poukens, J. Haex, D. Riediger: The use of rapid prototyping in the preoperative planning of distraction osteogenesis of the cranio-maxillofacial skeleton, *Computer Aided Surgery*, 8(3):146-154, 2003, DOI: 10.3109/10929080309146049

[38] Q. Yan, H. Dong, J. Su, J. Han, B. Song, Q. Wei, Y. Shi: A Review of 3D Printing Technology for Medical Applications, *Engineering*, 4(5):729–742, 2018, DOI: 10.1016/j.eng.2018.07.021

[39] Z. Qian, K. Wang, S. Liu, X. Zhou, V. Rajagopal, C. Meduri, J. R. Kauten, Y. H. Chang, C. Wu, C. Zhang, B. Wang, M. A. Vannan: Quantitative Prediction of Paravalvular Leak in Transcatheter Aortic Valve Replacement Based on Tissue-Mimicking 3D Printing, *Journals of the American College of Cardiology: Cardiovascular Imaging*, 10(7):719–731, 2017, DOI: 10.1016/j.jcmg.2017.04.005

[40] G. L. Goh, H. Zhang, T. H. Chong, W. Y. Yeong: 3D Printing of Multilayered and Multimaterial Electronics: A Review, *Advanced Electronic Materials*, 7(10):2100445, 2021, DOI: 10.1002/aelm.202100445

[41] Y. L. Yap, S. L. Sing, W. Y. Yeong: A review of 3D printing processes and materials for soft robotics, *Rapid Prototyping Journal*, 26(8):1345-1361, 2020, DOI: 10.1108/RPJ-11-2019-0302

[42] B. Dorweiler, P. E. Baque, R. Chaban, A. Ghazy, O. Salem: Quality Control in 3D Printing: Accuracy Analysis of 3D-Printed Models of Patient-Specific Anatomy, *Materials*, 14(4):1021, 2021, DOI: 10.3390/ma14041021

[43] L. Pugliese, S. Marconi, E. Negrello, V. Mauri, A. Peri, V. Gallo, F. Auricchio, A. Pietrabissa: The clinical use of 3D printing in surgery, *Updates in Surgery*, 70:381–388, 2018, DOI: 10.1007/s13304-018-0586-5

[44] M. J. Mirzaali, A. H. d. l. Nava, D. Gunashekar, M. Nouri-Goushkia, R. P. E. Veegera, Q. Grossman, L. Angeloni, M. K. Ghatkesar, L. E. Fratila-Apachitei, D. Ruffoni, E. L. Doubrovski, A. A. Zadpoor: Mechanics of bioinspired functionally graded soft-hard composites made by multi-material 3D printing, *Composite Structures*, 237:111867, 2020, DOI: 10.1016/j.compstruct.2020.111867

[45] Stratasys Ltd.: www.stratasys.com/medical/advanced-medical-models (Accessed 14.03.2023)

[46] US2019224914A1: Additive Manufacturing of rubber-like materials (Patent, 2019)

[47] V. Y. Slesarenko: Towards mechanical characterization of soft digital materials for multimaterial 3D-printing, *International Journal of Engineering Science*, 123:62-72, 2017, DOI: 10.1016/j.ijengsci.2017.11.011

[48] G. L. Goh, S. Agarwala, W. I. Yong: 3D printing of microfludic sensor for soft robots: a preliminary study in design and fabrication, *Proceedings of the 2nd International Conference on Progress in Additive Manufacturing*, 2016

[49] J. Yeo, J. Koh, F. Wang, Z. Li, C. He: 3D Printing Silicone Materials and Devices, *Silicon Containing Hybrid Copolymers,* Chapter 9: 239-263, Wiley-VCH Verlag GmbH & Co. KGaA, 2020, DOI: 10.1002/9783527823499.ch9

[50] Y. Zhao, R. Yao, L. Ouyang, H. Ding, T. Zhang, K. Zhang, S. Cheng, W. Sun: Three-dimensional printing of Hela cells for cervical tumor model in vitro, *Biofabrication*, 6:035001, 2014, DOI: 10.1088/1758-5082/6/3/035001

[51] J. M. Lee, S. L. Sing, W. Y. Yeong: Bioprinting of Multimaterials with Computer-aided Design/Computer -aided Manufacturing, *International Journal of Bioprinting*, 6(1):245, 2020, DOI: 10.18063/ijb.v6i1.245

[52] F. Coulter: www.fergalcoulter.eu (Accessed 14.03.2023)

[53] F. Coulter, M. Schaffner, J. Faber, A. Rafsanjani, R. Smith, H. Appa, P. Zilla, D. Bezuidenhout, A. Studart: Bioinspired Heart Valve Prosthesis Made by Silicone Additive Manufacturing, *Matter*, 1(1):266-279, 2019, DOI: 10.1016/j.matt.2019.05.013

[54] E. Luis, H. M. Pan, S. L. Sing, A. K. Bastola, G. L. Goh, H. K. J. Tan, R. Bajpai, J. Song, W. Y. Yeong: Silicone 3D Printing: Process Optimization, Product Biocompatibility, and Reliability of Silicone Meniscus Implants, *3D Printing and Additive Manufacturing*, 6(6):319-332, 2019, DOI: 10.1089/3dp.2018.0226

[55] E. Luis, H. M. Pan, S. L. Sing, R. Bajpai: 3D Direct Printing of Silicone Meniscus Implant Using a Novel Heat-Cured Extrusion-Based Printer, *Polymers*, 12(5):1031, 2020, DOI: 10.3390/polym12051031

[56] WO2017108208A1: 3D-printing device and process for producing an object with use of a 3D-printing device (Patent, 2017)

[57] Lynxter SAS: www.lynxter.fr/en/product/3d-printing-silicone-toolhead-liq21 (Accessed 14.03.2023)

[58] CR-3D: www.cr3d.de/3d-drucker/liquid-serie (Accessed 14.03.2023)

[59] S. E. Bakarich, R. Gorkin, M. Panhuis, G. M. Spinks: Three-Dimensional Printing Fiber Reinforced Hydrogel Composites, *American Chemical Society: Applied Materials and Interfaces*, 6(18):15998–16006, 2014, DOI: 10.1021/am503878d

[60] Viscotec GmbH: www.viscotec.de/produkte/3d-druckkoepfe (Accessed 14.03.2023)

[61] Railcore Labs: www.railcore.org (Accessed 14.03.2023)

[62] Duet 3D Printer Electronics: www.duet3d.com/DuetWifi (Accessed 14.03.2023)

[63] F. Melchels, J. Feijen, D. Grijpma: A review on stereolithography and its applications in biomedical engineering, *Biomaterials*, 31(24):6121–6130, 2010, DOI: 10.1016/j.biomaterials.2010.04.050

[64] A. Harynska, I. Carayona, P. Kosmela, K. Szeliski, M. Lapinski, M. Pokrywczynska, J. Kucinska-Lipka, H. Janik: A comprehensive evaluation of flexible FDM/FFF 3D printing filament as a potential material in medical application, *European Polymer Journal*, 138:109958, 2020, DOI: 10.1016/j.eurpolymj.2020.109958

[65] E. Edelmers, D. Kazoka and M. Pilmane: Creation of Anatomically Correct and Optimized for 3D Printing Human Bone Models, *Applied System Innovation*, 4(3):67, 2021, DOI: 10.3390/asi4030067

[66] A. Kantaros, D. Piromalis: Fabricating Lattice Structures via 3D Printing: The Case of Porous Bio-Engineered Scaffolds, *Applied Mechanics*, 2(2):289–302, 2021, DOI: 10.3390/applmech2020018

[67] K. S. Soni, M. Taufik: Design and assembly of fused filament fabrication (FFF) 3D printers, *Materials Today: Proceedings*, 46(11):5233–5241, 2021, DOI: 10.1016/j.matpr.2020.08.627

[68] S. Walker, U. Daalkhaijav, D. Thrush, C. Branyan, O. Yirmibesoglu, G. Olson, Y. Menguc: Zero-Support 3D Printing of Thermoset Silicone Via Simultaneous Control of Both Reaction Kinetics and Transient Rheology, *3D Printing and Additive Manufacturing*, 6(3):139–147, 2019, DOI: 10.1089/3dp.2018.0117

[69] M. Fernandez-Vicente, M. Canyada, A. Conejero: Identifying limitations for design for manufacturing with desktop FFF 3D printers, *International Journal of Rapid Manufacturing*, 5(1):116-128, 2015, DOI: 10.1504/IJRAPIDM.2015.073551

[70] J. Jiang, J. Stringer, X. Xu, R. Zhong: Investigation of printable threshold overhang angle in extrusion-based additive manufacturing for reducing support waste, *International Journal of Computer Integrated Manufacturing*, 31(10):961-969, 2018, DOI: 10.1080/0951192X.2018.1466398

[71] J. Jiang, G. Hu, X. Li, X. Xu, P. Zheng, J. Stringer: Analysis and prediction of printable bridge length in fused deposition modelling based on backpropagation neural network, *Virtual and Physical Prototyping*, 14(3):253-266, 2019, DOI: 10.1080/17452759.2019.1576010

[72] J. Jiang, X. Xu, J. Stringer: Optimization of process planning for reducing material waste in extrusion based additive manufacturing, *Robotics and Computer Integrated Manufacturing*, 59:317-325, 2019, DOI: 10.1016/j.rcim.2019.05.007

[73] L. Rebaioli, I. Fassi: A review on benchmark artifacts for evaluating the geometrical performance of additive manufacturing processes, *International Journal of Advanced Manufacturing Technologies*, 93:2571–2598, 2017, DOI: 10.1007/s00170-017-0570-0

[74] ISO/ASTM 52910:2018 Additive manufacturing - Design - Requirements, guidelines and recommendations

[75] ISO 17296-3:2014 Additive manufacturing - General principles - Part 3: Main characteristics and corresponding test methods

[76] ISO/ASTM 52902:2019 Additive manufacturing - Test artifacts - Geometric capability assessment of additive manufacturing systems

[77] A. K. Sood, R. Ohdar, S. Mahapatra: Parametric appraisal of mechanical property of fused deposition modelling processed parts, *Materials & Design*, 31(1):287–295, 2010, DOI: 10.1016/j.matdes.2009.06.016

[78] A. Kantaros, D. Piromalis: Employing a Low-Cost Desktop 3D Printer: Challenges, and How to Overcome Them by Tuning Key Process Parameters, *International Journal of Mechanics and Applications*, 10(1):11-19, 2021, DOI: 10.5923/j.mechanics.20211001.02

[79] A. Kantaros, D. Karalekas: FBG Based in Situ Characterization of Residual Strains in FDM Process, *Residual Stress, Thermo-mechanics & Infrared Imaging, Hybrid Techniques and Inverse Problems*, 2013

[80] Bondtech AB: www.bondtech.se/product/bmg-extruder (Accessed 14.03.2023)

[81] E3D-Online: www.e3d-online.com/products/v6-all-metal-hotend (Accessed 14.03.2023)

[82] Elkem AMSil Silicones: www.elkem.com/silicones/brands/amsil (Accessed 14.03.2023)

[83] Duet 3D Documentation: www.duet3d.dozuki.com/Wiki/M592 (Accessed 14.03.2023)

[84] Full Control G-Code: www.fullcontrolgcode.com (Accessed 14.03.2023)

[85] G. Percoco, L. Arleo, G. Stano, F. Bottiglione: Analytical model to predict the extrusion force as a function of the layer height, in extrusion based 3D printing, *Additive Manufacturing*, 38:101791, 2021, DOI: 10.1016/j.addma.2020.101791

[86] S. Singh, G. Singh, C. Prakash, S. Ramakrishna: Current status and future directions of fused filament fabrication, *Journal of Manufacturing Processes*, 55:288-306, 2020, DOI: 10.1016/j.jmapro.2020.04.049

[87] J. Stieghorst, T. Doll: Rheological behavior of PDMS silicone rubber for 3D printing of medical implants, *Additive Manufacturing*, 24:217-223, 2018, DOI: 10.1016/j.addma.2018.10.004

[88] P. Mohan, D. Marzougui, C.-D. Kan: Development and Validation of Hybrid III Crash Test Dummy, *Society of Automotive Engineers: Technical Paper*, 2009, DOI: 10.4271/2009-01-0473

[89] C. Humphrey, J. Kumaratilake: Ballistics and anatomical modelling – A review, *Legal Medicine*, 23:21-29, 2016, DOI: 10.1016/j.legalmed.2016.09.002

[90] K. Trehan, C. D. Kemp, S. C. Yang: Simulation in cardiothoracic surgical training: Where do we stand?, *Journal of Thoracic and Cardiovascular Surgery*, 147(1):18-24, 2014, DOI: 10.1016/j.jtcvs.2013.09.007

[91] E. Kurt, S. E. Yurdakul, A. Atac: An Overview Of The Technologies Used For Anatomy Education In Terms Of Medical History, *Procedia - Social and Behavioral Sciences*, 103:109-115, 2013, DOI: 10.1016/j.sbspro.2013.10.314

[92] J. B. Cooper, V. R. Taqueti: A brief history of the development of mannequin simulators for clinical education and training, *Quality & Safety*, 84(997):563–570, 2004, DOI: 10.1136/qshc.2004.009886

[93] D. I. Nikitichev, P. Patel, J. Avery, L. J. Robertson, T. M. Bucking, K. Y. Aristovich, E. Maneas, A. E. Desjardins, T. Vercauteren: Patient-Specific 3D Printed Models for Education, Research and Surgical Simulation, *3D Printing*, Chapter 6, IntechOpen Publishing Ltd., 2018, DOI: 10.5772/intechopen.79667

[94] V. Waran, V. Narayanan, R. Karuppiah, D. Pancharatnam, H. Chandran, R. Raman, Z. A. A. Rahman, S. L. F. Owen, T. Z. Aziz: Injecting realism in surgical training-initial simulation experience with custom 3D models, *Journal of Surgical Education*, 71(2):193-197, 2014, DOI: 10.1016/j.jsurg.2013.08.010

[95] S. J. Estermann, D. H. Pahr, A. Reisinger: Quantifying tactile properties of liver tissue, silicone elastomers, and a 3D printed, *Journal of the Mechanical Behavior of Biomedical Materials*, 104:103630, 2020, DOI: 10.1016/j.jmbbm.2020.103630

[96] J. S. Witowski, J. Coles-Black, T. Z. Zuzak, M. Pedziwiatr, J. Chuen, P. Major, A. Budzynski: 3D Printing in Liver Surgery: A Systematic Review, *Telemedicine and e-Health*, 23(12): 943-947, 2017, DOI: 10.1089/tmj.2017.0049

[97] M. M. Maddox, A. Feibus, J. Liu, J. Wang, R. Thomas, J. L. Silberstein: 3D-printed soft-tissue physical models of renal malignancies for individualized surgical simulation: a feasibility study, *Journal of Robotic Surgery*, 12:27–33, 2018, DOI: 10.1007/s11701-017-0680-6.

[98] M. Saari, B. Xia, P. S. Krueger, A. L. Cohen, E. Richer: Additive manufacturing of soft and composite parts from thermoplastic elastomers, *International Solid Freeform Fabrication Symposium*, 2015

[99] J. W. Jung, J. S. Lee, D. W. Cho: Computer-aided multiple-head 3D printing system for printing of heterogeneous organ/tissue constructs, *Scientific Reports*, 6:21685, 2016, DOI: 10.1038/srep21685

[100] L. Talalwa, G. Natour, A. Bauer, A. Drzezga, S. Beer: Radiological characteristics of a new experimental rubber elastomeric polymer used in three-dimensional printing with different infill densities and patterns, *Journal of Physics Communications*, 4:125006, 2020, DOI: 10.1088/2399-6528/abd1c3

[101] S. J. Estermann, S. Förster-Streffleur, L. Hirtler, J. Streicher, D. H. Pahr, A. Reisinger: Comparison of Thiel preserved, fresh human, and animal liver tissue, *Annals of Anatomy*, 236:151717, 2021, DOI: 10.1016/j.aanat.2021.151717

[102] S. J. Estermann, D. H. Pahr, A. Reisinger: Hyperelastic and viscoelastic characterization of hepatic tissue under uniaxial tension in time and frequency domain, *Journal of the Mechanical Behavior of Biomedical Materials*, 112:104038, 2020, DOI: 10.1016/j.jmbbm.2020.104038

[103] 3D-Slicer: www.slicer.org (Accessed 14.03.2023)

[104] Autodesk Meshmixer: www.meshmixer.com (Accessed 14.03.2023)

[105] Optimal Products GmbH: www.optimal-products.de/silikonoele (Accessed 14.03.2023)

[106] Smooth-On Silc Pig Paints: www.smooth-on.com/products/silc-pig (Accessed 14.03.2023)

[107] Prusa Research a.s.: www.prusa3d.com/page/prusaslicer_424 (Accessed 14.03.2023)

[108] ASTM D638-14: Standard Test Method for Tensile Properties of Plastics

[109] O. J. Aryeetey, M. Frank, A. Lorenz, S. J. Estermann, A. Reisinger and D. H. Pahr: A parameter reduced adaptive quasi-linear viscoelastic model for soft biological tissue in uniaxial tension, *Journal of the Mechanical Behavior of Biomedical Materials*, 126:104999, 2021, DOI: 10.1016/j.jmbbm.2021.104999

[110] M. Frank, D. Marx, V. Nedelkovski, J.-T. Fischer, D. Pahr and P. Thurner: Dehydration of individual bovine trabeculae causes transition from ductile to quasi brittle failure mode, *Journal of the Mechanical Behavior of Biomedical Materials*, 87:296–305, 2018, DOI: 10.1016/j.jmbbm.2018.07.039

[111] O. J. Aryeetey, M. Frank, A. Lorenz and D. H. Pahr: Fracture toughness determination of porcine muscle tissue based on AQLV model derived viscous dissipated energy, *Journal of the Mechanical Behavior of Biomedical Materials*, 153:105429, 2022, DOI: 10.1016/j.jmbbm.2022.105429

[112] E. Rietzel, D. Schardt, T. Haberer: Range accuracy in carbon ion treatment planning based on CT-calibration with real tissue samples, *Radiation Oncology*, 2:14, 2007, DOI: 10.1186/1748-717X-2-14

[113] J. M. Toledo, T. P. C. Ribeiro: Radiological evaluation of a liver simulator in comparison to a human real liver, *Proceedings of the International Nuclear Atlantic Conference*, 2009

[114] G. D. Goh, S. L. Sing, J. L. J. Thong, Z. K. Peh, S. R. Mogali, W. Y. Yeong: Machine learning for 3D printed multi-material tissue-mimicking anatomical models, *Materials & Design*, 211:110125, 2021, DOI: 10.1016/j.matdes.2021.110125

[115] J. Kwon, J. Ock, N. Kim: Mimicking the mechanical properties of aortic tissue with pattern-embedded 3D printing for a realistic phantom, *Materials*, 13(21):5042, 2020, DOI: 10.3390/ma13215042

[116] L. Jaksa, S. Hatamikia, D. Pahr, G. Kronreif, A. Lorenz: 3D-Printer Enabling Customized Anatomic Models, *Poster, 27th Congress of the European Society of Biomechanics*, 2022, DOI: 10.13140/RG.2.2.28812.39049